

ABSTRACT

Title of Dissertation: ENERGETICS OF DRUG INTERACTIONS

Niya Ancheva Todorova, Doctor of
Philosophy, 2008

Directed By: Professor Frederick P. Schwarz
Center for Advanced Research in Biotechnology,
University of Maryland Biotechnology Institute
Professor Zvi Kelman
Molecular and Cell Biology

The goal of our research is to determine in terms of thermodynamic change of state functions the effects of experimental factors, such as water, mutagenesis, or the presence of a second substrate on the energetics of drug-inhibitor binding interactions. The binding of non-steroidal anti-inflammatory drugs within the rigid cavities of cyclodextrins was investigated by titration calorimetry and spectrofluorimetry. Loss of bulk water structure upon drug binding in the smaller hydrophobic β -cyclodextrin cavity results in an increase in the binding entropy, while restriction of the configurations of the drug in the cavity decreases the binding entropy. This restriction in the hydrophobic β -cyclodextrin cavity enhances the binding enthalpies so that the β -cyclodextrin binding reactions are enthalpy-driven. In the larger γ -cyclodextrin cavity, water is retained so that, not only are the interactions between the drug and the cavity reduced, there is an increase in the drug configurations resulting in increases in the binding entropies and the binding reactions

become entropically-driven. These binding reactions also manifest enthalpy-entropy compensation where changes in the binding enthalpies are compensated by changes in the binding entropies. In drug binding to the more flexible p38 α MAP kinase mutants, a single-point C \rightarrow S mutation distal from the binding site, changes the interaction between the N- and C-terminal structural domains of the kinase as evident in differential scanning calorimetry. Calorimetric results show that drug-inhibitor binding affinities to kinase increase with size of the drugs since the binding reactions are all enthalpically-driven. Drug-inhibitors binding to trimeric human purine nucleoside phosphorylase were investigated by calorimetry in the presence of its second substrate, inorganic phosphate (Pi). Increasing concentrations of Pi modulates the driving-nature of the binding reaction, so that the acyclovir binding almost exclusively to the purine substrate binding site becomes more entropically-driven, while the binding reactions of ganciclovir and 9-benzylguanine interacting also with the adjacent Pi substrate site become more enthalpically-driven. A novel calorimetric enzyme activity assay at the low dissociation concentrations of the phosphorylase show an increase in the enzyme activity at low Pi concentrations, but also a decrease in the 9-benzylguanine binding affinity since this drug also interacts with an adjacent subunit.

ENERGETICS OF DRUG INTERACTIONS

By

Niya Ancheva Todorova

Dissertation submitted to the Faculty of the Graduate School of the
University of Maryland, College Park, in partial fulfillment
of the requirements for the degree of
Doctor of Philosophy
2008

Advisory Committee:
Professor Zvi Kelman, Chair
Professor Frederick P. Schwarz, Co-chair
Professor Jeffery T. Davis
Professor Richard C. Stewart
Professor Sergei Sukharev
Professor Steve Mount

© Copyright by
Niya Ancheva Todorova
2008

Preface

Declaration of author's intent to use own published text.

1) The main text, figures and figure legends for:

Chapter 3: The role of water in the thermodynamics of drug binding to cyclodextrin

Chapter 4: Effect of the distal C162S mutation on the energetics of drug binding to p38 α MAP kinase

Chapter 5: Effect of the phosphate substrate on drug-inhibitor binding to human purine nucleoside phosphorylase

were used, and only modified for readability/formatting within the context of this dissertation. Full citations are given below.

Todorova, N.A. and F.P. Schwarz, *The role of water in the thermodynamics of drug binding to cyclodextrin*. J Chem Thermodynamics, 2007. **39**: p. 1038-48.

Todorova, N.A., V. Doseeva, J. Ramprakash, and F.P. Schwarz, *Effect of the distal C162S mutation on the energetics of drug binding to p38 α MAP kinase*. Arch Biochem Biophys, 2008. **469**(2): p. 232-42.

Todorova, N.A. and F.P. Schwarz, *Effect of the phosphate substrate on drug-inhibitor binding to human purine nucleoside phosphorylase*. Arch Biochem Biophys, in press.

Dedication

With love to my family and my husband Harshaka

Acknowledgements

I would like to express my gratitude to my research advisor Fred Schwarz for his guidance and valuable advice during my graduate work in CARB for the past three years. His enormous experience as a PI, his down-to-earth, focused thinking, and his intelligent advice made the publication of my graduate research work possible. I view this as a great success since I did not have the opportunity to be in a research environment as an undergraduate student and entered graduate school with limited experience in the laboratory.

I would like to thank sincerely all the members of the third floor of CARB 1B, former and present for the valuable discussions and their advice not only professional but also personal. The weekly meetings on the floor gave me an excellent opportunity to practice my communication skills in my area of research as well as learn more about the interesting work done around me and enrich my knowledge in the broad field of science.

I would like to mention here the name of a fellow graduate student, Nozomi, and thank her for her friendship and needed conversations. She also is in the process of writing her dissertation and I would like to take the time here to wish her all the best in her future endeavors.

I would like to thank all the members of my advisory committee for their advice and guidance throughout my graduate work. I would like to extend my special thanks to my co-advisor Zvi Kelman for his help with the molecular biology techniques and his advice throughout my graduate work.

I would like to thank with all my heart my parents without whose support on the first place I would not be in the United States pursuing my education. Their love, support and encouragement throughout my years in the United States helped me reach this stage of my education, my Ph.D. defense. I would also like to mention here my brother who is pursuing his education in Germany and wish him all the best in all his future endeavors.

Last but not least, I would like to thank my husband Harshaka for his support, understanding and patience that helped me accomplish many goals as a graduate student as well as deal with the many challenges on the way. I would like to extend my special thanks to my brother-in-law Rajeev who helped me to improve the quality for several figures in my dissertation.

Table of Contents

Preface.....	ii
Dedication.....	iii
Acknowledgements.....	iv
Table of Contents.....	vi
List of Tables.....	viii
List of Figures.....	x
List of Abbreviations.....	xiii
 Chapter 1: Protein-drug interactions.....	 1
1.1 Rational drug design.....	1
1.2 Energetics of drug design.....	4
1.3 Experimental drug design.....	6
1.4 Research goals of drug-protein interactions.....	9
 Chapter 2: Experimental methods.....	 11
2.1 Isothermal titration calorimetry.....	11
2.2 Displacement ITC.....	14
2.3 Enzyme kinetics by ITC.....	15
2.4 Differential scanning calorimetry.....	18
2.5 Fluorescence spectroscopy.....	24
 Chapter 3: The role of water in the thermodynamics of drug binding to cyclodextrin.....	 29
3.1 Abstract.....	29
3.2 Introduction.....	30
3.3 Materials and Methods.....	36
3.3.1 Materials.....	36
3.3.2 Determination of the drug concentration in phosphate buffer.....	37
3.3.3 Phenolphthalein assay for cyclodextrin concentration.....	37
3.3.4 Isothermal titration calorimetry measurements.....	39
3.3.5 Spectrofluorimetry measurements.....	42
3.4 Results.....	44
3.4.1 ITC measurements.....	44
3.4.2 Fluorescence measurements.....	57
3.5 Discussion.....	61
 Chapter 4: Effects of the distal C162S mutation on the energetics of drug binding to p38 α MAP kinase.....	 68
4.1 Abstract.....	68
4.2 Introduction.....	68
4.3 Materials and Methods.....	78
4.3.1 Protein cloning, expression and purification.....	78
4.3.2 Isothermal titration calorimetry.....	80

4.3.3 Displacement isothermal titration calorimetry	82
4.3.4 Differential scanning calorimetry	83
4.4 Results	85
4.5 Discussion	103
Chapter 5: Effect of the phosphate substrate on drug-inhibitor binding to human purine nucleoside phosphorylase	
5.1 Abstract	109
5.2 Introduction	110
5.3 Materials and Methods	116
5.3.1 Materials	116
5.3.2 Drug-inhibitor binding reactions by ITC	117
5.3.3 Enzyme assays by ITC	119
5.3.4 Static light scattering	121
5.3.5 Size exclusion chromatography	122
5.4 Results	123
5.5 Discussion	143
Chapter 6: Conclusions	
6.1 Binding affinities of drug-protein interactions	151
6.2 The importance of determining the driving-nature of the binding reaction	154
6.3 Heat capacity changes favoring or hindering drug-protein interactions	156
6.4 The role of water in the energetics of drug-protein interactions	157
6.5 Importance of correlating thermodynamic and structural data in characterizing drug-protein interactions	158
Appendices	
Appendix A - UV-Vis spectrophotometry	161
Appendix B - HPLC analysis of FLP, NPX, NAB, and 9-benzylguanine	163
Appendix C - Circular Dichroism measurements	165
Appendix D - Size-exclusion chromatography	169
Appendix E- Static light scattering	170
Appendix F - Derivation of equation used for analyzing fluorescence data	172
Appendix G - Determination of K_b from the shift in the transition temperature induced by binding of the drug in the folded state of the protein and temperature shift calculations from DSC experiments	173
Bibliography	175

List of Tables

Table 3-1. The extinction coefficients of FLP, NAB, and NPX determined in ethanol and in acetonitrile.....	38
Table 3-2. Comparison of ITC calibrations with the literature values.....	41
Table 3-3. Thermodynamics of drug binding to β -cyclodextrin as a function of temperature	52
Table 3-4. Thermodynamics of drug binding to γ -cyclodextrin as a function of temperature	53
Table 3-5. Thermodynamics of drug binding to β -cyclodextrin at different pHs and $T = 298.15$ K	55
Table 3-6. Thermodynamics of drug binding to β -cyclodextrin as a function of added NaCl concentration at $T = 298.15$ K.....	56
Table 3-7. Comparison of ΔG^0 values with the literature values.....	65
Table 4-1. Thermodynamics of SB 203580 and SKF 86002 binding to isoform 1 and isoform 1 C162S in 5 mM HEPES buffer at pH 7.4 ± 0.1 from ITC measurements .	90
Table 4-2. Thermodynamics of SB 203580 and SKF 86002 binding to isoform 2 and isoform 2 C162S in 5 mM HEPES buffer at pH 7.4 ± 0.1 from ITC measurements .	91
Table 4-3. Thermodynamics of p38 INH.1 binding to the isoforms in 5 mM HEPES buffer at pH 7.4 ± 0.1 from ITC displacement measurements.....	94
Table 4-4. Thermodynamic transition parameters of isoform 1 and its C162S mutant and in the presence of drug inhibitors from fits of a two-state transition model to the DSC data.....	99
Table 4-5. Thermodynamic transition parameters of isoform 2 and its C162S mutant and in the presence of drug inhibitors from fits of a two-state transition model to the DSC data	100
Table 5-1. Thermodynamics of Acyclovir Binding to hsPNP in Buffer at pH 7.4 ± 0.1 from ITC Results.....	128
Table 5-2. Thermodynamics of Ganciclovir Binding to hsPNP in Buffer at pH 7.4 ± 0.1 from ITC Results.....	129
Table 5-3. Thermodynamics of 9-Benzylguanine Binding to hsPNP in Buffer at pH 7.4 ± 0.1 from ITC	130

Table 5-4. Enzyme kinetic parameters for hsPNP determined from ITC measurements using 7-methylguanosine as a substrate and calculated specific activity values at 25°C	138
---	-----

Table 5-5. Enzyme Inhibition constants determined from enzyme kinetic measurements in 100 mM HEPES + 50 mM potassium phosphate buffer at pH =7.0 and 25°C from ITC Measurements.	142
---	-----

List of Figures

Figure 2-1. Schematic diagram of a typical ITC instrument with raw and analyzed data display.....	12
Figure 2-2. Schematic diagram of a typical DSC instrument with raw data display ...	19
Figure 2-3. Schematic diagram of a spectrofluorimeter.....	27
Figure 3-1. Chemical structures of FLP (a), NAB (b), and NPX (c).....	31
Figure 3-2. Schematic representation of β -cyclodextrin and the most stable three dimensional molecular configuration.....	32
Figure 3-3. ITC scan of FLP binding to β -cyclodextrin at $T = 298.15$ K, pH 6.1 and no added salt and fit of a 1:1 binding model to the binding isotherm data.	45
Figure 3-4. ITC scan of NAB binding to β -cyclodextrin at $T = 293.15$ K, pH 7.1 and no added salt and fit of a 1:1 binding model to the binding isotherm data.....	46
Figure 3-5. ITC scan of NPX binding to β -cyclodextrin at $T = 298.15$ K, pH 6.1 and no added salt and fit of a 1:1 binding model to the binding isotherm data.....	47
Figure 3-6. ITC scan of FLP binding to γ -cyclodextrin at $T = 298.15$ K, pH 7.1 and no added salt and fit of a 1:1 binding model to the binding isotherm data.....	48
Figure 3-7. ITC scan of NPX binding to γ -cyclodextrin at $T = 303.15$ K, pH 7.1 and no added salt and fit of a 1:1 binding model to the binding isotherm data.....	49
Figure 3-8. Plot of the fluorescence intensity as a ratio for FLP in phosphate buffer against the added β -cyclodextrin concentration at $T = 298$ K.....	58
Figure 3-9. Plot of the fluorescence intensity as a ratio for NAB in phosphate buffer against the added β -cyclodextrin concentration at $T = 298$ K.....	60
Figure 4-1. Diagram of the MAPK signaling pathway.....	70
Figure 4-2. Chemical structures of used inhibitors: (a) SKF 86002; (b) SB 203580; (c) p38 INH.1.....	73
Figure 4-3. Schematic exon alignment of splice variants of p38 α MAP kinase.....	75
Figure 4-4. Aligned X-ray crystal structures for wild type (wt) and mutant C162S p38 α MAP kinase main isoform.....	77

Figure 4-5. ITC scan of SB 203580 binding to isoform 1 at 30 °C and fit of a 1:1 binding model to the binding isotherm of this scan.....	86
Figure 4-6. ITC scan of SKF 86002 binding to isoform 1 C162S at 25 °C and fit of a 1:1 binding model to the binding isotherm of this scan.....	88
Figure 4-7. ITC scan of SB 203580 binding to isoform 1 C162S at 30 °C and fit of a 1:1 binding model to the binding isotherm of this scan.....	89
Figure 4-8. ITC scan of p38 INH.1 binding to isoform 1 C162S complexed with SKF 86002 at 25 °C and fit of a 1:1 binding model to the binding isotherm of this scan.....	93
Figure 4-9. DSC scans at 60°C hr ⁻¹ of isoform 2 (a) and of isoform 2 complexed with SB 203580 (b).....	96
Figure 4-10. DSC scans at 60°C hr ⁻¹ of isoform 2 C162S (a) and of isoform 2 C162S complexed with SB 203580 (b).....	97
Figure 4-11. Aligned X-ray crystal structures for wt and mutant p38α MAPK main isoform bound to SB 203580 and p38 INH.1, respectively.....	104
Figure 5-1. Schematic representation of the reaction catalyzed by purine nucleoside phosphorylase.....	111
Figure 5-2. Structures of the drug-inhibitors for hsPNP: a) Acyclovir; b) Ganciclovir; c) 9-benzylguanine.....	115
Figure 5-3. ITC scan of acyclovir binding to hsPNP in 5 mM phosphate buffer (pH = 7.4) at 25°C and fit of a 1:1 binding model to the binding isotherm of this scan.....	124
Figure 5-4. ITC scan of ganciclovir binding to hsPNP in 100 mM phosphate buffer at 25°C and fit of a 1:1 binding model to the binding isotherm of this scan.....	125
Figure 5-5. ITC scan of 9-benzylguanine binding to hsPNP in 100 mM [Pi] buffer at 25°C and fit of a 1:1 binding model to the binding isotherm of this scan.....	126
Figure 5-6. Drug-inhibitor thermodynamic binding quantities as a function of Pi concentration.....	133
Figure 5-7. Molar mass distribution plot of hsPNP alone and in the presence of Acyclovir.....	135
Figure 5-8. ITC enzyme kinetics scan of hsPNP with the substrate 7-methylguanosine in the presence of 50 mM potassium phosphate, at 25°C.....	137

Figure 5-9. A fit of the Michaelis-Menten model to the hsPNP enzyme reaction rate as a function of the added 7-methylguanosine concentration derived from the ITC data shown in Figure 4-8.....	137
Figure 5-10. Gel filtration chromatography results for hsPNP with the elution profiles for standard proteins used for the column calibration.....	139
Figure 5-11. ITC enzyme inhibition assay scan of hsPNP with the substrate 7-methylguanosine in HEPES buffer, pH 7.0 with 50 mM potassium phosphate, at 25°C.....	141
Figure 5-12. A fit of the Michaelis-Menten model to the hsPNP enzyme reaction rate in the presence of acyclovir as a function of the added 7-methylguanosine concentration derived from the ITC data shown in Figure 4-1.....	141
Figure C-1. Overlaid CD of hsPNP alone and in complex with acyclovir.....	168

List of Abbreviations

ITC – Isothermal Titration Calorimetry

DSC – Differential Scanning Calorimetry

NSAIDs – Non-steroidal Anti-inflammatory Drugs

FLP – flurbiprofen

NAB – nabumetone

NPX – naproxen

2CMP – Cytidine-2'-monophosphate

CBS – 4-carboxybenzenesulfonamide

DMSO – dimethyl sulfoxide

DTT – DL-dithiothreitol

Hepes – N-(2-Hydroxyethyl)piperazine-N'(2-ethanesulfonic acid)

isoform 1 – p38 α MAP Kinase isoform 1 splice variant

isoform 1 C162S – p38 α MAP Kinase isoform 1 with C162S mutation

isoform 2 – wild type p38 α MAP Kinase

isoform 2 C162S – p38 α MAP Kinase isoform 2 splice variant with C162S mutation

CSAIDs – Cytokine Suppressive Anti-inflammatory Drugs

p38 INH.1 – drug-inhibitor of p38 α MAP Kinase; 1-(2,6-Dichlorophenyl)-5-(2,4-difluorophenyl)-7-piperidine-4-yl-3,4-dihydroquinoline-2(1H)-one

SB 203580 – drug-inhibitor of p38 α MAP Kinase; 4-(4-Fluorophenyl)-2-(4-methylsulfinylphenyl)-5-(4-pyridyl) 1H-imidazole

SKF 86002 – drug-inhibitor of p38 α MAP Kinase; 6-(4-Fluorophenyl)-2,3-dihydro-5-(4-pyridyl) imidazo-[2,1-b]-thiazole

Tris – tris[Hydroxymethyl]aminomethane

PNP – Purine nucleoside phosphorylase

hsPNP – Human purine nucleoside phosphorylase

dGTP – deoxyguanosine triphosphate

NDPs – nucleoside diphosphates

dNDPs – deoxynucleoside diphosphates

bsPNP – Calf spleen purine nucleoside phosphorylase

Acyclovir – Acycloguanosine; 9-[(2-Hydroxyethoxy)methyl]guanine

Ganciclovir – 9-[(1,3-Dihydroxy-2-propoxy)methyl]guanine

Chapter 1: Protein-drug Interactions

1.1 Rational Drug Design

Regulation of the diverse functions of enzymes is essential for maintaining the homeostasis of all organisms. Numerous enzymes are involved in controlling individual steps of the complex and interconnected signal transduction pathways. The inability of any organism to naturally regulate enzymes leads to disease conditions. Therefore, the major goal of contemporary drug design is to design small molecules that resemble the natural substrates of enzymes to either inhibit or stimulate their function to potentially help to treat disease conditions. The availability of a three-dimensional (3D) structure of the target enzyme allows for the use of drug-docking methods that computationally determine the optimum orientation of a drug candidate at the target site on the enzyme to maximize its interaction with the enzyme. The identification of a lead drug candidate is an essential step in computational analysis. However, further improvement of the design of the drug requires experimental tests to validate its effectiveness [1]. This experimental validation is particularly important since the drug candidate may not describe all possible binding modes, there may be more than one active site on the targeted enzyme, and other conditions for optimization of its interaction with the target enzyme may be present, such as its transport properties [1].

The increasing number of protein structures available through the Research Collaboratory for Structural Biology Protein Data Bank (RCSB PDB) has allowed for further refinement of the computational algorithms for drug development [2,3]. The criterion for an efficient docking algorithm is whether it can answer unambiguously three main questions: (1) does the lead drug candidate indeed interact with its protein target

site; (2) what is the binding affinity of this interaction, and (3) what is the 3D structure of the drug candidate-target enzyme complex [2]. Drug-docking generates scoring functions which predict the binding affinity of a lead drug candidate to its enzyme target. Drug-docking involves the following sequential series of steps: (1) the surface of each molecule must be defined by a solvent contact surface; (2) input of critical features to match the drug candidate to its target such as shape complementarity and the formation of hydrogen bonds, metal-acceptor bonds, and hydrophobic contacts; (3) a search for drug candidate-enzyme complexes is then performed; (4) a large number of potential drug candidate-enzyme complexes are evaluated in terms of optimal structural features, chemical properties and minimized energy functions; and (5) the docking results are further refined to take into account detailed structural features of the binding sites, including information on structural motifs and structurally conserved residues [2].

Another important property of drug-docking algorithms is consideration of the degree of flexibility in the search for a specific drug candidate-enzyme target complex [2]. The design of an efficient drug-docking algorithm is also associated with difficulties stemming from the high complexity of possible fits to a target binding site since the reference crystal structure represents an average structure and does not account for other possible conformations, and the very common conformational changes that occur upon association, known as “induced fit” [2]. Another challenge for computational drug design is the lack of specificity. According to a recent research article, an increasing number of experimental data suggests that selective drugs for an enzyme target exhibit high binding affinity for other proteins due to the structural similarity between the binding sites [4]. In order to predict “unexpected drug-protein interactions” researchers have developed a

computational method to compare the structure of protein-ligand binding regions [4]. In addition, researchers have used the developed method to predict new drug-enzyme target interactions and have determined binding affinities by performing scoring calculations as well as experimentally confirming some of the predicted interactions [4]. Another proposed method to improve drug design strategies is based on optimizing drug-enzyme target interactions by affecting the energetics of these interactions [5]. Researchers used the so-called “double-decoupling method” to calculate a standard free energy of trapping water molecules in the binding site of drug-enzyme target complexes [5]. Therefore, an important property that should be considered in contemporary drug design is structural features to enable the drug candidates to favorably affect the energetics of a desired interaction by displacing localized water molecules from the enzyme target site. Warren *et al* (2006) evaluated the performance of available docking programs and scoring functions when applied to eight different proteins of seven protein types [3]. They made an important observation that with an increase in the size of the binding site and the complexity of the candidate drugs, fewer docking algorithms succeeded in predicting structures close to the experimentally determined crystal conformations of the drug-enzyme complexes. They concluded that the evaluated docking programs were making the right predictions correlated with experimental data, whereas the scoring functions were less efficient in predicting agreement between the predicted binding affinities and the experimentally-observed binding affinities [3]. Although drug-docking algorithms are effective in reducing the cost and time in developing new drugs, there is a need to further understand experimentally how the energetics of drug binding is affected by displacement of water at the target site, conformational changes to provide an induced fit

of the drug in the target site, and the presence of a second active site on the enzyme target.

1.2 Energetics of Drug Design

The basis for quantifying the energetics of drug-enzyme target interactions is thermodynamics. Thermodynamics is the study of energy transformations and allows for their quantitative characterization. The main concepts of thermodynamics include the system defined as the space of interest and the surroundings described as the region outside the system under investigation [6]. In addition, depending on the characteristics of the boundary between the system and the surroundings the system is defined as open, closed or isolated. An open system can exchange matter as well as energy with the surroundings; a closed system can exchange only energy, whereas an isolated system is separated from the surroundings by an adiabatic boundary, so there is no heat transfer to the surroundings [6]. All the definitions that follow are derived with the assumption of dealing with an isolated system of the following drug (D)-enzyme target (E) interaction,



The energy absorbed or released during a binding reaction is defined as the change in enthalpy, $\Delta_b H$. (A superscript o is added to read $\Delta_b H^o$ when the change occurs under standard conditions of temperature and pressure.) From the First Law of Thermodynamics, the enthalpy is a state function or path-independent function, i.e. it depends solely on the initial and final states of the binding reaction under investigation.

The dependence of the enthalpy change on temperature is defined as the heat capacity change at constant pressure [6] as,

$$\Delta_b C_p = (\partial \Delta_b H / \partial T)_p. \quad (1.2)$$

The spontaneity of any changes occurring during a binding reaction is defined by the change in the entropy, $\Delta_b S$. The entropy is also a state function. According to the Second Law of Thermodynamics spontaneous changes are associated with an increase in the entropy of the system, i.e. changes in the entropy for a binding reaction converting separated reactants(s) to product (s) is positive, $\Delta_b S (\text{total}) > 0$ [6]. The changes in the functions, $\Delta_b H$ and $\Delta_b S$ are equal, respectively, to the enthalpy and the entropy of the drug-enzyme target complex minus the enthalpies and the entropies of the drug and enzyme target,

$$\Delta_b H = H(D \cdot E) - H(D) - H(E) \quad (1.3)$$

Another important state function that takes into account both the enthalpy and the entropy changes when describing the spontaneity of a binding reaction is the Gibbs energy change, $\Delta_b G$, also referred to as the free energy change. The free energy change is related to the enthalpy change and the entropy change through the fundamental equation of thermodynamics,

$$\Delta_b G = \Delta_b H - T \Delta_b S \quad (1.4)$$

where T is the absolute temperature in degrees Kelvin. For a spontaneous binding reaction at constant temperature and pressure $\Delta_b G_{T,p} \leq 0$ [6]. Since the changes in the enthalpy and entropy as a function of temperature with regard to some reference temperature T_0 are

$$\Delta_b H (T) = \Delta_b H(T_0) + \Delta_b C_p(T-T_0) \quad (1.5a)$$

And

$$\Delta_b S(T) = \Delta_b S(T_0) + \Delta_b C_p \ln\{T/T_0\} \quad (1.5b)$$

Then

$$\Delta_b G(T) = \Delta_b H(T_0) + \Delta_b C_p(T-T_0) - \Delta_b S(T_0) - \Delta_b C_p \ln\{T/T_0\} \quad (1.5c)$$

Since for the binding reaction described by equation (1.1),

$$\Delta_b G(T) = \Delta_b G^0(T) + RT \ln\{[E \cdot D]/[E][D]\} \quad (1.6a)$$

and $\Delta_b G(T) = 0$ at equilibrium,

$$\Delta_b G^0(T) = -RT \ln\{K_b\} \quad (1.6b)$$

$$K_b = [E \cdot D]/[E][D] \quad (1.6c)$$

where R is the ideal gas constant and K_b is the equilibrium constant.

1.3 Experimental Drug Design

Both computational techniques together with experimental measurements are key components of rational drug design [2]. The important role of experimental measurements in rational drug design cannot be overstated. For example, many computational approaches focusing on increasing the interactions between the drug and the protein target in drug design neglect enthalpy-entropy compensation, where changes in the enthalpy for a series of similar drugs can be compensated by corresponding changes in the entropy so that changes in $\Delta_b G^0(T)$ are minimized. On the contrary, an excellent example of employing enthalpy-entropy compensation in both computational and experimental methods to improve drug-design strategies has been recently reported by Crespo *et al.* [7]. The researchers recognized the importance of enthalpy-entropy compensation for optimization of the drug binding affinity to its protein target. Most

conventional drug-design methods focus on promoting favorable intermolecular interactions between the drug and its target without consideration of the entropy penalty stemming from the induced fit of the target site to the drug [7]. With this in mind Crespo *et al.* proposed inducing disorder in a protein target as an alternative strategy to increase the binding affinity of a drug to its protein target [7]. The neglect of hydration effects in drug binding interactions such as solvation/desolvation events and ordering/disordering of water near surfaces in an aqueous environment can also substantially affect the predicted drug binding affinities. For example, a study of carbonic anhydrase binding to benzenesulfonamides with different para substituents exhibited an increase in binding affinity with increase in the chain length of the para alkyl chain [8]. When an oligoethylene glycol or oligoglycine chain was substituted for the pure hydrocarbon chain, the binding affinity, instead, did not change with varying the length of the chain because of enthalpy-entropy compensation. Furthermore, the resulting compensatory enthalpy and entropy changes were correctly explained by considering the affects of hydration on the hydrophobic binding interaction between the chain and the enzyme cleft [8]. Another important area where experimental data shows deviations from predictive binding affinities is the effect of salt on possible electrostatic interactions between the drug and protein target in water. Coulomb's law describes the electrostatic interaction between two charged species in vacuum but it must be modified to account for solvation effects in water, since ions in water are highly solvated. Accordingly, the corresponding electrostatic interaction in solution becomes:

$$\Delta E = Z_A Z_B \epsilon^2 / D r_{AB} \quad (1.7)$$

where Z denotes the charges, e denotes the charge of an electron, D is the dielectric constant of the medium and r_{AB} is the distance between the charges A and B.

Equation (1.7) exhibits an inverse proportionality dependence of the electrostatic interaction on the dielectric constant of the medium. Since the presence of ions in solution causes an increase in the apparent dielectric constant of the medium, the addition of small ions such as Na^+ and Cl^- in aqueous solution would, thus, reduce any electrostatic protein-drug interactions [9]. This is particularly important if the binding interactions between a drug and a protein target involve the formation of salt bridges. Ion release into the solution upon binding of a drug to a protein target can substantially effect the change of entropy in the binding reaction, resulting in a change in the binding affinity as observed for DNA binding to proteins [10]. The effects of change in pH is another factor to consider when characterizing protein-drug interactions since different amino acid side chains in the protein's active site as well as functional groups on the drug interacting with the protein have different localized pK_a values. Furthermore, the effects of ion-dipole interactions in water are complicated by interactions between the charged amino acids on proteins as well as their interactions with charges on drugs and on substrates in their transition states during catalysis [8]. For example, the binding of heparin to human antithrombin III (ATIII) is accompanied by a proton transfer to the heparin•antithrombin complex from the solvent and this is particularly apparent in a decrease in the observed binding enthalpy, since tris buffer has a substantial heat of protonation of -47 kJ mol^{-1} [11]. Changes in temperature can also affect drug-protein interactions, since raising the temperature increases the disorder in the system under investigation by altering the mobility of interacting groups on the protein and the drug or

the flexibility of bonds important for the interactions. In addition, the net effects of a temperature change are complicated by the resulting temperature effects on the properties of the solvent environment such as dehydration of the surfaces of the interacting species [12]. The temperature induced disorder of the system may be compensated by corresponding changes in the binding enthalpy through enthalpy-entropy compensation.

1.4 Research Goals of Drug-Protein Interactions

The goal of this research project as described in detail in the subsequent chapters is to characterize drug-protein target interactions experimentally to elucidate how water, salt, temperature, mutagenesis, and the presence of a second substrate influence the thermodynamics of drug-inhibitors binding to their enzyme targets. There are three experimental systems that are the focus of our research efforts. In chapter 3, the results of a study are presented on non-steroidal anti-inflammatory drugs (NSAIDs) binding within the cavities of cyclodextrins as a function of temperature, pH, salt concentration, and size of the cavity to control the amount of water in the interaction. Cyclodextrins are characterized by a simple, rigid, and known structure and have thus, been used to develop and evaluate drug-docking algorithms [13]. In chapter 4, the results of a study on drug-inhibitors binding to p38 α MAP kinase are presented with emphasis on the effects of mutagenesis on these interactions. It was anticipated that the mutagenesis would affect the induced fit of the drug-inhibitor to the protein target. It is shown that the binding affinity for this drug-protein target system increases with the size of the drug-inhibitor through increases in the binding enthalpy [14]. The focus of chapter 5 is the multi-substrate and trimeric enzyme purine nucleoside phosphorylase (PNP), typical of many

regulatory enzymes. Therefore, it presents a more complex framework to investigate drug-protein target binding interaction which consists of binding to each of the subunits of an oligomeric enzyme in the absence or presence of a second substrate binding to an adjacent substrate binding site. Interestingly, the enthalpically or entropically-driven nature of the binding reactions of the different drug-inhibitors to PNP depends on the concentration of the second substrate in solution [15]. In summary, the purpose of my dissertation is to describe the obtained experimental results on the effects of various experimental factors on the energetics of drug interactions with proteins, from the simple cyclodextrin mimics of these interactions, through the more flexible and mutated single-substrate MAP kinase with a single binding site, to the multiple binding sites of the multi-substrate enzyme PNP. The results of this research could be potentially incorporated into a drug-binding data base for use in the development and evaluation of drug-docking algorithms and the ultimate design of more potent drugs.

Chapter 2: Experimental Methods

2.1 Isothermal titration calorimetry

The experimental method used extensively throughout this research is isothermal titration calorimetry (ITC) using a Microcal, LLC VPITC. A schematic diagram of an ITC instrument is presented on Fig. 2-1 along with a typical display of the raw and analyzed data. The instrument consists of two vessels, sample and reference, enclosed in an adiabatic jacket to minimize any heat exchange with the surroundings. The vessels are made of an efficient thermal conducting material, Hastelloy® Alloy and the vessels are connected through circuits to sense any temperature differences between the sample and reference vessels. The ligand for the reaction is placed in the syringe and titrated into the sample vessel filled with the protein solution. Depending on whether the binding reaction is exothermic or endothermic, a change in the thermal power occurs between the two vessels to maintain equal temperatures between the sample and reference vessels. Therefore, the raw data consists of a plot of the differential power exchanged (ΔP) in $\mu\text{cal/sec}$ per the syringe injection as a function of time in s. The total integrated area of the peaks is plotted as a function of the molar $[\text{ligand}]/[\text{macromolecule}]$ ratio to yield a binding isotherm. The thermodynamic parameters of a binding reaction are determined in terms of the binding constant (K_b), the binding enthalpy change ($\Delta_b H$) and the stoichiometry (n) from a fit of an ITC binding model to the binding isotherm. In particular, the areas of the peaks yield a value for $\Delta_b H$ and the slope at the stoichiometric equivalence point n of the molar ratio yields a value for K_b . The binding free energy change ($\Delta_b G$) can be determined from equation (1.6b) and the binding entropy change ($\Delta_b S$) can be determined from equation (1.4). Therefore, a single ITC experiment

provides a complete thermodynamic profile description for a binding reaction at a specific temperature.

ISOTHERMAL TITRATION CALORIMETRY

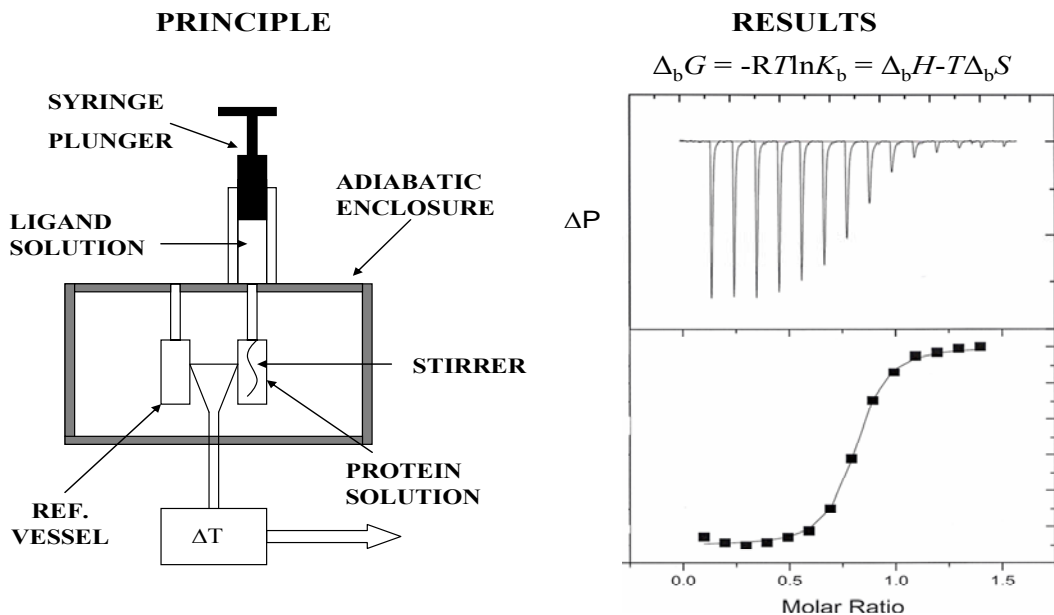


Figure 2-1. Schematic diagram of a typical ITC instrument (left) with raw and analyzed data display (right).

In addition, determination of the $\Delta_b H$ as a function of temperature by performing ITC experiments at different temperatures yields a value for the heat capacity change ($\Delta_b C_p$) characterizing the protein-ligand interaction. Moreover, heats of mixing, dilution and protonation should be taken into account when analyzing the experimental ITC data as recommended by Schwarz *et al.*[16].

The ITC method has found a broad application in the study of protein-drug interactions. An excellent example for the use of ITC is the extensive characterization of the interactions of HIV-1 protease with different inhibitors. Moreover, the binding

energetics of the protease inhibitors have been characterized to address the frequently occurring phenomenon of “drug resistant mutations” with HIV-1 protease [17-21] as well as the important issues in drug-design strategies [22,23]. Another study focuses on characterizing the binding thermodynamics of five different statins with their enzymatic target 3-hydroxy-3-methyl glutaryl coenzyme A reductase (HMG-CoA reductase) [24]. Other important enzyme targets for drug design studied by ITC include stromelysin-1 in cancer and arthritis research, haematin in antimalarial research, PTP-1B, an important protein in signal transduction and cancer studies and isoleucyl-tRNA synthetase in antibacterial research [25]. An additional study on comparing the binding thermodynamics of two structurally similar inhibitors of ribonuclease A, 2’CMP and 3’CMP suggests that even small modifications in the structure of the inhibitors can result in significant changes in the thermodynamic binding parameters [26].

For ITC binding experiments, the practical range of measurable K_b values is limited to 10^3 - 10^8 M^{-1} [27]. Binding constants outside this range are either too high or too low to be reliably determined through this method. An alternative method, called displacement ITC has been described for the determination of binding constants on the order of 10^2 to 10^{12} M^{-1} . The basis of the displacement ITC method is alterations in the binding properties of a ligand in the presence of another competing ligand. This rationale is based on the critical dependence of the shape of the binding isotherm on the unitless constant c which is a product of the binding constant K_b and the concentration of macromolecule in the cell. It has been previously shown that c should be between 1 and 1000, preferably 10 and 100 for reliable measurements of K_b and $\Delta_b H$ [28]. If the c value is too large, the resulting binding isotherm is very steep and rectangular in shape and does

not allow for reliable determination of K_b . If, on the contrary, the c value is too low the binding isotherm becomes too featureless, almost horizontal, to reliably determine K_b and $\Delta_b H$.

2.2 Displacement ITC

Displacement ITC involves an ITC titration to form a weakly bound ligand – protein complex that is followed by titration of a tighter binding ligand into the complex solution to displace the weakly bound ligand [27]. The apparent K_b of the second tighter interaction is lower than the actual K_b of the tighter bound ligand to the protein since the weakly binding ligand competes with the high affinity binding ligand for binding to the protein in the second titration. In order to observe heat exchange during the second displacement titration, there should be differences in the $\Delta_b H$ value of the two ligands [29]. An additional recommendation for a successful displacement ITC experiment is that the higher affinity binding constant under investigation should range two to six orders of magnitude greater than the weaker affinity binding constant [30]. The apparent binding constant (K_{app}) obtained during a displacement experiment is related to the actual binding constant of the high affinity ligand (K_2) through the equation:

$$K_{app} = K_2 / (1 + K_1 [T_1]) \quad (2.1)$$

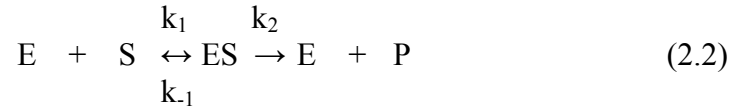
where $[T_1]$ is the concentration of the weaker affinity ligand and K_1 is its binding constant. It is recommended that the ratio $K_2 / (K_1 [T_1])$ be in the range of 10^5 - 10^8 M^{-1} [16]. An example of the use of displacement ITC is the thermodynamic study on inhibitor binding to the catalytic site of glucoamylase G2 where the binding constant for the high affinity acarbose ligand is determined following the initial binding of a weaker affinity

ligand, 1-deoxynojirimycin to glucoamylase G2 [29]. The very high affinity binding constant of the inhibitor KNI-577 to HIV-1 protease was determined from the second titration of the KNI-577 into a solution of the HIV protease complexed with the weaker binding affinity inhibitor acetyl-pepstatin [26]. A recent example is the characterization of the energetics of the binding of three strong somatic angiotensin I-converting enzyme inhibitors by the displacement ITC method through titrations of these inhibitors into complexes of the enzyme complexed with the weakly bound inhibitor L-Asp-L-Phe [31]. Binding interactions weaker than the practical lower limit K_b of the direct ITC technique, 10^3 M^{-1} , can also be determined by displacement ITC measurements [27], as reported previously [26,32,33]. In particular, the binding enthalpies of the weak competitive inhibitor imidazole with K_b on the order of 40 M^{-1} and related compounds to human carbonic anhydrase I have been reliably determined by measurements of the heat of binding of a strong sulfonamide inhibitor to carbonic anhydrase I in the presence of the weak inhibitors [32]. The thermodynamic parameters for two low affinity competitive inhibitors, namely arsenate and inorganic phosphate binding to human protein tyrosine phosphatase 1B have been characterized by displacement ITC [33]. Furthermore, the binding of the low affinity binding inhibitor 5'CMP to ribonuclease A has been characterized by the displacement method from titrations of 5'CMP into solutions of ribonuclease A bound to the more potent inhibitor 2'CMP [26].

2.3 Enzyme kinetics by ITC

The ITC method has also been applied to determine the enzyme kinetic parameters, the Michaelis constant (K_m) and the catalytic constant (k_{cat}) characterizing the

interaction between enzymes and substrates in the absence or presence of inhibitors. Furthermore, all studied reactions followed simple Michaelis-Menten kinetics and involved heat exchange [34,35]. The rate of enzyme-catalysed reactions approaches a maximum rate with increase in the substrate concentration. An enzyme (E)-substrate (S) reaction following Michaelis-Menten kinetics is described by,



in the absence of product inhibition. The change in the concentration of the product (P) or the substrate (S) as a function of time is defined as the reaction rate. Employing the steady-state approximation where the time-dependent change of the ES complex concentration, $d[ES]/dt$, is zero, then

$$d[ES]/dt = k_1[E][S] - k_{-1}[ES] - k_2[ES] = 0 \quad (2.3)$$

where k_1 , k_{-1} , and k_2 are rate constants independent of concentration but dependent on temperature. The Michaelis-Menten equation then defines the reaction rate as:

$$v = V_{\max}[S]/(K_m + [S]) \quad (2.4)$$

where V_{\max} is the enzyme's maximum reaction rate, $[S]$ is the substrate concentration and K_m is the Michaelis constant defined as the substrate concentration necessary to achieve half V_{\max} . The rate of the rate-determining enzymatic step: $ES \rightarrow E + P$ is characterized by the rate constant k_{cat} , such that

$$v = k_{\text{cat}}[ES] \quad (2.5)$$

also known as the turnover number, the maximum number of enzymatic reactions catalyzed per second.

Several enzyme systems following Michaelis-Menten kinetics have been characterized successfully using ITC, namely *H. pylori* urease, trypsin, *E.coli* GroEL chaperonin, *F. heparinum* heparinase, and HIV-1 protease. The generated during the enzymatic reaction thermal power (heat/time) which is directly measured by the calorimeter is directly proportional to the rate of the enzymatic reaction:

$$\text{Rate} = (1/V * \Delta_r H) * dQ/dt \quad (2.6)$$

where dQ/dt is the thermal power generated by the enzymatic reaction, $\Delta_r H$ is an experimentally determined molar enthalpy for the enzymatic reaction, and V is the cell volume [34]. In addition, not only the substrate-enzyme reaction but also the effects of competitive inhibitors for some of the above mentioned enzymes have been experimentally determined by ITC. Competitive inhibitors bind to the substrate site on the enzyme and thus inhibit the rate of the enzymatic reaction. Their inhibition constants can also be determined by ITC since the rate of the enzymatic reaction R_t is related to the inhibition constant K_i of competitive inhibitors through the expression based on Michaelis-Menten kinetics:

$$R_t = (k_{\text{cat}} * [E]_{\text{tot}} * [S]_t) / ([S]_t + K_m * (1 + [I]/K_i)) \quad (2.7)$$

where $[E]_{\text{tot}}$ is the total enzyme concentration and $[S]_t$ is the instantaneous substrate concentration [36].

There is good agreement between enzyme kinetic parameters determined by ITC and those reported in the literature using other experimental techniques [34]. For example, the kinetic parameters K_m and k_{cat} obtained by using ITC for the enzymatic reaction of yeast cytochrome *c* oxidase with its biological substrate ferrocytochrome *c* exhibited good agreement with values of K_m and k_{cat} using the conventional

spectrophotometric technique [35]. Some of the main advantages of using ITC as a general enzymatic assay procedure include that it is an *in situ* measurement that does not require the addition of extraneous reagents [34,35]. ITC is a universal method that does not require specific spectroscopic or chemical properties for the enzymatic assay [34,35]. Furthermore, using calorimetry for enzyme kinetic analysis provides additional information on the energetics of the enzymatic reaction, since it directly determines the reaction enthalpy change ($\Delta_r H$) [35]. However, the enzymatic reactions that can be reliably characterized by ITC should follow the Michaelis-Menten model as described above with its simplifying assumptions. Another important simplifying assumption mentioned above is that the product of the enzymatic reaction does not interact with the enzyme. In particular, the currently available model for analyzing ITC enzyme kinetics data can be applied only in the analysis of enzymatic reactions with no product inhibition. ITC also requires significant heat exchange during the enzymatic reaction for its use in enzymatic assays.

2.4 Differential Scanning Calorimetry

An additional calorimetry method in this research project is differential scanning calorimetry, DSC. A Microcal, LLC VPDSC was used and it consists of a sample and a reference vessel enclosed in an adiabatic jacket to prevent any heat exchange with the surroundings. The two vessels are made of an inert material, Tantaloy 6. As in ITC the temperature difference between the two vessels is monitored as a function of the increase in temperature of the adiabatic enclosure. The raw data consists of monitoring the power

exchange as a function of temperature, which can be converted to a heat capacity change (ΔC_p) as a function of temperature by dividing by the power exchange by the scan rate [37]. A schematic representation of a typical DSC instrument is presented on Fig. 2-2.

DIFFERENTIAL SCANNING CALORIMETRY

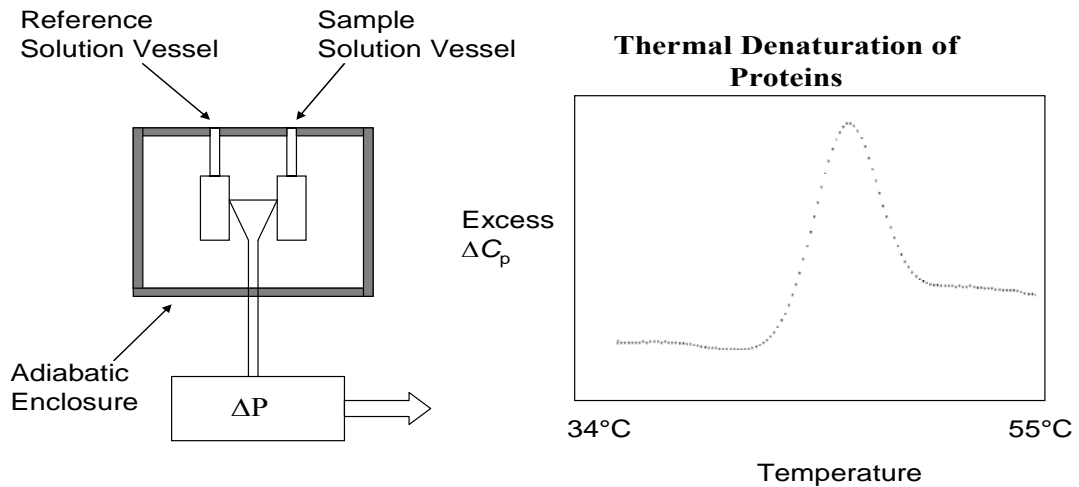


Figure 2-2. Schematic diagram of a typical DSC instrument (left) with raw data display (right).

The broad application of DSC is the determination of the thermodynamics of phase transitions and conformational changes in biological systems [37]. As a protein solution is heated up the protein absorbs heat and undergoes an endothermic unfolding transition. A two-state unfolding transition



where F is the folded state of the protein and U is the unfolded state of the protein is described as an all-or-non transition with no intermediate states [38]. The heat capacity versus temperature data of a DSC scan can be analyzed by fitting a two-state transition model to the data to yield the following thermodynamic quantities: (1) the transition or calorimetric enthalpy ($\Delta_{\text{trs}}H$) from integration of the area under the transition peak per mole of the system under investigation; (2) the transition temperature, T_m where half of the protein is in the unfolded state and (3) the transition heat capacity change ($\Delta_{\text{trs}}C_p$). In addition, the shape of the transition peak as a function of temperature yields the van't Hoff enthalpy ($\Delta_{\text{trs}}H_{\text{vH}}$) for the transition. Moreover, the ratio $\Delta_{\text{trs}}H_{\text{vH}}/\Delta_{\text{trs}}H$ gives information on the cooperativity of the observed transition [37]. If this ratio is close to unity, the unfolding transition can be described as a simple two-state transition, if the ratio is < 1 , intermediate states are involved in the unfolding transition, such is the case of unfolding of a multidomain protein, and a ratio > 1 implies that the protein is an oligomer or aggregated in the folded state. The described analysis of the DSC scan is relevant only if the two-state system under investigation is reversible, i. e. if the unfolding transition reappears upon cooling and subsequent heating. In the case of irreversible transition, the analysis of the system assuming two states is valid only if the thermodynamic parameters are shown to be scan rate independent [38] since when unfolded protein (U) undergoes a slow chemical degradation to form a product I:



then transition parameters are assumed to describe the $F \rightleftharpoons U$ step as described by Manly et al.[38]. This was confirmed by Manley et al. since they observed good agreement between experiment and simulation for the irreversible, scan rate independent

unfolding transition of the *lac* repressor protein both in the absence and in the presence of ligand [38]. Therefore, if a transition appears to be irreversible then the DSC measurements should be performed at different scan rates to determine the applicability of the two-state thermodynamic transition model for analysis. In addition, calibration of the DSC instrument can be performed by measuring the well-studied unfolding thermodynamics of simple globular proteins, such as ribonuclease A, lysozyme, and lactoglobulin [37]. In addition to determination of the unfolding thermodynamics of a protein solution, DSC can be used to characterize protein-ligand interactions. Ligand binding can stabilize either the native (folded) or the unfolded state of the protein, resulting in a shift of the transition temperature to, respectively, higher or lower values relative to that of the protein alone [37]. Binding constant values, which can be directly determined by ITC, can also be indirectly calculated from DSC data, in particular from the temperature shift of the ligand bound complex versus the unbound protein by:

$$1/T - 1/T_0 = (R/\Delta H) * \ln \{1 + ([I_0] - [P_0]/2) * K_b\} \quad (2.10)$$

where T_0 and T are the denaturation temperatures for the protein, respectively in the absence and presence of ligand, ΔH is the transition enthalpy change of the ligand-protein complex, $[I_0]$ and $[P_0]$ are, respectively, the initial inhibitor and protein concentrations, and K_b is the binding constant of the interaction at the transition temperature of the ligand-protein complex. For a detailed derivation of equation (2.8) refer to appendix G. The DSC method has been used to characterize the thermodynamics of the interactions of ribonuclease A with inhibitors, cytidine 3'-monophosphate and uridine 3'-monophosphate at the denaturation temperature. The binding constants and binding

enthalpies of the complexes at the denaturation temperature can be estimated from these parameters and the binding heat capacity change determined at room temperature ([14,39], see chapter 4, equation 4.2). Other examples of the application of DSC to the study of protein-ligand interactions include the study on cAMP and cGMP binding to *E.coli* catabolite activator protein [40], heparin binding human antithrombin [11], various monosaccharides binding to lectins [41], and several disaccharides binding to bovine spleen galectin-1 [42]. Additional information from DSC scans can be obtained from changes in the shape and temperatures of the transitions as well as from the number of transitions observed in a sample solution in the presence of various ligands. Changes in the unfolding profiles of native Heat Shock Protein 90 and its recombinant N- and C-terminal domains upon binding of ATP suggest domain stabilization, since in the presence of ATP the two transition peaks characteristic of the protein unfolding shift to higher temperatures [43]. The binding of tetracycline to the tetracycline repressor affects the unfolding transition of the protein and disrupts specific repressor-DNA interactions through conformational changes. The unfolding transition in the absence of tetracycline shows scan-rate dependence, which disappears upon addition of the ligand and a two-state model could be used to describe the protein unfolding transition [43]. Furthermore, destabilization of the native state of the glucose transporter GLUT-1 is observed upon interaction with ATP, since in the presence of ATP the unfolding transition occurs at a lower temperature [43]. The correlation between protein thermal stability and conformational dynamics induced by anilinonaphtalene sulphonate derivatives binding to bovine serum albumin has been studied by monitoring the shift in the protein unfolding transition upon ligand addition at different concentrations [43]. High binding constants,

up to 10^{20} M^{-1} can be estimated from DSC data, allowing for the characterization of ultratight binding interactions [43]. An extensive study comparing binding constant values determined through simulations and calculations based on DSC data to experimental values has been published [44]. In particular, this correlation method between simulations, calculations and experiment has been developed for the simple 1:1 binding interaction of 2'CMP with ribonuclease and subsequently extended to strongly interacting systems, including trypsin-inhibitor interactions. For most of the investigated systems, there was agreement between the binding constant values obtained through the DSC method and previously reported values using equilibrium techniques. Moreover, the researchers conclude based on simulations that for single-site interactions, binding constants on the order of 10^{40} M^{-1} can easily be estimated by DSC methods [44]. The indirect estimation of binding constants based on temperature shifts makes DSC a valuable technique in primary or secondary drug screening [45]. In particular, DSC instrumentation has been recently adapted by automation for the analysis of 50 samples per day. Moreover, the coupling of the DSC thermal shift method with fluorescence has allowed for a significant increase in the number of investigated interactions per experiment as well as a shorter time per complete experiment [45]. In our research project described in more detail in the following chapters DSC is used to determine the conformational stability of the protein target in the unbound and drug-bound state through measurements of the heat capacity changes in the protein solution as a function of temperature as the protein target undergoes an unfolding transition.

2.5 Fluorescence Spectroscopy

Another technique that gives information about the energetics of protein-drug interactions is fluorescence spectroscopy. However, fluorescence spectroscopy monitors changes on a localized fluorophore in the reaction mixture whereas calorimetry is a global technique. The thermodynamic parameters determined from calorimetry measurements result from all the changes occurring upon drug binding to a protein target such as conformational changes in the protein or possible proton transfer events. On the other hand, fluorescence spectroscopy monitors localized changes, for example the emission properties of aromatic amino acids to describe the entire system under investigation. Fluorescence is a spontaneous emission of radiation which occurs on a nanosecond (10^{-9} s) timescale. Upon excitation the molecule goes from a ground electronic state of lower energy to an excited electronic state of higher energy. Each electronic state is composed of vibrational as well as rotational states and since the lifetime of the molecule in the vibrational levels of the excited electronic state is on the order of picoseconds (10^{-12} s) it rapidly loses energy by collisions with the surrounding molecules and falls to the lowest vibrational level of the excited state. The emission of radiation as a molecule falls from the lowest vibrational level of the excited electronic state to any vibrational level of the ground state gives rise to fluorescence. An important property of fluorescence is that it always occurs at longer wavelength than the absorbance wavelength. The energy is inversely proportional to wavelength according to Planck's law:

$$E = (hc)/\lambda \quad (2.11)$$

where E is the energy of a photon, c is the speed of light, h is the Planck's constant, and λ is the wavelength of radiation. Therefore, longer wavelength would imply lower energy. The longer emission wavelength could be explained by considering the lifetime in the vibrational levels (10^{-12} s) versus the lifetime of fluorescence (10^{-9} s), implying that there would be always some energy lost to nonradiative vibrational relaxations before fluorescence occurs.

A measure of the extent of the emitted energy during fluorescence (F) compared to the absorbed photons (A) is the fluorescence quantum yield, ϕ :

$$\phi = F/A \quad (2.12a)$$

The fraction of photons absorbed can be expressed in terms of the change in incident intensity of the excitation light source, I_0 passing through a small element of space, dx containing a molecule at a concentration c with an absorbance extinction coefficient, ϵ , by the Beer-Lambert law,

$$dF = \phi dI = I_0 \exp\{-\epsilon c x\} dx \quad (2.12b)$$

and the total fluorescence from a cell of depth l is

$$\int dF = \int \phi I_0 \exp\{-\epsilon c x\} dx$$

$$F = \phi I_0 (1 - \exp\{-\epsilon c l\}) \quad (2.12c)$$

Another expression of the Beer-Lambert law is:

$$OD = \epsilon l c \quad (2.12d)$$

where OD is optical density or absorbance of the fluorophore under investigation and

$$OD = -\ln(I/I_0). \quad (2.12e)$$

Therefore, the expression for F can be written as:

$$F = \phi I_0(1 - e^{-OD}). \quad (2.12f)$$

At low concentrations of the fluorophore where $OD < 0.05$ Equation (2.10f) can be expanded in a Taylor Series to read

$$F = \phi I_0 \epsilon lc \quad (2.12g)$$

so that the fluorescence intensity is linearly proportional to the concentration of the fluorophore. Dilute concentrations of the fluorophore have to be used to maintain an optical density < 0.05 [46]. If the concentration of the sample under investigation is too high, the fluorescence will not be linearly proportional to the concentrations and all the incident light will be absorbed at the surface of the cell facing the light source, therefore the signal is not measured uniformly and does not reflect the fluorescence capacity of all the used sample [46]. Furthermore, the linearity between the fluorescence intensity signal and the concentration should be checked in a separate experiment in order to determine appropriate concentrations when designing a set of experiments.

The devices used for measuring the parameters of fluorescence are called spectrofluorimeters. A schematic diagram of a simple spectrofluorimeter setup is shown in Fig. 2-3. In brief, the light from an excitation source passes through a monochromator which transmits light of an adjustable wavelength. A portion of this so called “incident light” is absorbed by the sample and some of the sample molecules fluoresce. Some of this fluorescent light passes through a second monochromator and its intensity is read by a detector usually placed at 90° to the light path to minimize any transmitted or reflected incident light reaching the detector. The detected fluorescence signal is at longer

wavelengths compared to the excitation light wavelength that initially strikes the sample under investigation.

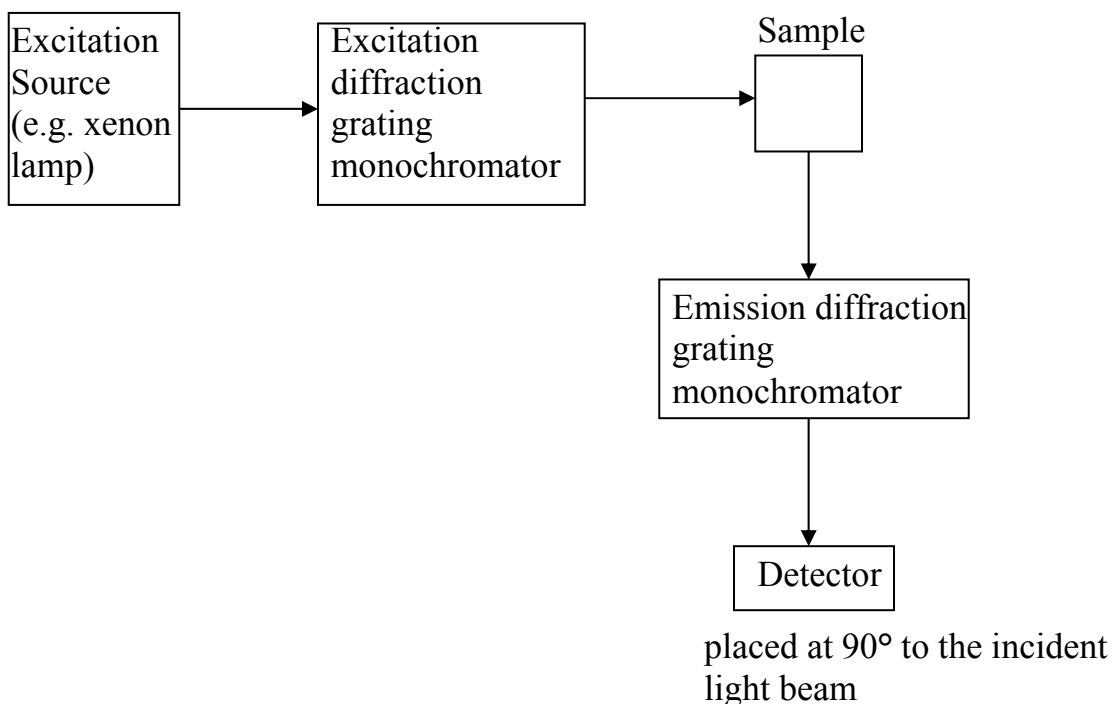


Figure 2-3. Schematic diagram of a spectrofluorimeter.

In the research outlined in the chapters to follow, spectrofluorimetry is used to characterize equilibrium binding interactions as an independent method of ITC for the determination of the binding constants. In addition, the quantum yields and wavelength maxima of drug fluorescence may be affected by the dielectric constant of the solvent environment so that in the high dielectric environment of water the fluorescence ϕ may be reduced and the maximum may be red-shifted to lower energies. These changes can be monitored to determine the binding constant of the drug as well as the change in the water solvent environment of the drug. The analysis of the effect of heparin binding on the intrinsic fluorescence of human antithrombin was used to obtain a binding constant

for heparin binding to antithrombin [11]. The intrinsic fluorescence of proteins is due to aromatic amino acid residues, such as tryptophan (Trp), tyrosine (Tyr), or phenylalanine (Phe). Moreover, the indole groups of the Trp residues are the dominant source of a protein's fluorescence properties. Furthermore, the emission of Trp is very sensitive to its local environment, the hydrophobic interior of the protein or exposure to the solvent environment, and therefore frequently used as a monitor of protein conformational changes [47]. In comparison, the emission of Tyr in native proteins is often quenched due to energy transfer to proximal Trp residues, whereas Phe fluorescence is rarely observed [46]. Calcium binding to calcium-binding proteins, including calmodulin, oncomodulin, troponin C, parvalbumin and α -lactalbumin has been characterized by monitoring the change in the intrinsic fluorescence of the protein [48]. In addition, the binding of indoleacrylic acid, a tryptophan analog causes quenching of the intrinsic protein fluorescence of the tryptophan aporepressor [48]. Furthermore, the binding of the coenzymes, NADH and NADPH to proteins has been characterized by following the increase of the fluorescences of NADH and NADPH, while the binding of haptens causes quenching of the intrinsic tryptophan fluorescence of antibodies [48].

Chapter 3: The role of water in the thermodynamics of drug binding to cyclodextrin

3.1 Abstract

The thermodynamic parameters, $\Delta_b G^\circ$, $\Delta_b H^\circ$, $\Delta_b S^\circ$, $\Delta_b C_p$, of the drugs flurbiprofen (FLP), nabumetone (NAB), and naproxen (NPX) binding to β -cyclodextrin and to γ -cyclodextrin in 0.010 M sodium phosphate buffer were determined from isothermal titration calorimetry (ITC) measurements over the temperature range from 293.15 K to 313.15 K. The heat capacity changes for the binding reactions ranged from $-(362 \pm 48)$ J mol⁻¹ K⁻¹ for FLP and $-(238 \pm 90)$ J mol⁻¹ K⁻¹ for NAB binding to the β -cyclodextrin cavity to 0 for FLP and $-(25.1 \pm 9.2)$ J mol⁻¹ K⁻¹ for NPX binding in the larger γ -cyclodextrin cavity, implying that the structure of water is reorganized in the β -cyclodextrin binding reactions but not reorganized in the γ -cyclodextrin binding reactions. Comparison of the fluorescence enhancements of FLP and NAB upon transferring from the aqueous buffer to isopropyl alcohol with the maximum fluorescence enhancements observed for their β -cyclodextrin binding reactions indicated that some localized water was retained in the FLP- β -cyclodextrin complex and almost none in the NAB- β -cyclodextrin complex. No fluorescence change occurs with drug binding in the larger γ -cyclodextrin cavity, indicating the retention of the bulk water environment in the drug- γ -cyclodextrin complex. Since the specific drug binding interactions are essentially the same for β -cyclodextrin and γ -cyclodextrin, these differences in the retention of bulk water may account for the enthalpically driven nature of the β -cyclodextrin binding reactions and the entropically driven nature of the γ -cyclodextrin binding reactions.

3.2 Introduction

The development of therapeutic strategies is dependent on design strategies for new drugs and on the development of drug-docking algorithms to determine the potency of a specifically-designed drug for its target. To facilitate the design of new drugs, it is important to know how the drug potency or thermodynamic binding affinity is dependent on structural modifications of a new drug. The thermodynamic binding affinity, defined as the free energy change upon the drug binding to its target, is dependent through the fundamental equation of thermodynamics on the binding enthalpy and the binding entropy (see chapter 1, equation 1.4). If, for example, a binding reaction is basically driven by a decrease in the binding enthalpy then structural modifications to enhance this decrease would, presumably, increase the binding affinity. Enthalpy-entropy compensation where additional enthalpic contributions are negated by a compensatory change in the resulting binding entropy, however, would limit the effectiveness of this modification [49-51]. The involvement of water in the binding reaction has been argued as the primary source of enthalpy-entropy compensation [49,52]. An investigation of a well-characterized binding system that would allow for the participation of varying amounts of water would, potentially, elucidate how the binding affinity of a drug is dependent not only on structure but also on the role of water in the binding reaction.

A simple, well-characterized drug binding system that would allow for the participation of varying amounts of water is the binding of the drugs flurbiprofen (FLP), nabumetone (NAB), and naproxen (NPX), shown in Fig. 3-1, to a site in the cavity of a cyclodextrin molecule [51].

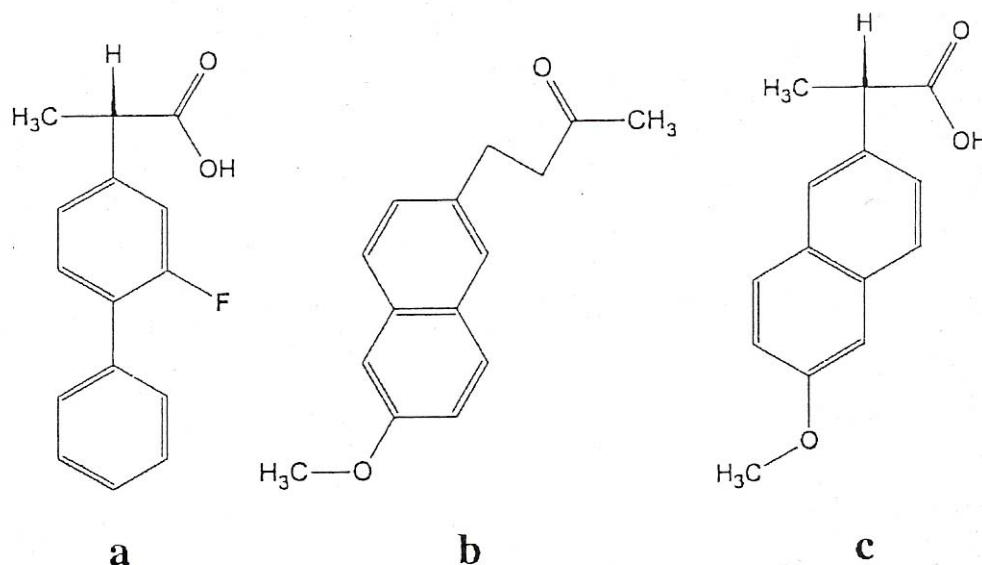


Figure 3-1. Chemical structures of FLP (a), NAB (b), and NPX (c).

The interactions of cyclodextrins with drugs are also known as host-guest interactions and their noncovalent nature, such as hydrogen bonds, van der Waals interactions, dipole-dipole interactions, hydrophobic interactions, or electrostatic interactions makes them a simplified model for studying the complex protein-drug interactions.

A cyclodextrin consists of 6 (α -cyclodextrin), 7 (β -cyclodextrin), or 8 (γ -cyclodextrin) glucose units interconnected to form a hydrophobic tapered cone-shaped cavity for the inclusion binding of small molecules. A schematic representation of a typical cyclodextrin molecule is presented on Fig. 3-2. Naturally occurring as well as chemically modified cyclodextrins are finding increasing applications in the drug, cosmetic, and food industry as inert and nontoxic carriers of active compounds [51]. For example, modified γ -cyclodextrin has been used successfully in delivering hydrophobic fluorescent

phospholipid derivatives from vesicles to cells in culture in order to investigate intracellular phospholipids trafficking [53]. Furthermore, natural cyclodextrins have been reported to possess anti-aggregation properties with application as protein refolding agents. In particular, the refolding of lysozyme and carbonic anhydrase in the presence of cyclodextrins has been characterized [54], and α -cyclodextrin has been reported to prevent aggregation and to function as an artificial chaperone of phosphofructokinase-1 [55]. In addition, cyclodextrins have been successfully used for *in situ* DNA delivery [56]. Some x-ray crystal structures of cyclodextrins complexed with guest molecules have been reported, such as the structure of the inclusion complex between β -cyclodextrin and the O-diglycosyl flavonoid neohesperidin dihydrochalcone [57].

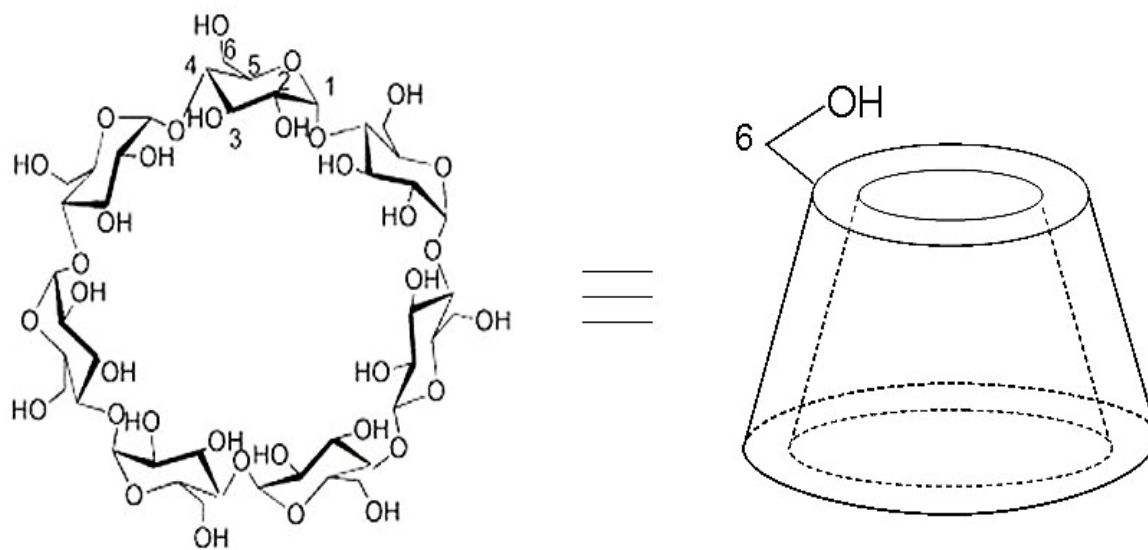


Figure 3-2. Schematic representation of β -cyclodextrin (left) and the most stable three dimensional molecular configuration (right).

The limited number of available structural data for cyclodextrin-guest complexes is compensated by an extensive thermodynamic study on cyclodextrins reported by Rekharsky and Inoue in 1998 [58]. This thermodynamic binding data allows for correlation with computational studies [51]. The drugs under investigation, namely FLP, NAB and NPX belong to the class of non-steroidal anti-inflammatory drugs, or in short NSAIDs. Some additional examples of NSAIDs are aspirin and ibuprofen. The biological target of NSAIDs is the enzyme cyclooxygenase, specifically the COX II isoform responsible for pain and inflammation. One important advantage of NSAIDs is that they are non-narcotic drugs with analgesic, antipyretic and anti-inflammatory effects; in particular they reduce pain, fever and inflammation. These drugs have similarities in structure in that NAB and NPX are substituted naphthalene derivatives with an acetic acid group on NPX while FLP is a substituted biphenyl derivative. This binding system with modifications in the structures of the drugs and in the size of the cyclodextrin cavity would presumably alter the retention of water in the binding interface. The role of water in a binding reaction would presumably be manifested in the heat capacity change of the binding reaction since this thermodynamic parameter has been shown to be attributed to the reorganization of the structure of water upon the transfer of nonpolar groups into the water [52,58]. In addition, since the fluorescence of the drugs in aqueous solution may exhibit significant fluorescence enhancement upon binding inside the hydrophobic interior of the cyclodextrin cavity, the amount of this fluorescence enhancement may be employed to determine the amount of water excluded from the drug-cyclodextrin complex. In fact, the fluorescence enhancement of NAB upon binding in the hydrophobic site of β -cyclodextrin was employed in the determination of the binding constant of NAB

to β -cyclodextrin [6]. The enhancement of drug fluorescence may be compared to the enhancement of fluorescence upon transferring the drug from an aqueous phase with a dielectric constant of 77 at 298.15 K [59] to a more hydrophobic phase with a lower dielectric constant to estimate the amount of water excluded from the cyclodextrin binding site.

A comprehensive review [60] has been published on the binding thermodynamics of up to 1000 small molecules into the cavities of the cyclodextrins at $T = 298$ K. Enthalpy-entropy compensation has indeed been observed for the binding of a variety of small ligands to the cyclodextrins, and the slopes and intercepts of the entropy *versus* enthalpy compensation plots exhibit slight increases in going from α -cyclodextrin to β -cyclodextrin and then to γ -cyclodextrin [61]. The drug binding information on FLP, NAB, and NPX from this review was used to evaluate a drug-docking algorithm developed to predict the binding affinities from structural information [51]. Although drug-docking algorithms have been successful in scoring which structures bind to their targets, there is very little correlation between the docking score and the drug binding affinity [62]. The primary experimental methods employed in these determinations were calorimetry and fluorimetry. Unfortunately, many of the published experimental results were based on assuming that the cyclodextrin concentration is the same as the mass of cyclodextrin added to a known volume of buffer, thereby neglecting the extent of hydration of the cyclodextrin. A more accurate approach would be to assay the *in situ* cyclodextrin concentration in solution. In addition, the FLP, NAB, and NPX binding thermodynamics were not determined as a function of temperature, pH, and salt concentration, experimental variables amenable to drug-docking algorithms.

Thermodynamic drug-cyclodextrin binding data as a function of these experimental variables and based on an *in situ* determination of the cyclodextrin concentration could, thus, provide variable and highly accurate experimental thermodynamic binding data that would mimic the binding of small molecules to their protein targets for the further development and validation of drug-docking algorithms.

The goals of this investigation are twofold: to elucidate the role of water in the binding thermodynamics and to provide highly accurate thermodynamic binding data for FLP, NAB, and NPX binding to cyclodextrin under different experimental conditions. Isothermal titration calorimetry (ITC) measurements were performed on the binding of FLP, NAB, and NPX to β -cyclodextrin and γ -cyclodextrin in 10 mM sodium phosphate buffered solutions as a function of pH from 6 to 8, added sodium chloride concentration from 0 to 0.3 M, and temperature from 293 K to 313 K. These variable experimental conditions provide information on the dependence of the binding affinities on temperature, salt concentration and pH, which are all amenable to the docking computations. The typical binding reaction, exemplified for NPX binding to β -cyclodextrin with a binding constant, K_b is



$$K_b = [\beta\text{CD}\cdot\text{NPX}] / [\beta\text{CD}] [\text{NPX}]. \quad (3.2)$$

An assay based on a decrease in the visible absorption spectrum of phenolphthalein at 550 nm with increase in binding to cyclodextrin was employed to more accurately determine the *in situ* concentration of the cyclodextrin in solution [63]. Any increase in the fluorescence intensity of the drugs in the presence of cyclodextrin was compared to that predicted by a simple binding model predicated on the fluorescence enhancement of

the drug in going from an aqueous to a completely hydrophobic environment upon binding. In addition, agreement between the experimental data and the data from the model would serve to validate the binding constants determined from the ITC measurements. Any departure from this model would presumably be attributed to the retention of water in the complex. If indeed water is retained upon drug binding to the hydrophobic cyclodextrin site, this can be estimated from comparison of the binding fluorescence enhancement with that from transferring the drug from an aqueous solution with a dielectric constant of 80.4 at $T = 273.15$ K to an isopropanol solution with a dielectric constant of 18.3 [59] as representative of the hydrophobic binding environment of the cyclodextrin binding site. The variation of the binding thermodynamic parameters will be compared to the structural modifications of the drugs and to the varying degrees of retention of water in the cyclodextrin binding cavity. The role of water would also be manifested in the heat capacity changes observed in the binding reaction from the dependence of the binding enthalpy on temperature.

3.3 Materials and Methods

3.3.1 Materials

The β -cyclodextrin and γ -cyclodextrin were obtained 0.98 mass fraction purity from Sigma-Aldrich. The FLP, NAB, NPX, and cytidine-2'-monophosphate (2CMP) were also obtained from Sigma-Aldrich and used without further purification. The phenolphthalein, sodium chloride, 100 % ethanol, methanol, isopropyl alcohol, sodium monophosphate, sodium diphosphate, potassium acetate, and potassium chloride were obtained from Sigma-Aldrich. The bovine carbonic anhydrase II and ribonuclease were

obtained from Sigma-Aldrich and used without any further purification. The 4-carboxybenzenesulfonamide (CBS) was obtained from Acros Organics (Morris Plains, NJ).

3.3.2 Determination of the drug concentration in phosphate buffer

Known masses of the drug were dissolved in ethanol and in acetonitrile. The UV absorption spectra were measured for the drug solutions employing a Perkin Elmer UV Lambda 4B Spectrophotometer. Molar extinction coefficients for the drugs in the two solvents were determined from the measured absorptivities and the known mass concentrations of the drug in solution. The extinction coefficients of the drugs in the ethanol and in the acetonitrile, which has a higher polarity than that of the ethanol, were the same as shown in Table 3-1 and, thus, assumed to be the same in the phosphate buffer solutions. The UV optical density measurements of each of the drugs as a function of drug concentration in the different solvents were linear indicating adherence to Beer's Law.

3.3.3 Phenolphthalein assay for cyclodextrin concentration

The assay method was developed by Vikmon [63] and depends on the decrease of the color intensity at 550 nm of phenolphthalein as it binds to the cyclodextrin. A fresh 3.75×10^{-4} M solution of phenolphthalein was prepared by diluting 10 mL of a stock phenolphthalein in ethanol solution to 100 mL with deionized water. A 4.00×10^{-2} M Na_2CO_3 solution in CO_2 free deionized water was also prepared and stored in a closed container. The cyclodextrin solutions in sodium phosphate buffer were prepared at least

two days before the assay to insure complete dissolution of the cyclodextrin and, thus, avoid inconsistency in the assay. To 2 mL of the fresh phenolphthalein solution and 2.5 mL of the Na_2CO_3 solution in a 25 mL volumetric flask was added an appropriate volume from 0.5 mL to 5.0 mL of the cyclodextrin solution to result in final concentrations <0.02 mM upon adding deionized water to bring the total volume of the mixed solutions up to 25 mL at a final pH 10.5. The light absorbance of phenolphthalein at 550 nm in the final diluted mixed solution was measured within 10 min. of mixing in the spectrophotometer and divided by the extinction coefficient of phenolphthalein, $26,000 \text{ M}^{-1} \text{ cm}^{-1}$ in the pH 10.3 to pH 11.2 range to determine the final concentration of free phenolphthalein in the mixture.

Table 3-1. The extinction coefficients of FLP, NAB, and NPX determined in ethanol and in acetonitrile.

	λ/nm	Extinction coefficients in ethanol/ $(\text{cm}^{-1} \text{ M}^{-1})$	Extinction coefficients in acetonitrile/ $(\text{cm}^{-1} \text{ M}^{-1})$
FLP	246.3	$(19.5 \pm 0.4) \times 10^3$	$(18.4 \pm 0.6) \times 10^3$
NAB	228.2	$(79.0 \pm 5.2) \times 10^3$	$(79.3 \pm 0.9) \times 10^3$
NPX	230.6	$(73.4 \pm 2.9) \times 10^3$	$(69.4 \pm 3.0) \times 10^3$

The initial concentration of the free phenolphthalein was determined from the absorbance of a final mixed solution without the added cyclodextrin. Since for β -cyclodextrin, $K_b = 2.16 \times 10^4 \text{ M}^{-1}$ and for γ -cyclodextrin, $K_b = 1.92 \times 10^3 \text{ M}^{-1}$ [63], the relative high concentration of the cyclodextrin insured complete binding to the lower concentration of $3 \times 10^{-5} \text{ M}^{-1}$ for the phenolphthalein. The uncertainty in the measurements is about 3 % arising from the uncertainty in the absorbance measurements and in the imprecision of about 1 % in the volume additions to the mixed solution. The uncertainty in the equilibrium constant was not reported.

3.3.4 Isothermal titration calorimetry measurements

The ITC measurements were performed using a VP ITC from Microcal, Ltd. with the cyclodextrin solution at the higher concentration in the stirrer syringe. The drugs dissolved in the same buffer were contained in the 1.43 mL solution vessel of the ITC. Initially, the cyclodextrin solution was titrated into the buffer solution to determine the heat of dilution of the cyclodextrin solution. After 10 injections, the buffer solution was removed from the solution vessel, the solution vessel rinsed several times with the buffer solution, and the drug solution was then added to the solution vessel. The concentration of the drug solution was about 20 \times lower than that of the cyclodextrin solution in the stirrer syringe. Aliquots from 5 μL to 10 μL , 3 min. apart were titrated into the drug solution until the resulting injections were the same as the heat exchanged for dilution of the cyclodextrin determined in the previous cyclodextrin solution into buffer titration. The titration results were converted to binding isotherms and the heat of dilution was subtracted from the binding isotherm data points prior to fitting a one to one binding

model to the binding isotherm results as described previously [28]. The stoichiometry in the fitting procedure was fixed at 1.00 since the binding affinities were low.

To insure the accuracy of the ITC measurements particularly at different temperatures, calibration of the ITC was performed using two binding systems, the binding of CBS to bovine carbonic anhydrase II in a 20 mM sodium phosphate buffer with 0.150 M NaCl at pH 7.4 and $T = 298.15$ K [64] and the binding of 2'-CMP to ribonuclease A in 0.2 M potassium acetate and 0.2 M KCl buffer at pH 5.5 at $T = 303.15$ K and $T = 311.15$ K [28]. Aliquots of 5 μ L of the 2CMP solution were injected into the 0.0485 mM ribonuclease A solution at $T = 301.15$ K and $T = 311.15$ K. Aliquots of 5 μ L injections of CBS were injected into the 0.056 mM anhydrase II solution at $T = 298.15$ K. The literature CBS binding results are averages of ITC measurements from 14 laboratories and Surface Plasma Resonance measurements from 36 laboratories [64]. The results of the calibration checks are presented in Table 3-2 where they are compared to the literature values. Since there was some dependence of the binding thermodynamic parameters on concentration for 2CMP binding to ribonuclease A [28], the literature values at the 0.04 mM ribonuclease A concentration level were used for the comparison in Table 3-2. For CBS binding to anhydrase II and for the 2CMP binding to ribonuclease A reaction at $T = 311.15$ K, there is good agreement between the calibration results for the ITC employed in this investigation and the same calibration results from other laboratories. Comparison of the ITC calibration results for 2CMP binding to ribonuclease A at $T = 301.15$ K exhibited good agreement for the binding constant. It is not known as to why the binding enthalpies exhibit a large

difference at $T = 301.15$ K. However, the binding enthalpies at $T = 298.15$ K and $T = 311.15$ K do agree with their literature values.

Table 3-2. Comparison of ITC calibrations with the literature values.

n_{exp}	n_{lit}	Exp. K	Lit. K	Exp. $\Delta_b H$	Lit. $\Delta_b H$
		M^{-1}		$kJ\ mol^{-1}$	
(CBS + anhydrase II) at $T = 298.15$ K					
0.86 ± 0.01^a	0.91 ± 0.17	$(1.05 \pm 0.17) \times 10^6$	$(1.06 \pm 0.17) \times 10^6$	-42.1 ± 0.1	-45.2 ± 6.7
(2CMP + ribonuclease A) at $T = 303.15$ K					
1.07 ± 0.01	0.98 ± 0.01	$(9.02 \pm 0.17) \times 10^4$	$(10.0 \pm 1.00) \times 10^4$	-41.6 ± 1.3	-51.2 ± 0.1
(2CMP + ribonuclease A) at $T = 311.15$ K					
1.05 ± 0.01	1.03 ± 0.03	$(4.50 \pm 0.11) \times 10^4$	$(6.91 \pm 1.23) \times 10^4$	-48.8 ± 1.0	-52.7 ± 1.3

^a The literature values for (CBS + anhydrase II) are from reference [64] and for (2CMP + ribonuclease A) from reference [28].

The uncertainties in the binding constant and the binding enthalpy from the ITC measurements were determined from the absolute differences between the experimental data points on the binding isotherm and data determined from the best least squares fit of a one to one binding model with a fixed stoichiometry of 1.00 to the experimental data. These uncertainties would include the uncertainty in the cyclodextrin and the drug concentrations.

3.3.5 Spectrofluorimetry measurements

The three drugs fluoresce in the range from 300 nm to 400 nm in the phosphate buffer solution and in isopropyl alcohol, the latter of which served to mimic the hydrophobic environment of the cyclodextrin cavity. More specifically, the fluorescence of the FLP was excited at 275 nm and the fluorescence was observed from 300 nm to 360 nm with a peak maximum at 313 nm. The fluorescence of the NAB was excited at 262 nm and the fluorescence was observed from 330 nm to 400 nm with a peak maximum at 358 nm. The excitation and fluorescence slit widths were set at 5 nm for NAB and 2 nm for FLP. To insure a near uniform distribution of the fluorescence at right angle to the excitation light and to insure linearity between the fluorescence signal and the drug concentration, the concentrations of the drugs were below the absorbance of 0.10 at the fluorescence excitation wavelength. This was verified by observing a linear dependence of the fluorescence intensity on FLP and on NAB concentration at this absorbance level in the absence of the cyclodextrin. A background fluorescence intensity of just the phosphate buffer alone was first measured and subsequently subtracted from the drug fluorescence intensity. The increase in the fluorescence intensity, $F([CD])$, from F_o , the

drug fluorescence intensity in the absence of cyclodextrin, to a nearly saturated value, $F_f([CD])$, from binding of the drug into the cyclodextrin yields the following fractional increase of the bound drug, $x(F)$:

$$x(F) = (F([CD]) - F_o) / (F_f([CD]) - F_o) \quad (3.3)$$

If this fractional increase were the same as the fractional increase of the drug-cyclodextrin complex concentration, then

$$x = \{ ([CD] + [D] + 1/K_b) - (([CD] + [D] + 1/K_b)^2 - 4[CD][D])^{1/2} \} / 2[D] \quad (3.4)$$

where $[CD]$ is the cyclodextrin concentration in the solution and $[D]$ is the drug concentration in the solution. Detailed derivation of equation (3.4) is presented in appendix F. The experimentally determined fractional increase in the fluorescence intensity was plotted as a function of the cyclodextrin concentration in the solution. With this model, it is expected that the binding constants would be close to the ITC binding constants and so values for K_b from the ITC measurements over a range from $0.3K_b$ to $3.0K_b$ were then used with the known concentrations of the cyclodextrin and the drug in equation (3.4) to determine the calculated value for x at each cyclodextrin concentration. Since the maximum increase in fluorescence intensity corresponding to 100% binding of the drug was not obtainable because of the low fluorescing drug concentrations, the value of $F_f([CD])$ was normalized by dividing this value by the value of x obtained at the highest cyclodextrin and drug concentrations. Ratios of the calculated values x to the experimental values $x(F)$ were then used to calculate a standardized residual deviation between the two sets of values.

The standardized residual is defined as

$$\sigma = \left[\left\{ \sum_{n=1}^N [x/x(F)] \right\} / \{N - 1\} \right]^{1/2} . \quad (3.5)$$

It was observed that the fluorescence intensity in isopropyl alcohol relative to that in the phosphate buffer increased by $(41 \pm 2)\%$ for FLP, by $(77 \pm 4)\%$ for NAB, and by only 6% for NPX. Since the fluorescence increase for NPX is close to the experimental error of approximately 5%, only the FLP and NAB binding reactions to cyclodextrin were monitored by the fluorescence method. The uncertainties in all the fluorescence measurements arise out of uncertainty of about 5 % in the intensity measurements and uncertainty of about 3% in the drug and the cyclodextrin concentrations.

3.4 Results

3.4.1 ITC measurements

The results of a typical ITC experiment of β -cyclodextrin binding to FLP at $T = 298.15$ K along with the corresponding binding isotherm are presented in Fig. 3-3. This titration consisted of titrating 5 μ L aliquots of a 15.8 mM solution of β -cyclodextrin into a 0.285 mM FLP solution in 10 mM phosphate buffer at pH 7.1. The binding reaction is exothermic and the titration peaks following saturation are the same as those observed for titration of the same cyclodextrin solution into just the buffer solution. The heat contributions of these dilutions were subtracted from the observed titration heats to generate the binding isotherm shown in Fig. 3-3. Typical ITC results for β -cyclodextrin binding to NAB and to NPX are presented, respectively, in Fig. 3-4 and Fig. 3-5 and for γ -cyclodextrin binding to FLP and NPX, respectively, in Fig. 3-6 and Fig. 3-7. The figures show typical ITC titrations at different temperatures and different pH levels.

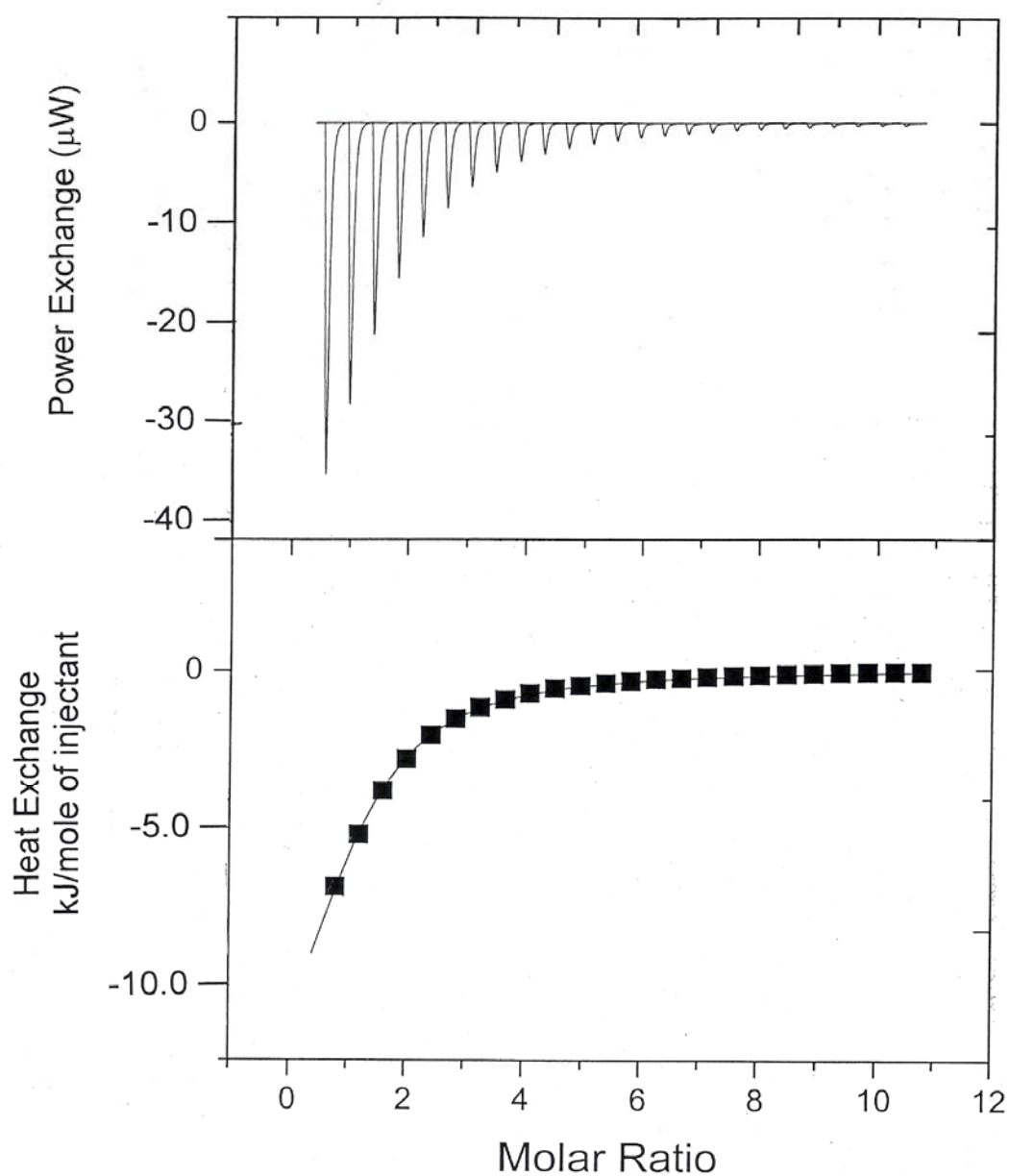


Figure 3-3. ITC scan of FLP binding to β -cyclodextrin. Top: Plot of the power exchange against mole ratio for the ITC titration consisting of 5 μL of 15.8 mM β -cyclodextrin titrated into 0.285 mM of FLP at $T = 298.15\text{ K}$, pH 6.1 and no added salt. Bottom: Plot of the heat exchanged against mole ratio for the binding isotherm and the line represents the best least squares fit of a 1:1 binding model to the binding isotherm data.

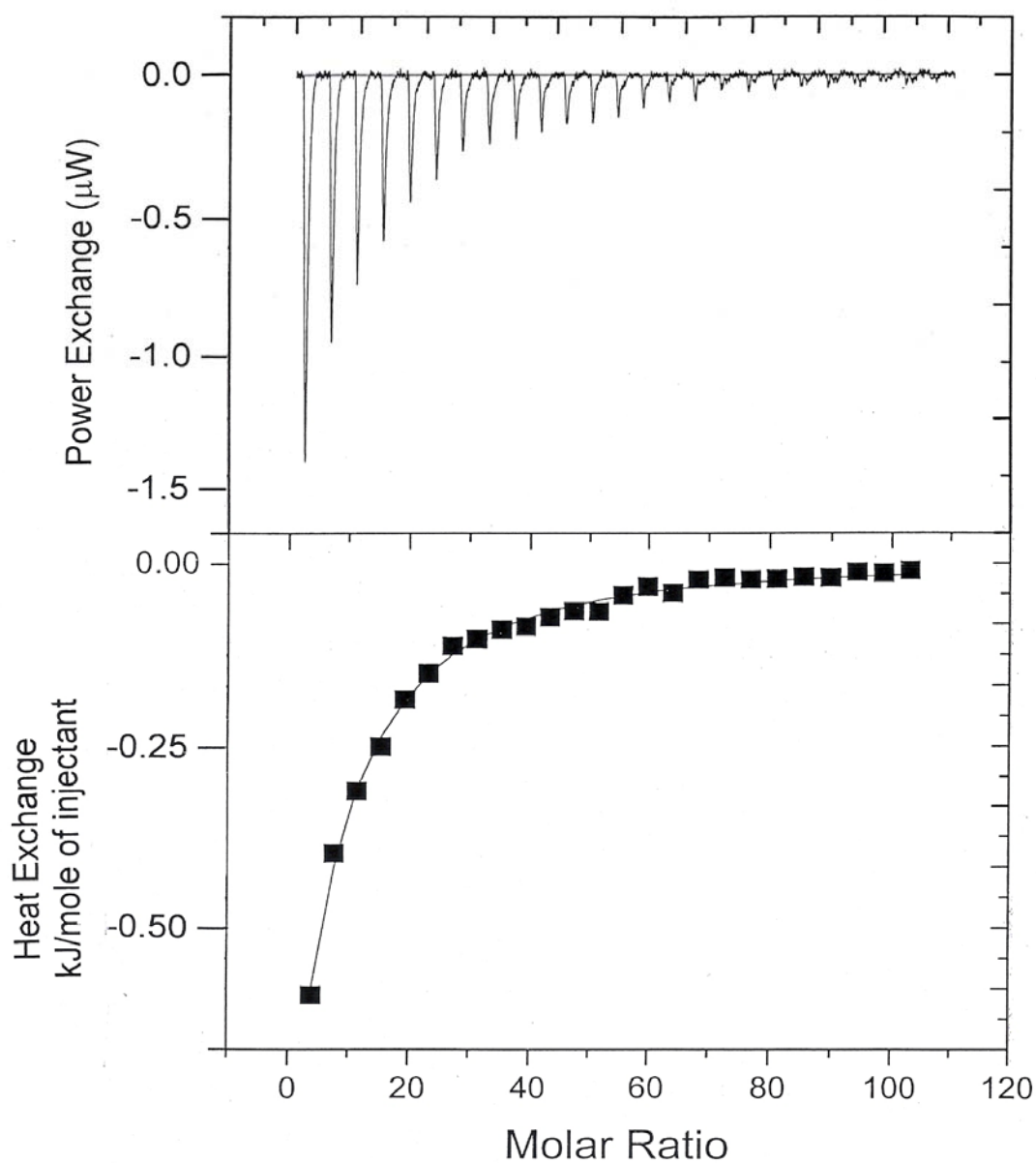


Figure 3-4. ITC scan of NAB binding to β -cyclodextrin. Top: Plot of the power exchange against mole ratio for the ITC titration consisting of 5 μL of 9.66 mM β -cyclodextrin titrated into 0.0182 mM of NAB at $T = 293.15\text{ K}$, pH 7.1 and no added salt. Bottom: Plot of the heat exchanged against mole ratio for the binding isotherm and the line represents the best least squares fit of a 1:1 binding model to the binding isotherm data.

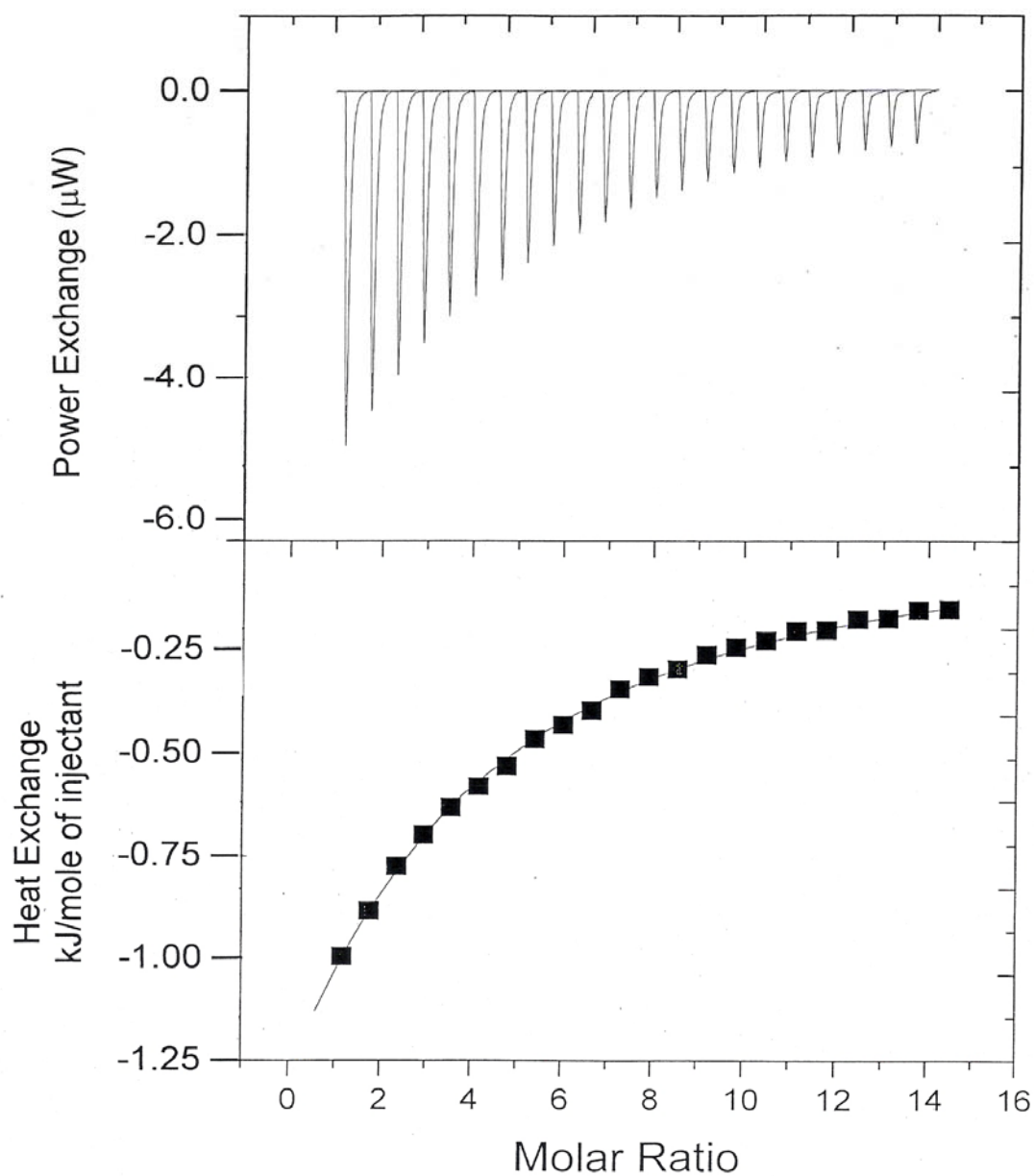


Figure 3-5. ITC scan of NPX binding to β -cyclodextrin. Top: Plot of the power exchange against mole ratio for the ITC titration consisting of 5 μL of 15.8 mM β -cyclodextrin titrated into 0.194 mM of NPX at $T = 298.15\text{ K}$, pH 6.1 and no added salt. Bottom: Plot of the heat exchanged against mole ratio for the binding isotherm and the line represents the best least squares fit of a 1:1 binding model to the binding isotherm data.

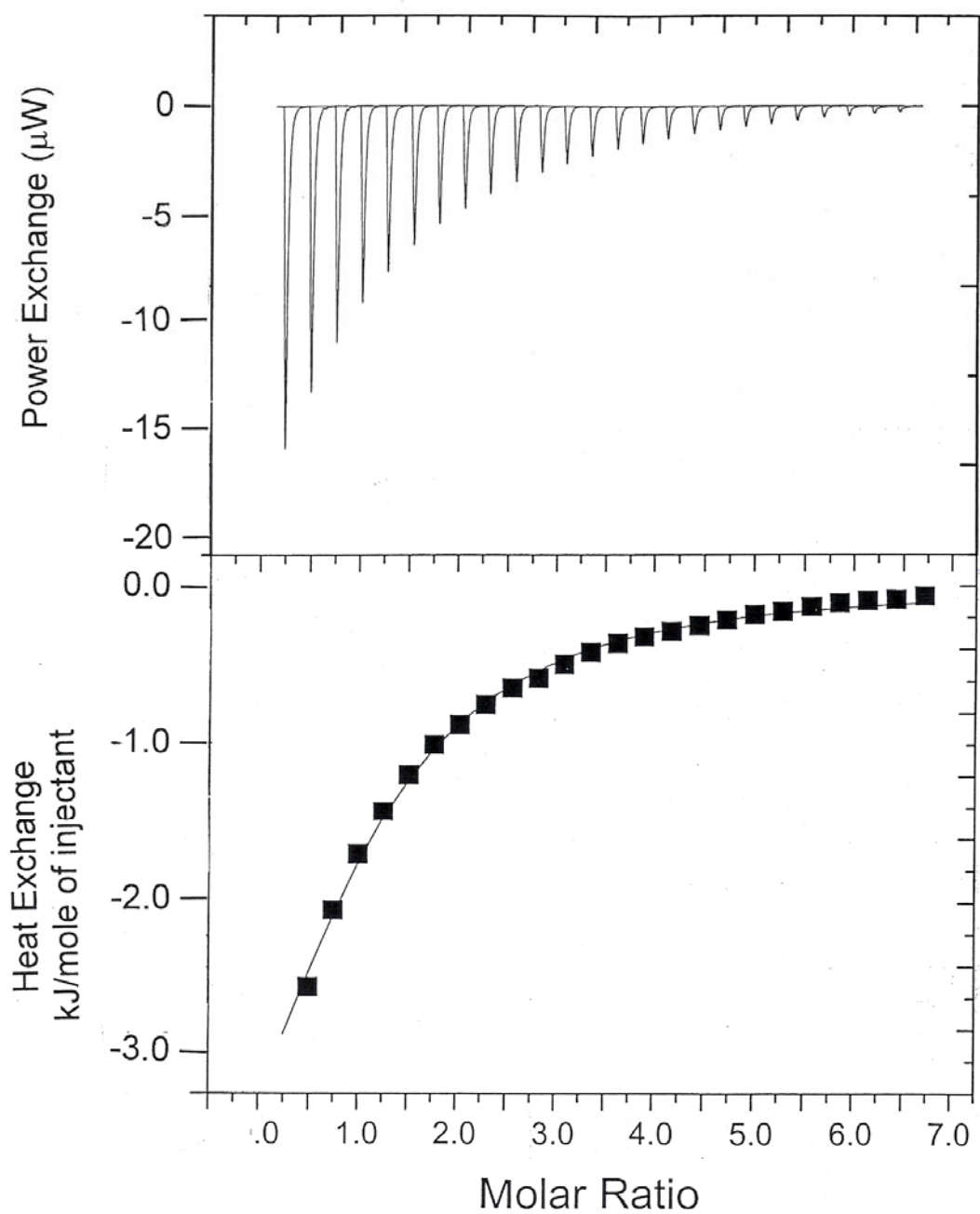


Figure 3-6. ITC scan of FLP binding to γ -cyclodextrin. Top: Plot of the power exchange against mole ratio for the ITC titration consisting of 5 μ L of 19.4 mM γ -cyclodextrin titrated into 0.561 mM of FLP at $T = 298.15$ K, pH 7.1 and no added salt. Bottom: Plot of the heat exchanged against mole ratio for the binding isotherm and the line represents the best least squares fit of a 1:1 binding model to the binding isotherm data.

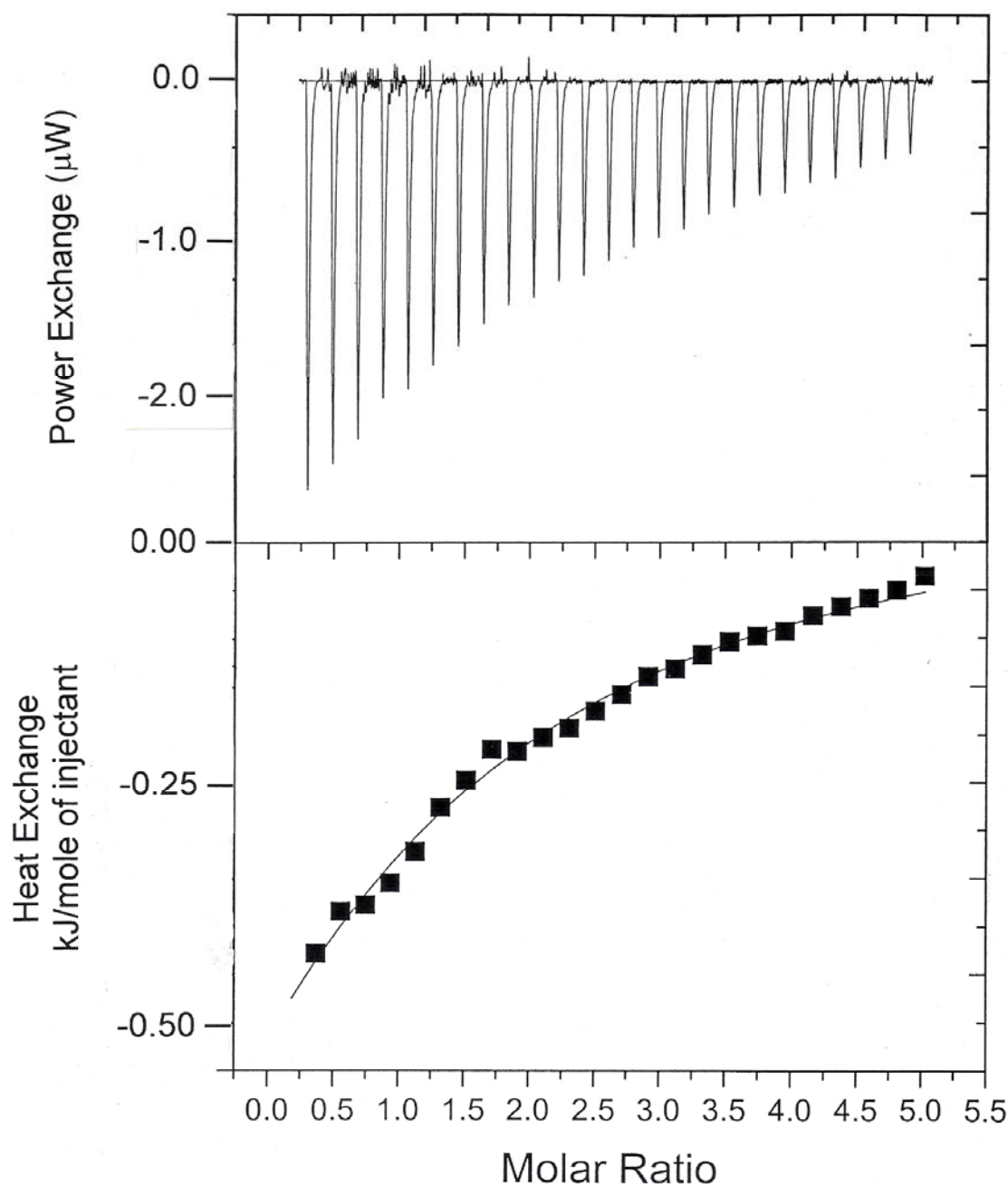


Figure 3-7. ITC scan of NPX binding to γ -cyclodextrin. Top: Plot of the power exchange against mole ratio for the ITC titration consisting of 5 μL of 19.8 mM γ -cyclodextrin titrated into 0.766 mM of NPX at $T = 303.15\text{ K}$, pH 7.1 and no added salt. Bottom: Plot of the heat exchanged against mole ratio for the binding isotherm and the line represents the best least squares fit of a 1:1 binding model to the binding isotherm data.

Only for some of the high affinity binding reactions of β -cyclodextrin to FLP at $T = 298.15$ K, fits of the 1:1 binding model were performed where the stoichiometry was allowed to vary along with K_b and $\Delta_b H^\circ$ in the fitting procedure. It was found that the stoichiometries were 1.00 in these fitting procedures as would be expected for the correct cyclodextrin and FLP concentrations. For the weaker binding affinities of cyclodextrin to NAB and NPX, rapid convergence of the fits was difficult to achieve without fixing the stoichiometry to 1.00. Each fitting procedure, thus, was performed with the stoichiometry fixed at 1.0. The results from the best least squares fit of a 1:1 binding model to the binding isotherm data are summarized in Table 3-3 and Table 3-4 in terms of the binding constant, binding free energy change, binding enthalpy, and the binding entropy. The average values of K_b and $\Delta_b H^\circ$ at each temperature in Tables 3-3 and 3-4 were determined as weighted averages of K_b and $\Delta_b H^\circ$ determined from each of the number of fits indicated in the tables. For the final average values of K_b and $\Delta_b H^\circ$, the weighting factor of K_b and $\Delta_b H^\circ$ determined from each fit was the inverse square root of the uncertainty of each parameter from the fit. Although binding of the smaller β -cyclodextrin was observed for all three of the drugs, ITC measurements were successful with γ -cyclodextrin binding to only FPL and NPX but not to NAB. Very little heat exchange was observed for titrations of the γ -cyclodextrin into the NAB solutions because the γ -cyclodextrin binding enthalpies in general are much lower than the corresponding β -cyclodextrin binding enthalpies by approximately factors of 3 for FLP and 4 to 6 for NPX. This combined with the lower solubility of NAB in the buffer relative to the other two drugs resulted in an exchange of heat close to the noise level of the baseline during the titration.

The binding constants and enthalpies exhibited a decrease with increase in temperature from 293.15 K to 313.15 K with the exception of FLP binding to γ -cyclodextrin, which exhibited very little change in the binding enthalpy with temperature in Table 3-4. The decrease in the binding enthalpy with increase in temperature yielded heat capacity changes of $-(362 \pm 48) \text{ J mol}^{-1} \text{ K}^{-1}$ for FLP binding to β -cyclodextrin, $-(238 \pm 90) \text{ J mol}^{-1} \text{ K}^{-1}$ for NAB binding to β -cyclodextrin, $-(163 \pm 17) \text{ J mol}^{-1} \text{ K}^{-1}$ for NPX binding to β -cyclodextrin, and $-(25.1 \pm 9.2) \text{ J mol}^{-1} \text{ K}^{-1}$ for NPX binding to γ -cyclodextrin. In general, changes in the binding enthalpies with temperature are partially compensated by changes in the corresponding binding entropies.

Table 3-3. Thermodynamics of drug binding to β -cyclodextrin as a function of temperature

Temp.	Conc. Ranges, mM		No.	K_b	$-\Delta_b G^o$	$-\Delta_b H^o$	$\Delta_b S^o$
K	[cyclodextrin]	[Drug]	Det.	10^3 M^{-1}	kJ mol ⁻¹		J mol ⁻¹ K ⁻¹
<hr/>							
<i>FLP</i>							
293.15	7.91	0.0572	2	9.52 ± 0.12	22.3 ± 0.1	14.6 ± 1.9	26.4 ± 3.4
298.15	10.9–17.1	0.0553–0.110	6	4.84 ± 0.28	21.0 ± 0.1	16.5 ± 1.2	15.2 ± 1.1
303.15	9.85–10.1	0.0558–0.060	4	4.69 ± 0.35	21.3 ± 0.2	18.8 ± 1.7	8.37 ± 0.74
308.15	9.85–10.1	0.0560–0.0564	2	4.34 ± 0.19	21.5 ± 0.1	21.2 ± 0.3	0.80 ± 0.01
313.15	10.5–12.5	0.0547–0.0564	4	3.54 ± 0.43	21.2 ± 0.3	21.3 ± 1.4	0.010 ± 0.001
$\Delta_b C_p = -(362 \pm 48) \text{ J mol}^{-1} \text{ K}^{-1}$							
<i>NAB</i>							
293.15	9.66	0.0182	3	3.30 ± 0.36	19.7 ± 0.3	13.3 ± 0.31	22.1 ± 0.6
298.15	9.61–16.9	0.0146–0.0187	7	3.79 ± 0.69	20.4 ± 0.4	11.7 ± 1.9	29.4 ± 4.9
303.15	9.49	0.0189	3	2.94 ± 0.65	20.1 ± 0.1	13.6 ± 2.3	21.6 ± 3.6
308.15	10.3	0.0191	3	2.37 ± 0.54	19.9 ± 0.6	14.7 ± 1.3	16.8 ± 1.6
313.15	9.45	0.0193	3	1.97 ± 0.21	19.8 ± 0.3	17.7 ± 4.0	6.55 ± 1.48
$\Delta_b C_p = -(238 \pm 90) \text{ J mol}^{-1} \text{ K}^{-1}$							
<i>NPX</i>							
293.15	15.4	0.0733	4	0.856 ± 0.074	16.5 ± 0.2	7.80 ± 0.74	29.5 ± 2.8
298.15	13.6–16.9	0.0730–0.153	7	0.698 ± 0.128	16.2 ± 0.5	8.38 ± 0.82	26.3 ± 2.7
303.15	14.2	0.0729	3	0.777 ± 0.062	16.8 ± 0.2	9.17 ± 0.47	25.1 ± 1.3
308.15	14.5–15.0	0.0735–0.0737	6	0.708 ± 0.052	16.8 ± 0.2	9.76 ± 0.64	22.9 ± 1.5
313.15	13.0–14.3	0.0728–0.0730	6	0.636 ± 0.038	16.8 ± 0.2	11.2 ± 0.60	18.0 ± 0.1
$\Delta_b C_p = -(163 \pm 17) \text{ J mol}^{-1} \text{ K}^{-1}$							

Table 3-4. Thermodynamics of drug binding to γ -cyclodextrin as a function of temperature

Temp.	Conc. Ranges, mM		No.	K_b	$-\Delta_b G^\circ$	$-\Delta_b H^\circ$	$\Delta_b S^\circ$
K	[cyclodextrin]	[Drug]	Det.	10^3 M^{-1}	kJ mol^{-1}		$\text{J mol}^{-1} \text{ K}^{-1}$
<i>FLP</i>							
293.15	11.2	0.562	2	2.63 ± 0.02	19.2 ± 0.1	5.88 ± 0.02	45.4 ± 0.1
298.15	11.6–19.4	0.560–0.561	2	1.96 ± 0.09	18.8 ± 0.1	6.03 ± 0.13	42.8 ± 0.9
303.15	11.9–19.5	0.387–0.500	3	1.08 ± 0.31	17.6 ± 0.7	5.84 ± 0.32	38.8 ± 2.7
308.15	10.7	0.391	2	0.980 ± 0.013	17.6 ± 0.1	5.73 ± 0.07	38.7 ± 0.4
313.15	11.0	0.399	2	0.718 ± 0.003	17.1 ± 0.1	6.05 ± 0.09	35.4 ± 0.5
$\Delta_b C_p = 0$							
<i>NPX</i>							
293.15	18.7	0.766	2	0.789 ± 0.012	16.3 ± 0.1	1.55 ± 0.01	50.2 ± 0.1
298.15	18.9–19.8	0.757–0.783	4	0.630 ± 0.048	16.0 ± 0.2	1.57 ± 0.08	48.3 ± 2.5
303.15	19.5–19.8	0.766–0.786	4	0.448 ± 0.100	15.4 ± 0.6	1.89 ± 0.19	44.5 ± 4.9
308.15	20.9	0.765–0.776	3	0.330 ± 0.109	14.9 ± 0.8	2.09 ± 0.25	41.4 ± 5.4
313.15	18.9	0.748	1	0.367 ± 0.030	15.4 ± 0.2	1.92 ± 0.04	43.0 ± 1.0
$\Delta_b C_p = -(25.1 \pm 9.2) \text{ J mol}^{-1} \text{ K}^{-1}$							

The binding thermodynamic parameters were within two standard deviations of their values as the pH increased from 6.4 to 7.8 as shown in Table 3-5. This would be expected since the propanoate groups on the FLP and NPX protonate below pH 4.0 and NAB does not undergo protonation. The binding thermodynamic parameters were within two standard deviations of their values as the added NaCl concentration increased up to 0.30 M as shown in Table 3-6. However, there is a consistent decrease on the binding enthalpies for added salt concentration from 0.15 M to 0.30 M, which are compensated by decreases in the binding entropies so that the binding affinities, $\Delta_b G^0$, remain the same. The parameters in Tables 3-5 and 3-6 were determined as the average of the values derived from at least two ITC runs.

Table 3-5. Thermodynamics of drug binding to β -cyclodextrin at different pHs and $T = 298.15$ K

pH	K_b 10^3 M^{-1}	$-\Delta_b G^\circ$ kJ mol^{-1}	$-\Delta_b H^\circ$ kJ mol^{-1}	$\Delta_b S^\circ$ $\text{J mol}^{-1} \text{ K}^{-1}$
<i>FLP</i>				
6.4 ± 0.1	5.40 ± 0.60	21.3 ± 0.3	17.2 ± 0.2	13.7 ± 0.2
7.1 ± 0.1	4.84 ± 0.28	21.0 ± 0.1	16.5 ± 1.2	15.2 ± 1.1
7.8 ± 0.1	4.27 ± 0.90	21.2 ± 0.3	17.0 ± 2.0	12.4 ± 1.5
<i>NAB</i>				
6.4 ± 0.1	2.39 ± 0.10	19.3 ± 0.1	14.8 ± 1.0	15.0 ± 1.1
7.1 ± 0.1	3.79 ± 0.69	20.4 ± 0.4	11.7 ± 1.9	29.4 ± 4.9
7.8 ± 0.1	2.35 ± 0.53	19.2 ± 0.6	15.0 ± 3.8	14.1 ± 3.5
<i>NPX</i>				
6.4 ± 0.1	0.709 ± 0.100	16.3 ± 0.4	9.69 ± 1.43	22.1 ± 3.3
7.1 ± 0.1	0.698 ± 0.128	16.2 ± 0.5	8.38 ± 0.82	26.3 ± 2.7
7.8 ± 0.1	0.712 ± 0.067	16.3 ± 0.2	8.88 ± 1.13	24.8 ± 3.2

Data at pH = 6.4 and pH = 7.8 are the averages of three determinations.

Table 3-6. Thermodynamics of drug binding to β -cyclodextrin as a function of added NaCl concentration at $T = 298.15$ K

[NaCl]	K_b	$-\Delta_b G^\circ$	$-\Delta_b H^\circ$	$\Delta_b S^\circ$
M	10^3 M^{-1}	kJ mol^{-1}		$\text{J mol}^{-1} \text{ K}^{-1}$
<i>FLP</i>				
0	4.84 ± 0.28	21.0 ± 0.1	16.5 ± 1.2	15.2 ± 1.1
0.15	5.90 ± 0.08	21.5 ± 0.1	18.3 ± 0.6	10.7 ± 0.4
0.30	5.32 ± 0.50	21.3 ± 0.2	18.1 ± 0.6	10.3 ± 0.4
<i>NAB</i>				
0	3.79 ± 0.69	20.4 ± 0.4	11.7 ± 1.9	29.4 ± 4.9
0.15	2.04 ± 0.38	18.9 ± 0.5	13.9 ± 3.1	16.8 ± 3.7
0.30	2.22 ± 0.01	19.1 ± 0.1	15.1 ± 2.4	13.1 ± 2.1
<i>NPX</i>				
0	0.698 ± 0.128	16.2 ± 0.5	8.38 ± 0.82	26.3 ± 2.7
0.15	0.588 ± 0.004	15.8 ± 0.1	10.6 ± 0.2	17.5 ± 0.3
0.30	0.674 ± 0.046	16.1 ± 0.2	10.1 ± 0.82	20.1 ± 1.7

Data at 0.15 mM and 0.30 mM NaCl concentration are the averages of two determinations.

3.4.2 Fluorescence measurements

The fractional increase observed in the fluorescence of the FLP at 313 nm as a function of β -cyclodextrin concentration is shown in Fig. 3-8 along with the closest calculated fractional increase in the inclusion complex. More specifically, the fluorescence of a 56.3 μ M FLP solution, increased to a near constant level by $(18 \pm 1)\%$ as the β -cyclodextrin concentrations increased from (0 to 2.0) mM. This total fractional increase was about 50% of that observed for the fluorescence enhancement of FLP in isopropyl alcohol. In Fig. 3-8, there is less agreement between the experimental and calculated data near the saturation concentration above 1 mM while the calculated data from equation (3.4) are close to the experimental data below 1 mM. The best agreement between the fractional experimental and the calculated fluorescence increases for FLP was determined at a binding constant value of 4930 M^{-1} , which is within two standard deviations of the average ITC determined binding constant of 5900 M^{-1} . The FLP fluorescence intensities in the presence of increasing concentrations of γ -cyclodextrin exhibited a monotonic increase but never approached saturation as observed for binding to β -cyclodextrin and predicted by the simple binding model of equation (3.4).

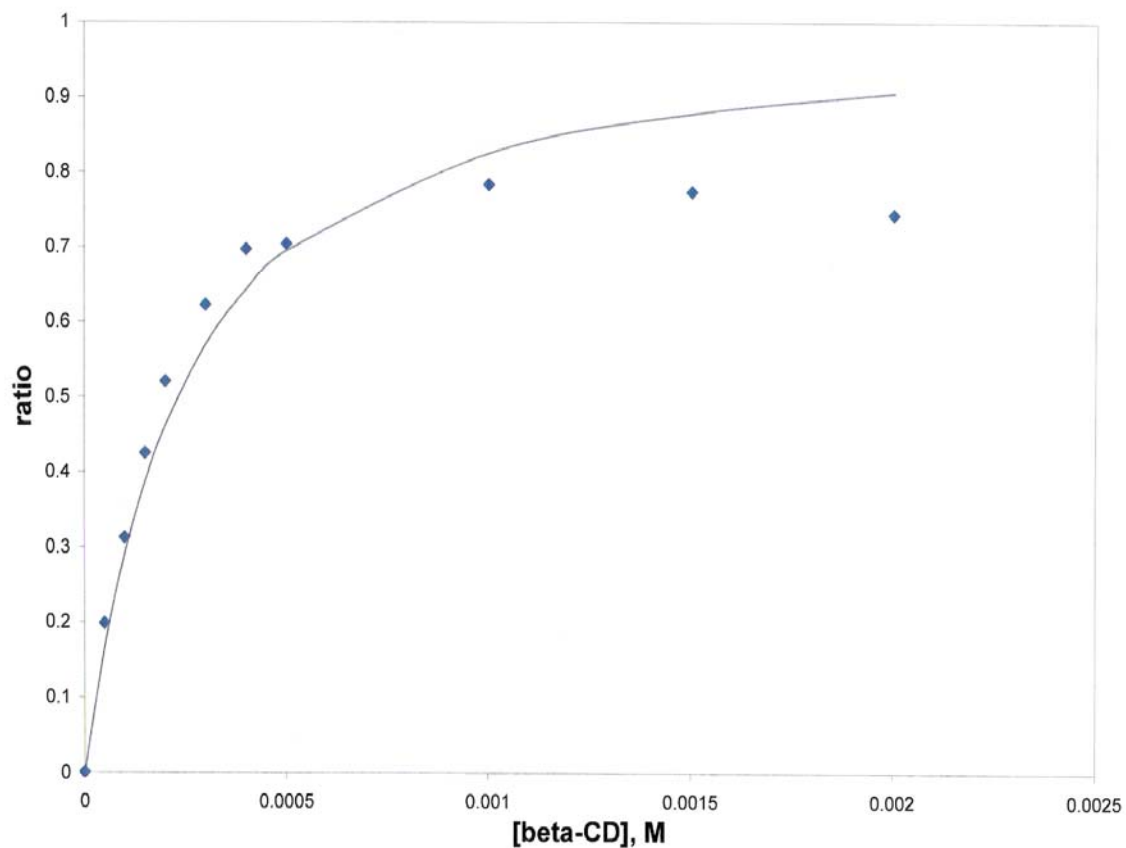


Figure 3-8. Plot of the fluorescence intensity as a ratio for the 56 μM FLP in phosphate buffer against the added β -cyclodextrin concentration at $T = 298$ K. The points are the experimental data and the line represents the calculated value from equation (3.4) in the text.

The fractional increase observed in the fluorescence of the NAB at 358 nm upon addition of β -cyclodextrin in the solution is shown in Fig. 3-9 along with the closest calculated fractional increase using a binding constant of 7580 M^{-1} , twice as great than the binding constant of 3790 M^{-1} from the ITC measurements at $T = 298.15 \text{ K}$. The fluorescence of a $16 \text{ }\mu\text{M}$ NAB solution increased by $(90 \pm 5)\%$ as the range of β -cyclodextrin concentrations increased from (0 to 2.0) mM. This increase to the NAB fluorescence saturation level with twice its uncertainty is the same as the $(77 \pm 3)\%$ fluorescence increase in isopropyl alcohol. In Fig. 3-9, the experimental data at the saturate concentration above 1 mM β -cyclodextrin exhibit a constant 10 % higher value than the calculated data. The cause of this discrepancy is not known although below 0.5 mM β -cyclodextrin, the experimental data are close to the calculated data from equation (4). The fluorescence intensities of NAB in the presence of increasing concentrations of γ - cyclodextrin from (0 to 3) mM were the same and followed by a decrease as the γ -cyclodextrin concentration increased to 15 mM, in contrast to the behavior predicted by equation (3.4).

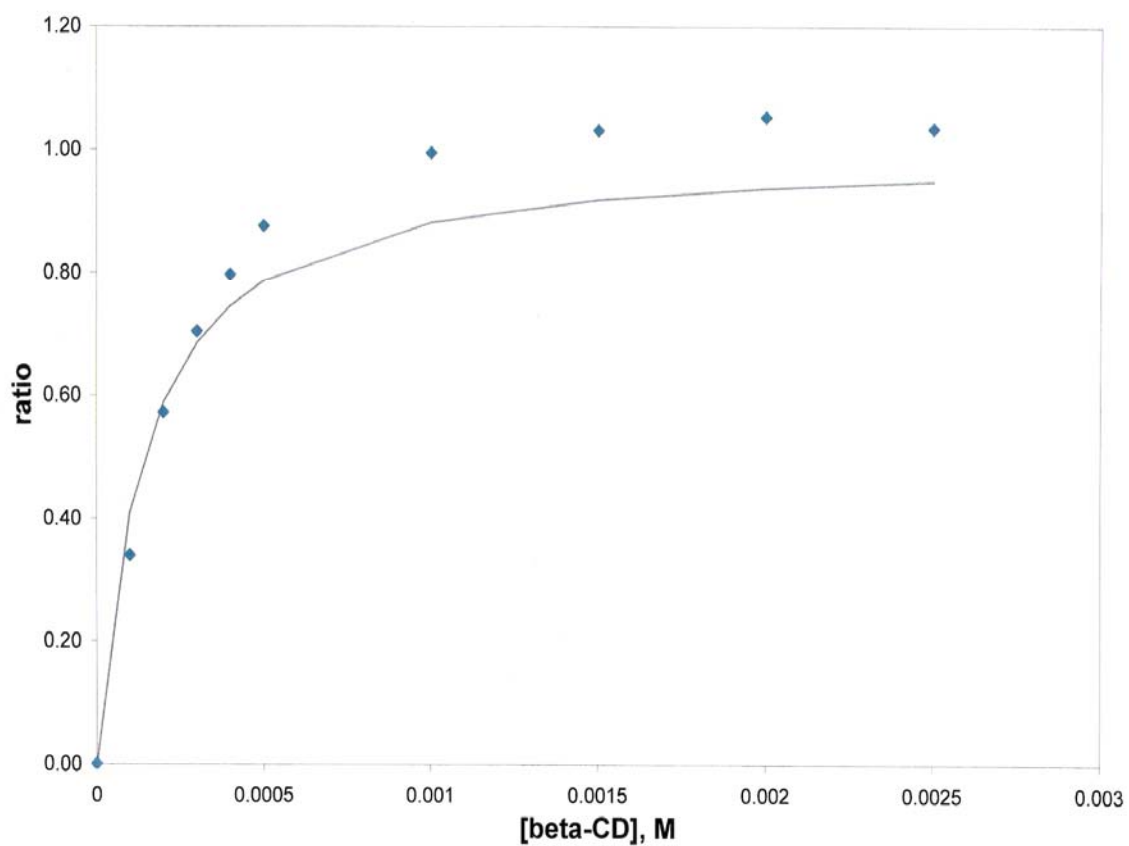


Figure 3-9. Plot of the fluorescence intensity as a ratio for the initial $18 \mu\text{M}$ NAB in phosphate buffer against the added β -cyclodextrin concentration at $T = 298 \text{ K}$. The points are the experimental data and the line represents the calculated values from equation (3.4) in the text.

3.5 Discussion

It is assumed that the effective role of water in the binding reactions would be different for drug binding inside the β -cyclodextrin cavity than for drug binding into the larger 40 vol% bigger γ -cyclodextrin cavity. This is evident in the fluorescence results where a change from the aquatic environment of FLP and NAB to an almost completely hydrophobic environment in the β -cyclodextrin cavity follows the simple model predicted by equation (3.4), while no such predictive behavior is observed for binding inside the larger γ -cyclodextrin cavity. Although the maximum enhancement of the NAB fluorescence in the NAB- β -cyclodextrin complex is the same as for the transfer of NAB from water to isopropyl alcohol, the maximum enhancement of the FLP fluorescence in the FLP- β -cyclodextrin complex is only about 50% of the enhancement observed for the transfer of FLP from water to isopropyl alcohol. This would imply that about 50% of the cyclodextrin localized water is still retained in the FLP- β -cyclodextrin complex while almost no water is retained in the NAB- β -cyclodextrin complex.

The effective role of water in the binding reactions is also apparent in differences in the heat capacity changes between the β -cyclodextrin and the γ -cyclodextrin drug binding reactions. For the β -cyclodextrin binding reactions, heat capacity changes of $-(362 \pm 48) \text{ J mol}^{-1} \text{ K}^{-1}$ for FLP, $-(238 \pm 90) \text{ J mol}^{-1} \text{ K}^{-1}$ for NAB, and $-(163 \pm 17) \text{ J mol}^{-1} \text{ K}^{-1}$ for NPX are observed whereas the heat capacity changes of the γ -cyclodextrin binding reactions are almost an order of magnitude lower, $-(25.1 \pm 9.2) \text{ J mol}^{-1} \text{ K}^{-1}$ for NPX and 0 for FLP. Since heat capacity changes in binding reactions are attributed to water reorganization upon transference of the drug from bulk water to its binding site [52,58], it is apparent that less reorganization of the water occurs

with drug binding to γ -cyclodextrin than with binding to β -cyclodextrin, implying that the original bulk water structure is retained after drug binding in the larger γ -cyclodextrin cavity. Part of the heat capacity changes may be attributed to changes in the vibrational modes of the cyclodextrin upon binding of the drug but it is expected that these contributions are minor relative to that of water reorganization upon drug binding to the cyclodextrin [52]. In accordance with the heat capacity changes arising out of reorganization of the bulk water structure and since the heat capacity change for the FLP- β -cyclodextrin binding reaction is the same as that of the NAB- β -cyclodextrin binding reaction, the retention of some water in the FLP- β -cyclodextrin complex would imply that this water is not part of the bulk water structure but localized water molecules.

The effective roles of water in the drug-cyclodextrin complexes are not only dependent on the size of the binding site but also on the structural details of the drug. All three drugs are predicted to bind with their long aromatic axis nearly aligned along the central long axis of the β -cyclodextrin and γ -cyclodextrin cavities with much less distortion of the estimated 40 vol% larger γ -cyclodextrin cavity [51]. There is a “snug” fit of the drugs inside the smaller β -cyclodextrin cavity where the binding reactions are exothermic and basically enthalpically-driven, 80 % for FLP, 60 % for NAB binding and 50 % for NPX binding at $T = 298.15$ K. The free rotation of the two benzene rings around the main axes of the biphenyl of FLP, unhindered by the small ortho fluorine on FLP, would facilitate the snugness of the fit as well as the van der Waals interactions between FLP and β -cyclodextrin cavity [51] and this would account for the higher enthalpic contributions to the binding affinity of FLP. The free rotation of the two benzene rings from steric considerations and the acetyl group would presumably allow for the retention

of some localized water in the FLP- β -cyclodextrin complex. In contrast, the naphthalene group of NAB and NPX is more rigid and, thus, may hinder the van der Waals interactions between the naphthalene and the β -cyclodextrin [51] and this would account for lower enthalpic contributions to the β -cyclodextrin binding affinities of NAB and NPX. The rigidity of the naphthalene ring from steric considerations and the replacement of the propanoate group on the NAB by nonpolar butanone would presumably increase the exclusion of water from the NAB- β -cyclodextrin complex. Since there is a lack of any effect of added salt concentration on the FLP and NPX binding affinities in Table 3-6, any electrostatic contributions from the propanoate group on FLP and NPX are presumably negligible. Since the γ -cyclodextrin cavity is estimated to be about 40% larger in volume than the β -cyclodextrin cavity, there would be a higher probability of inclusion of bulk water in the binding interactions within the γ -cyclodextrin cavity. The binding interactions in the larger γ -cyclodextrin cavity are indeed weaker and in contrast to the binding reactions with β -cyclodextrin, are basically entropically-driven, 67% for FLP binding and 90% for NPX binding. The entropically driven nature of the binding reactions in γ -cyclodextrin result from a decrease in the magnitude of the binding enthalpies by a factor of almost 3 for FLP and almost 6 for NPX and an increase in the binding entropy by a factor of 2 to 3 relative to their corresponding values for β -cyclodextrin. The decrease in the magnitude of the binding enthalpies can be attributed to the retention of the water in the drug- γ -cyclodextrin cavity allowing for a “looseness” of the drug fits in the γ -cyclodextrin cavity. The increase of the entropic component may be attributed to this looseness in terms of a higher configurational entropic contribution,

ΔS_{conf} , in the γ -cyclodextrin binding affinity as well as changes in the solvent entropic contribution, ΔS_{solv} , since [3]

$$\Delta S_{\text{exp}} = \Delta S_{\text{conf}} + \Delta S_{\text{solv}}. \quad (3.6)$$

Calculated values for the change in configurational entropy were computed from the probability density of the configuration associated with the molecular coordinates of the cyclodextrin-drug complex and consisted only of changes in the rotational and translational entropy [51]. The calculated configurational entropy was computed along with calculated values of the average energy to yield the free energy changes presented in Table 3-7, which are close to the experimentally determined ITC values [51].

Table 3-7. Comparison of ΔG° values with the literature values

Cyclodextrin	$\Delta G^\circ(298\text{K})/$ (kJ mol ⁻¹)	$\Delta G^\circ(\text{lit exp})/$ (kJ mol ⁻¹)	$\Delta G^\circ(298\text{K}) (\text{lit calc})/$ (kJ mol ⁻¹)
<i>FLP</i>			
β -cyclodextrin	21.0 ± 0.1	20.8, 18.8	22.6
γ -cyclodextrin	18.8 ± 0.1	19.9	22.9
<i>NAB</i>			
β -cyclodextrin	19.7 ± 0.3	19.2 ($T = 293\text{ K}$)	21.9
<i>NPX</i>			
β -cyclodextrin	16.2 ± 0.5	18.1 ($T = 295\text{ K}$)	18.9
γ -cyclodextrin	16.0 ± 0.2		17.9

Experimental literature (lit exp) values are from reference [65]. Calculated literature (lit calc) values are from reference [51].

The increases in ΔS_{exp} in going from β -cyclodextrin to γ -cyclodextrin binding at $T = 298.15\text{ K}$ are $(27.6 \pm 1.4)\text{ J mol}^{-1}\text{ K}^{-1}$ for FLP and $(22.4 \pm 3.7)\text{ J mol}^{-1}\text{ K}^{-1}$ for NPX from Tables 2-3 and 2-4. Since calculated increases in ΔS_{conf} in going from β -cyclodextrin to γ -cyclodextrin binding at $T = 298.15\text{ K}$ are $64.3\text{ J mol}^{-1}\text{ K}^{-1}$ for FLP and $45.5\text{ J mol}^{-1}\text{ K}^{-1}$

for NPX [51], then differences in ΔS_{solv} in going from β -cyclodextrin to γ -cyclodextrin binding are $-(36.7 \pm 1.8) \text{ J mol}^{-1} \text{ K}^{-1}$ for FLP and $-(23.1 \pm 3.8) \text{ J mol}^{-1} \text{ K}^{-1}$ for NPX. Specifically, the solvation entropy differences increase by $(36.7 \pm 1.8) \text{ J mol}^{-1} \text{ K}^{-1}$ for FLP binding to β -cyclodextrin and by $(23.1 \pm 3.8) \text{ J mol}^{-1} \text{ K}^{-1}$ for NPX binding to β -cyclodextrin. Interestingly, this increase is close to the isocratic entropy increase of $33.4 \text{ J mol}^{-1} \text{ K}^{-1}$ for a hydrocarbon transferring from water into its pure liquid phase. This would be analogous to a drug going from a pure aqueous phase into a pure hydrophobic site in the cavity of the β -cyclodextrin whereas such a transfer does not occur for drug binding inside the γ -cyclodextrin cavity with its retention of the bulk water structure.

The lack of any differences to within experimental error between the heat capacity changes for FLP and NAB binding to β -cyclodextrin reactions and the retention of some water in their FLP- β -cyclodextrin complex as indicated by the fluorescence measurements can be attributed to the same reorganization of the bulk water structure excluded from the β -cyclodextrin cavity upon binding. For the drug- γ -cyclodextrin binding reactions, most of the bulk water structure is probably retained within the larger drug- γ -cyclodextrin complex resulting in very little heat capacity change. Hence, the retention of the bulk water structure in the γ -cyclodextrin binding site would not only reduce the enthalpic contributions to the binding affinities but would also minimize the effect of temperature on the binding reaction whereas for binding of the drug inside the smaller β -cyclodextrin cavity, the drug is removed from the bulk water structure and reorganization of the water occurs. Interestingly, the retention of individual water molecules in the FLP- β -cyclodextrin complex may play a contrary role and contribute to the enthalpy of the FLP- β -cyclodextrin binding affinity as observed for lysozyme

antigen-antibody binding [66]. Such retention of water has long been shown to be important in the binding thermodynamics of proteins and should be taken into account in the development of drug-docking algorithms [67]. Even here in the simple case of drug binding in the cyclodextrin cavity, water plays an important role in the binding thermodynamics.

The ITC results show that the binding constants range from 367 M^{-1} for NPX binding to γ -cyclodextrin at $T = 313.15 \text{ K}$ to 9520 M^{-1} for FLP binding to β -cyclodextrin at $T = 293.15 \text{ K}$, over a factor of almost 30, and, thus, a viable range of values for validating binding affinities calculated from the docking algorithms. A comparison between the ITC results and both literature and calculated values of $\Delta_b G^\circ$ is presented in Table 3-7. While the literature experimental values are close to the values determined in this investigation, the calculated values are more negative by about 5%, within the standard deviation of the average value of $\Delta_b G^\circ$. Furthermore, the lack of any dependence of the binding affinities on pH and salt concentration would indicate that the binding affinities are not critically dependent on the make-up of the buffer. This lack of dependence should also be reflected in application of newly developed docking algorithms to these data.

Chapter 4: Effect of the distal C162S mutation on the energetics of drug binding to p38 α MAP kinase

4.1 Abstract

The binding reactions of the inhibitor drugs, SB 203580, SKF 86002, and p38 INH.1 to the isoforms 1 and 2 splice variants of p38 α MAP kinase and their C162S mutants, as determined from ITC measurements from 25 to 35°C, are totally enthalpically driven with binding constants ranging from 10^7 M^{-1} for SKF 86002 and SB 203580 to 10^9 M^{-1} for p38 INH.1. Interactions of p38 INH.1 with an additional hydrophobic pocket of the kinase would account for its large increase in K_b . DSC scans exhibited single unfolding transitions for the isoforms, their mutants, and the mutants bound to the drug-inhibitors. Two transitions, however, were observed for the isoform-drug complexes of SB 203580 and p38 INH.1 and were attributed to decoupled unfolding of the N- and C-terminal domains of the kinase. The C-terminal domain of isoform 1 is estimated to be less stable than of isoform 2 by 15 kJ mol^{-1} .

4.2 Introduction

p38 mitogen activated protein (MAP) kinase is a member of the MAPK family. MAP kinases or mitogen-activated protein kinases are the third main component of a phosphorylation cascade that gets activated by diverse environmental changes, such as growth factors, cytokines, as well as environmental stresses, such as osmotic shock, heat shock, or ultraviolet radiation [68,69]. MAPKs comprise four well-characterized subfamilies: (1) the extracellular-signal-regulated kinases or in short ERKs, in particular ERK1/2; (2) ERK5; (3) JUN N-terminal kinases (JNKs) and (4) p38 kinases [68,69].

MAPKs are serine/threonine kinases, or in other words enzymes that catalyze the phosphorylation of serine or threonine residues in proteins [68]. MAPKs get activated by dual phosphorylation on conserved threonine and tyrosine residues by the upstream MAP kinase kinases (MAPKKs) which on their part get activated by phosphorylation by the serine/threonine upstream MAP kinase kinase kinases (MAPKKKs) [68]. A schematic diagram of the MAPK signaling cascade is presented on Fig. 4-1. p38 MAP kinase regulates skeletal muscle formation or myogenesis [70], has been implicated in the regulation of apoptosis in macrophages [71,72], and promotes the production of proinflammatory cytokines, e.g. interleukin-1 and tumor necrosis factor- α , produced during prolonged or chronic inflammation [73-75]. The involvement of p38 MAP kinase in the immune response leading to inflammation has been studied most extensively since this kinase is an attractive target for the design of potent and selective inhibitors that would enable the production of anti-inflammatory drugs.

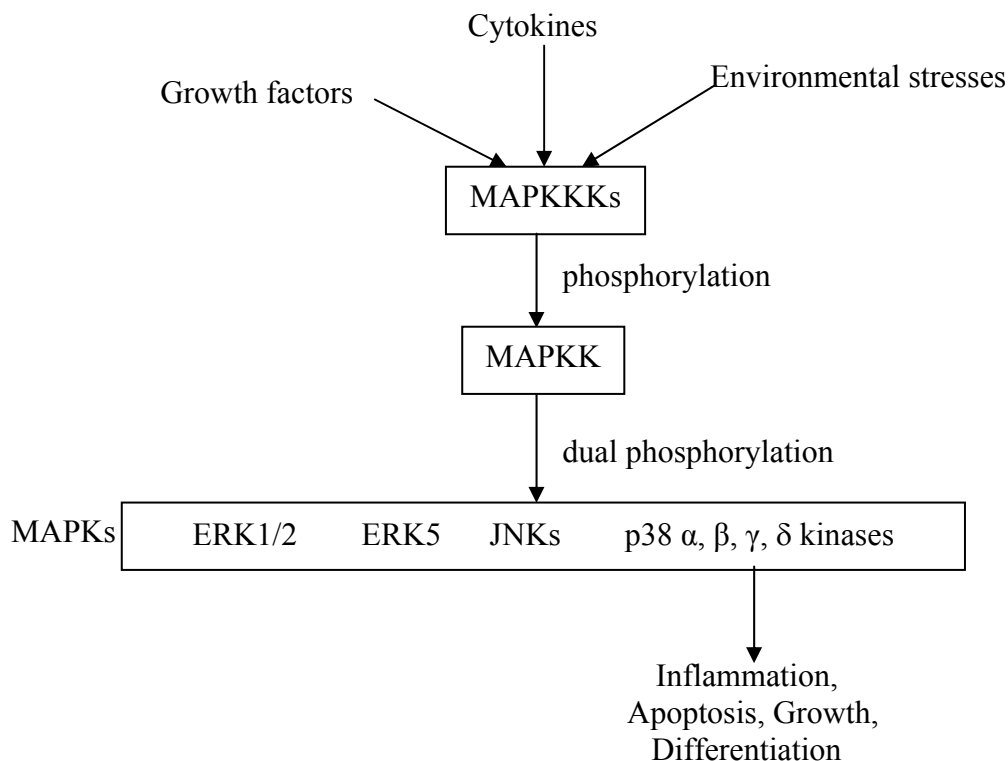


Figure 4-1. Diagram of the MAPK signaling pathway.

The first potent inhibitors developed for p38 kinase belong to the so called imidazole class of inhibitors [76] as represented by the drug SKF 86002, a bicyclic imidazole, [77] and SB 203580, a pyridinyl-imidazole [75] in Fig. 4-2. SB 203580 is a competitive inhibitor of the co-factor ATP binding to p38 MAP kinase [78] and the crystal structure of SB 203580 bound to the N-terminal domain of unphosphorylated p38 MAP kinase provides structural details on the interaction of this inhibitor with p38 MAP kinase [79]. The X-ray crystal structure of p38 α MAP kinase (isoform 2) consists of a deep channel between two structural domains, the C-terminal domain and the N-terminal domain, connected by a linker of amino acid residues His107 to Ala111 [80] and

SB 203580 binds to the ATP co-factor binding site in the N-terminal domain of the kinase [79]. In addition to being a potent inhibitor of p38 MAP kinase, SB 203580 is also reported to possess a high degree of selectivity towards the α and β isoforms of the four known isoforms, α , β , γ , and δ , of p38 kinase as compared to other members of the MAPK family [78,81-84]. These four isoforms are encoded by four different genes and have in common a 12-amino- acid activation loop containing a TGY motif [85]. Furthermore, the α - and β -isoforms are ubiquitously expressed and share 74% identity in amino acid sequence, p38 γ is predominantly expressed in skeletal muscle and is 63% identical to p38 α , while expression of the forth isoform p38 δ has been detected in the lung, kidney, testis, pancreas, and small intestine [86,87,88].

Isothermal titration calorimetry measurements performed on the binding of SB 203580 to the α isoform of p38 MAP kinase at 30°C exhibited a high affinity binding of $K_b = 6.7 \times 10^7 \text{ M}^{-1}$ and exothermic binding with a binding enthalpy of -50 kJ mol^{-1} [78]. Furthermore, the ITC experiments were extended to demonstrate that SB 203580 binds to the ATP-binding pocket of p38 MAP kinase since blocking the ATP-binding site with an analog of ATP prevented binding of this inhibitor [78]. In addition, the binding affinities of SB 203580 and SKF 86002 were compared through a competitive binding assay to p38 MAP kinase using a radioactively labeled inhibitor, SB 202190 [89]. Since SKF 86002 and SB 203580 also inhibit the production of proinflammatory cytokines IL-1 and TNF- α , they are referred to as CSAIDs or cytokine suppressive anti-inflammatory drugs [89]. Another class of kinase inhibitors is the dihydroquinazolinone-based drugs represented by p38 INHIBITOR 1 (p38 INH.1) also shown in Fig. 4-2. The inhibition of p38 MAP kinase by p38 INH.1 was demonstrated by enzyme inhibition studies with radio labeled

ATP and IC_{50} values for these inhibitors were determined [90]. The crystal structure of p38 INH.1 bound to p38 MAP kinase in these mutagenesis studies reveals more extensive interactions with the linkage region and with an additional hydrophobic area in the N-terminal domain [90]. It was shown from mutagenesis studies that the selectivity of quinazolinones and pyridol-pyrimidines for the p38 MAP kinases results from the presence of Gly110 [90]. Although the p38 MAP kinase is active when it is dually phosphorylated, in particular at residues Thr180 and Tyr182 in the so called phosphorylation or activation lip of the protein [80], all of the resolved structures of the p38 α MAP kinase alone [80,91] and the p38 MAP kinases complexed with different classes of inhibitors [79,89,92] are obtained only for the apo or unphosphorylated forms of the protein.

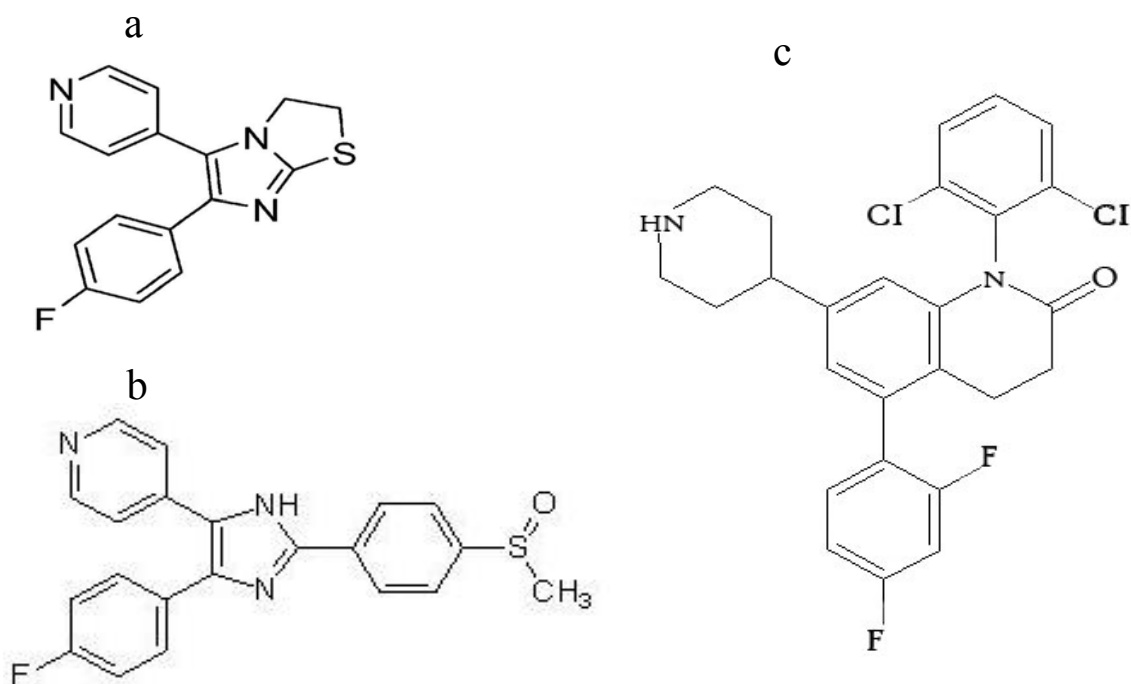
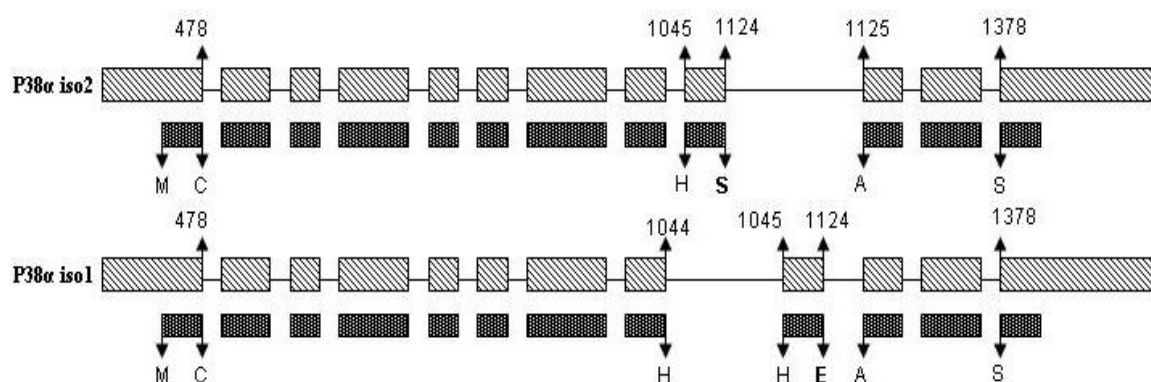


Figure 4-2. Chemical structures of used inhibitors: (a) SKF 86002; (b) SB 203580; (c) p38 INH.1.

In addition, to the use of ITC measurements and enzyme inhibition studies, UV melting, fluorescence exchange, and SPR have been employed to determine the relative binding affinities of inhibitors to the p38 MAP kinases. In particular, Kroe et al. [93] observed good agreement of the binding constants of ten diaryl urea class of inhibitors determined by a UV melting method, a fluorescence exchange method, and by ITC. The UV melting method was based on the increase in the transition temperature of a protein upon inhibitor binding and, thus, employed UV absorption melting scans to determine these temperature increases [93]. In addition, Davidson et al. [94] also employed UV



melting, and ITC as well as surface plasma resonance, fluorescence enhancement, and deuterium exchange mass spectrometry to determine the binding affinity of a diaryl urea inhibitor, CMPD1, to p38 MAP kinase.

The present investigation focuses on the thermodynamics of drug-inhibitor binding to two of the unphosphorylated splice variants of only the α isoform of this protein, p38 α MAP kinase. p38 α MAP kinase has four known splice variants, p38 α isoform 1, p38 α isoform 2, p38 α isoform 3, and p38 α isoform 4. Isoforms 1 and 2 of p38 α MAP kinase for which the gene sequences are shown in Fig. 4-3 are the same length, 360 amino acids and, more interestingly, are the result of an unusual splicing event involving a choice between two adjacent exons [75]. More specifically, the main isoform, isoform 2, has the exon spliced out of isoform 1 and vice versa, isoform 1 contains the adjacent exon that is spliced out from the main isoform. Both spliced-out exons are the same length; the proteins encoded by the two splice variants are also the same size; and the resulting sequence changes in the amino acid residues from 230 to 254 occur in the C-terminal domain of the kinase.



Isoform 2 1-229 DQLKLILRLVGTPGAELLKKISSES 255-360

Isoform 1 1-229 NQLQQIMRLTGTPPAYLINRMPSHE 255-360

Figure 4-3. Schematic exon alignment of splice variants of p38α MAP kinase. The first cDNA sequence  and protein sequence  represents isoform 2 and the second cDNA and protein sequence represents isoform 1. The splice variation occurs after exon 8 schematic in the figure. The resulting different amino acid sequences between I229 and A255 of the two isoforms are shown below.

p38 α isoform 3 contains a different segment within the coding region and a distinct C-terminus as compared to isoform 1 and encodes a shorter protein, 297 amino acids in length. In addition, p38 α isoform 4 also contains a different and shorter internal segment within the coding region as compared to isoform 1 and also encodes a shorter protein, 307 amino acids in length [95].

Isothermal titration calorimetry (ITC) was employed to determine the binding enthalpy ($\Delta_b H^\circ$), the stoichiometry (n), and the binding constant (K_b) of drug binding to isoforms 1 and 2 as a function of temperature. Differential scanning calorimetry (DSC) was employed to determine the effect of inhibitor binding on the conformational stabilities of the p38 α isoforms. The effect of the mutation C162S on the thermodynamics of drug-inhibitor binding to the two isoforms was also investigated in the present study. Since this mutation only occurs on the surface of the protein and this mutant has been expressed at higher levels than that of the wild type, it has been used in X-ray crystallization studies of isoform 2 [96]. The alignment of the X-ray crystal structures for wild type isoform 2 and its C162S mutant is displayed on Fig. 4-4. The crystal structures align pretty well with each other suggesting that there is no effect of the surface C162S mutation on the structure of isoform 2. However, the results presented below suggest that although the mutation is on the surface of the protein and distal from the inhibitor binding site it does have a significant effect on the conformational stability of the proteins upon binding of the drug-inhibitors, SB 203580, SKF 86002, and p38 INH.1.

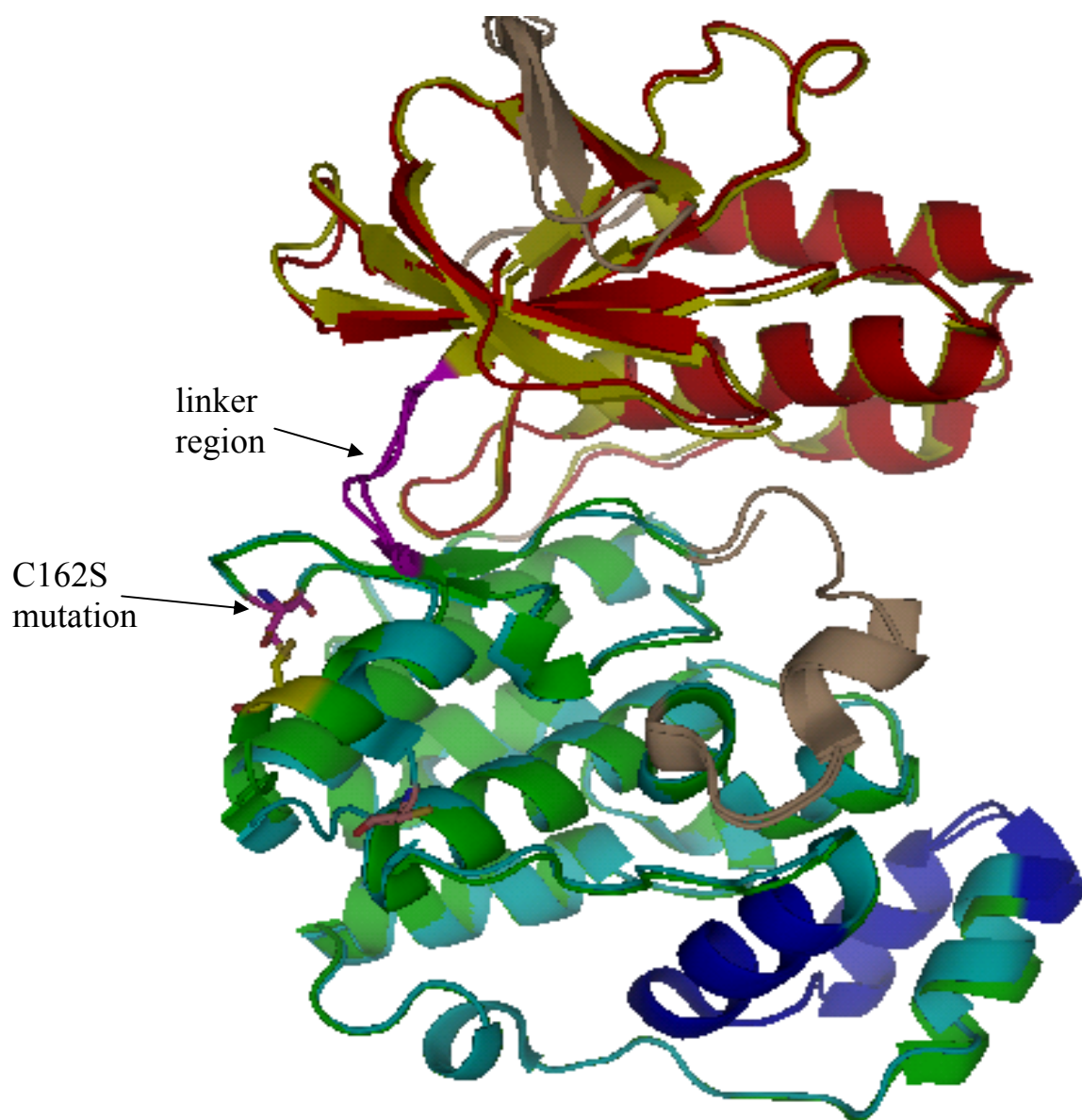


Figure 4-4. Aligned X-ray crystal structures for wild type (wt) and mutant C162S p38α MAP kinase main isoform. The N-terminal domain for the wt and mutant protein is colored in red and yellow, respectively. The C-terminal domain for the wt and mutant protein is in green and cyan color, respectively. The linker region (His107-Ala111), which comprises part of the ATP-binding domain, is in magenta color. The site of the C162S mutation is proximal to the linker region. The 25-amino acid region of difference between the p38α MAP kinase splice variants is in blue color.

4.3 Material and Methods

4.3.1 Protein cloning, expression, and purification

The protocol described below was provided from Victoria Doseeva and Jayanthi Ramprakash.

A cDNA clone containing human mitogen-activated protein kinase 14 (MAPK14 or p38 α) alternatively spliced isoform 1 was purchased from Origene. This clone was used to generate an expression construct, isoform 1 in Pet 15b vector (Novagen). This expression construct was verified by DNA sequencing and has His-tag at the N- terminal. *Escherichia coli* Rosetta (DE3) cells (Novagen) were used for protein expression. An overnight LB culture was used to inoculate three liters of LB media containing 100 $\mu\text{g mL}^{-1}$ ampicillin. Cells were grown at 30°C until OD₆₀₀ reached 0.4, then the temperature was lowered to 20°C and protein expression was induced with 1mM IPTG at mid-log phase. Cells were harvested after overnight expression at 20°C by centrifugation and resuspended in lysis buffer (50 mM Tris, pH 7.5, 500 mM NaCl, 5 mM MgCl₂, 5 mM imidazole, 10 v/v % glycerol, 2 mM TCEP, protease inhibitors and benzonase) (the designation M is used in substitution of moles per liter for concentration) and frozen at -80°C. Cell suspension was sonicated for 3 min. on ice and the lysate was centrifuged at 40,000 rpm for 30 min at 4°C to pellet the cell debris. The supernatant was then added to 10 mL of Ni-NTA resin which had previously been equilibrated in lysis buffer. This matrix was mixed gently in 50 mL tubes at 4°C for 2 hours. The matrix was then transferred to a 10 mL polypropylene column and washed with 200 mL of wash buffer, containing 50 mM Tris, pH 7.5, 500 mM NaCl, 15 mM imidazole, 10 v/v % glycerol. The protein was eluted with buffer containing 50 mM Tris, pH 7.5, 500 mM NaCl, 500

mM imidazole, 10 v/v % glycerol. Eluted fractions were analyzed by SDS-PAGE and confirmed by Western blot analysis using p38 α MAP Kinase Antibodies (Cell Signaling Technology).

Peak fractions were combined based on SDS-PAGE results and dialyzed against three changes of 2 L dialysis buffer, containing 25 mM Tris, pH 7.5, 10 mM NaCl. The His tag was cleaved by thrombin digestion of the protein (10 μ L of thrombin solution (10 cleavage units) per mg fusion protein) and thrombin was removed with pAminoBenzamidine-Agarose. His tag cleaved protein was passed through second Nickel column and concentrated using Centriprep filter units YM-10 (Millipore). Concentrated protein was further purified by Gel filtration using HiPrep 26/60 Sephacryl S-200 HR column. This column was equilibrated with the buffer, 20 mM Tris (pH 7.5), 100 mM NaCl, 5 v/v % glycerol, 10 mM DTT. No more than 5 mL of concentrated p38 α protein was applied to 320 mL Sephacryl S200 column at 2 mL min⁻¹ and eluted peak fractions were pooled and concentrated to 10-15 mg mL⁻¹. The total protein concentration was determined by Bio-Rad protein assay reagent. A single intense band was observed at 42,000 g mol⁻¹, the molecular mass level of p38 α MAP kinase, by SDS-PAGE. Because of the absence of bands at 5% of the intensity of this band, it was estimated that the p38 α MAP kinase was greater than 95 mol% in purity. The C162S mutants of isoforms 1 and 2 were generated using QuikChange Site-Directed Mutagenesis Kit (Stratagene) by following standard protocol and the mutation was verified by DNA sequencing. Mutants of isoforms 1 and 2 proteins were prepared employing the same protocol.

The protein solutions were dialyzed prior to the ITC measurements in a buffer consisting of 5 mM HEPES, 150 mM NaCl, 20 mM MgCl₂, and 2 v/v% DMSO at pH 7.4.

The concentrations of the proteins were determined by UV absorption measurements at 280 nm using an extinction coefficient of $49,850 \text{ M}^{-1}\text{cm}^{-1}$ [78]. Since the SB 203580 is completely soluble in DMSO and in the buffer solutions [78], the SB 203580 was dissolved in 100 v/v% DMSO by weight and aliquots of the DMSO solution were added to make up the 2 v/v% DMSO component of the buffer solution. Solutions of the SKF 86002 and p38 INH.1 inhibitors were also made up by diluting their 100 v/v% DMSO solutions with the aqueous buffer to make up the 2 v/v% DMSO buffer solutions. Since it was uncertain as to whether the SKF 86002 and p38 INH.1 were completely soluble in the 2 v/v% DMSO buffer solution, the concentrations of these inhibitors in the 2 v/v% buffer solutions were re-determined from optical density measurements. The extinction coefficients of p38 INH.1 and SKF 86002 were determined by completely dissolving known masses of the drug in several solvents including DMSO and measuring their UV absorption spectra over a range of concentrations. The experimentally determined extinction coefficients were $8,130 \text{ M}^{-1}\text{cm}^{-1}$ at 300 nm and $7,443 \text{ M}^{-1}\text{cm}^{-1}$ at 340 nm for p38 INH.1. For SKF 86002, the experimentally determined extinction coefficients were $9,268 \text{ M}^{-1}\text{cm}^{-1}$ at 326 nm and $8,894 \text{ M}^{-1}\text{cm}^{-1}$ at 320 nm.

4.3.2 Isothermal titration calorimetry

For all the ITC measurements, the solution vessel of a VP Microcal, Inc. isothermal titration calorimeter was filled up with 1.43 mL of the appropriate protein solution at concentrations approximately $10 \times$ to $20 \times$ lower than the drug-inhibitor concentrations in the stirrer syringe. Prior to loading into the ITC vessel, the protein solution was dialyzed against the dialysis buffer consisting of 5 mM HEPES, 150 mM

NaCl, 20 mM MgCl₂, and 2 v/v % DMSO at pH 7.4. The dialysis buffer was in the reference vessel of the ITC, and used for rinsing of the vessels during the experiment. The inhibitor solution was first titrated into the dialysate to determine any heats of dilution of the inhibitor solution. Then the solution vessel in the ITC was rinsed thoroughly several times with the buffer and filled with the protein solution. Five to ten microliters aliquots of the inhibitor solution were added to the protein solution until well past saturation of the protein binding sites as evident by the appearance of titration peaks of the same amplitude as those of the dilution titration peaks. The analysis of the titration of the drug-inhibitor solution into the protein solution consisted of first subtracting an average heat of dilution of the inhibitor solution from the binding isotherm and then fitting the resulting binding isotherm to a single site binding model equation to determine values for n , $\Delta_b H^\circ$, and K_b as described previously [28]. The fitting procedure was performed by the software program Origin from Microcal, Inc. Values of the binding free energy change ($\Delta_b G^\circ$) and the binding entropy ($\Delta_b S^\circ$) were then determined from the fundamental equation of thermodynamics:

$$\Delta_b G^\circ = -RT \ln \{ K_b \} = \Delta_b H^\circ - T \Delta_b S^\circ \quad (4.1)$$

The heat capacity change for the binding reaction, $\Delta_b C_p$, was determined as the slope of the assumed linear dependence of the binding enthalpy on temperature. Uncertainties in n , K_b , and $\Delta_b H^\circ$ for each ITC scan were generated from the final iterative fit of the single site binding model to the ITC isotherm data. Each ITC reaction was performed at least twice and the uncertainties in the values of n , K_b , and $\Delta_b H^\circ$ of each ITC scan were employed as weighing factors in determining average values for n , K_b , and $\Delta_b H^\circ$ from the

ITC reactions. The uncertainties are, thus, reported as standard deviations of the averaged n , K_b , and $\Delta_b H$ values.

4.3.3 Displacement isothermal titration calorimetry

The direct ITC measurements described previously with the inhibitor, p38 INH.1 revealed that the binding of the inhibitor to p38 α protein is very tight, exceeding the ITC limit on reliably determining binding constants up to 10^8 M^{-1} . Therefore, ITC displacement measurements as described previously [97] were performed with this inhibitor. Briefly, a weaker affinity inhibitor such as SKF 86002 was first titrated into the protein solution following the ITC procedure just described, then the syringe was emptied, cleaned, filled with the p38 INH.1 solution, and the p38 INH.1 solution was titrated into the weak inhibitor (SKF 86002) -protein complex solution to displace the weaker binding inhibitor. Because of the displacement reaction, the second titration results in an apparent lower binding constant amenable to analysis by Origin. A heat of dilution of the p38 INH.1 solution into just the dialysate was determined in a separate ITC experiment. The titration results were analyzed by employing the competitive binding model from Origin 7.0 [98] to yield binding constants for p38 INH.1. The criterion from Origin 7.0 of " K_A "/ $K_B[B]_{\text{tot}} = 10^5 - 10^8 \text{ M}^{-1}$ where " K_A " is an estimate of the p38 INH.1 binding constant, K_B is the SKF 86002 binding constant, and $[B]_{\text{tot}}$ is the total average concentration of SKF 86002 was followed for the second displacement titration. The Origin 7.0 fitting procedure required an average value for the SKF 86002 concentration and an initial value for the p38 INH.1 binding enthalpy, which was determined from a separate direct titration of p38 INH.1 solution into the protein

solution. The average value of the SKF 86002 concentration was determined as the average of the initial SKF 86002 concentration from the number of injections and volume of each injection in the first titration and of the final SKF 86002 concentration determined from dilution of the initial concentration by the total number and volume of injections in the second titration. Each displacement titration was performed twice and, thus, the uncertainties are reported as standard deviations between the averaged n , K_b , and $\Delta_b H^\circ$ values.

4.3.4 Differential scanning calorimetry

DSC measurements were performed using a VP DSC from Microcal Inc. (Northampton, MA). DSC measurements were performed on the protein-inhibitor complexes from the ITC titrations. DSC measurements on the protein solutions alone were performed in two different buffers: the ITC buffer consisting of 5 mM HEPES, 150 mM NaCl, 20 mM MgCl₂, and the storage buffer consisting of 25 mM Tris HCl, pH 8.0, 100 mM NaCl, 5 v/v % glycerol, and 10 mM DTT. The volumes of the solution and the reference vessels were 0.511 mL and the scan rate was either 15 or 60°C hr⁻¹. A series of DSC scans consisted of two buffer versus buffer scans from 15 to 95°C followed by several repeat scans of the protein or protein complex solutions under the same conditions of temperature range and scan rate. Either the second buffer versus buffer scan was employed in the analysis as the baseline scan or a repeat scan of the protein/complex solution versus buffer scan for a non-repeatable transition was used as the baseline scan. After subtraction of the baseline scan from the protein or complex solution scan, the resulting difference power versus temperature data scans were divided by the scan rate to

convert the power versus temperature scan into a heat capacity versus temperature data scan. Utilizing the EXAM program [99], a two-state $A \rightleftharpoons B$ transition model was then fitted to the heat capacity versus temperature data scan to determine the van't Hoff enthalpy ($\Delta_{\text{trs}}H_{\text{vH}}$) for the scan from the shape of the transition peak, a transition temperature (T_G), the temperature at the area mid-point of the transition, and a calorimetric transition enthalpy ($\Delta_{\text{trs}}H$) from the area of the transition peak and the amount of protein in the solution vessel of the DSC. The ratio, $\Delta_{\text{trs}}H / \Delta_{\text{trs}}H_{\text{vH}}$, is termed the transition cooperativity which normally is 1.0 for the unfolding transition of a simple monomeric protein. The uncertainties in $\Delta_{\text{trs}}H_{\text{vH}}$, T_G , and $\Delta_{\text{trs}}H$ were determined as the standard deviation of their values averaged from several DSC scans with the same samples.

The binding constants determined from the ITC measurements were extrapolated up to the denaturation temperature of the complex and employed to estimate the increase in the denaturation temperature of the protein in its complexed state provided that the inhibitor does not bind to the unfolded state [100]. The equations utilized for the above calculations are as follows:

For extrapolation of the ITC determined binding constants up to the denaturation temperature of the complex, $T_G(I)$,

$$\ln[K_b(T_G(I))/K(T_o)] = [(-\Delta_bH(T_o) + \Delta_bCpT_o)/R]*(1/T_G(I) - 1/T_o) + (\Delta_bCp/R)*\ln(T_G(I)/T_o) \quad (4.2)$$

and for estimates of the temperature shifts at the denaturation temperature,

$$1/T_G - 1/T_G(I) = (R/\Delta_{\text{trs}}H) \ln\{1.00 + ([I_o]-[P_o]/2) K_b(T_G(I))\} \quad (4.3)$$

where T_o is the temperature of ITC determinations of K_b , T_G is the denaturation temperature of the protein alone, $T_G(I)$ is the transition temperature of the complex, $\Delta_{\text{trs}}H$ is the transition enthalpy of the complex, $[I_o]$ is the total initial inhibitor concentration, and $[P_o]$ is the total initial protein concentration.

4.4 Results

A typical ITC scan of the inhibitor SB 203580 binding to isoform 1 at 30°C along with its binding isotherm is shown in Fig. 4-5.

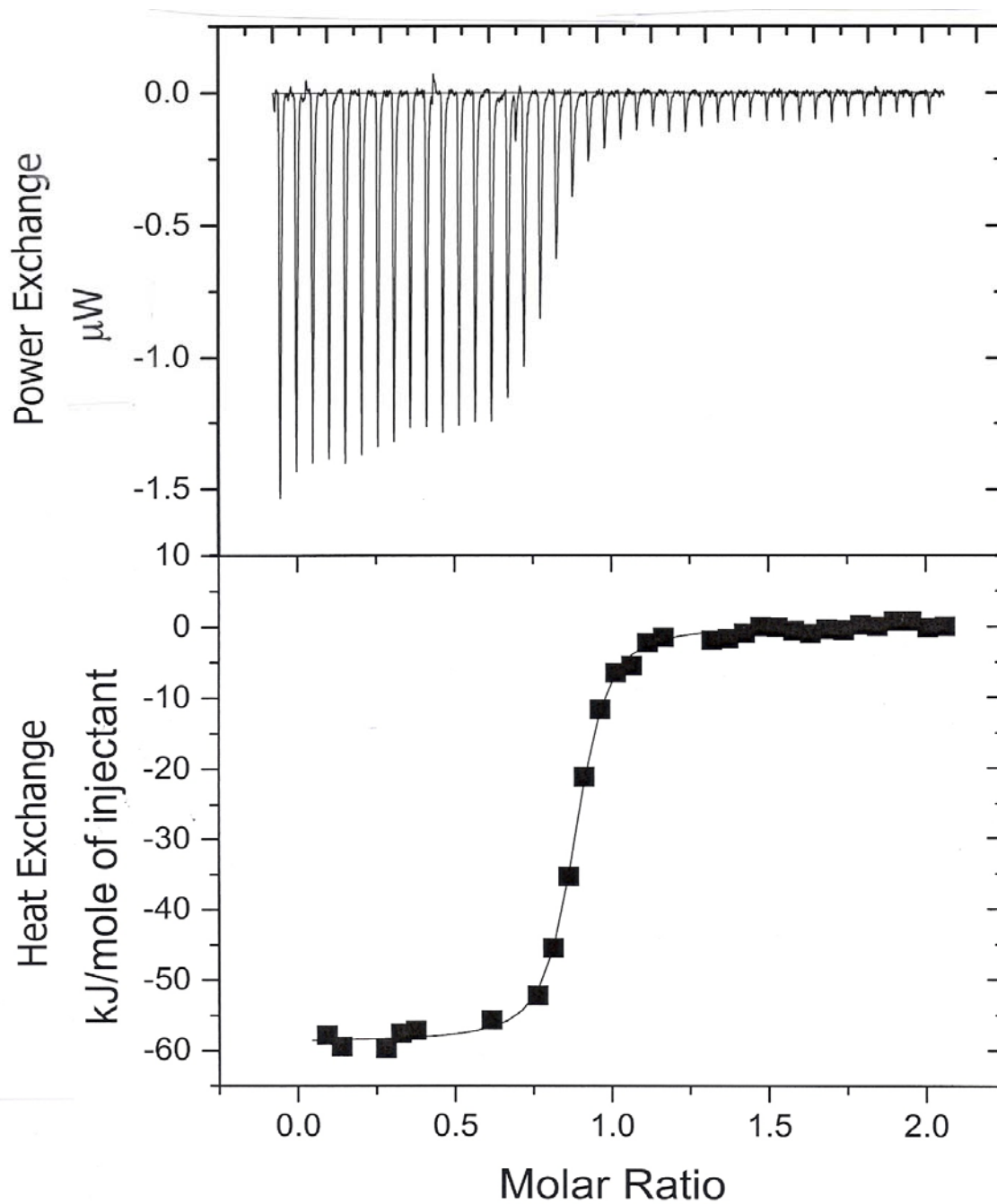


Figure 4-5. An ITC scan of 6 μL injections of a 0.1 mM SB 203580 solution into a 9.26 μM solution of isoform 1 at 30°C (top panel) and fit of a 1:1 binding model to the binding isotherm of this scan (bottom panel).

Typical ITC scans of the inhibitors SKF 86002 and SB 203580 binding to isoform 1 C162S, along with their binding isotherms are shown, respectively, in Figs. 4-6 and 4-7. Most of the SKF 86002 and SB 203580 binding reactions were performed at 25.0, 30.0, and 35.0°C, and the thermodynamic binding parameters determined at these temperatures are summarized in Tables 4-1 and 4-2. The stoichiometries of the binding reactions average 0.87 for isoform 1, 0.73 for isoform 1 C162S, 0.93 for isoform 2, and 0.62 for isoform 2 C162S in Tables 4-1 and 4-2. It should be emphasized that the protein concentrations were determined from UV optical density measurements, which does not distinguish between the optical densities of both inactive and active binding protein, while the ITC stoichiometries are determined for only the active binding protein and, thus, may be lower. The binding reactions are all exothermic and are totally enthalpically-driven. The SB 203580 binding thermodynamic parameters to isoform 2 of $K_b = 5.3 \pm 0.9 \times 10^7 \text{ M}^{-1}$ and $\Delta_b H^\circ = -59 \pm 8 \text{ kJ mol}^{-1}$ at 30.0°C are close to the literature values [93] of $K_b = 6.67 \times 10^7 \text{ M}^{-1}$ and $\Delta_b H^\circ = -50.2 \text{ kJ mol}^{-1}$ at 30.0°C. For the weaker binding drug-inhibitors, SKF 86002 and SB 203580, the binding constants at 25°C range from $1.2 \pm 0.2 \times 10^7 \text{ M}^{-1}$ for SKF 86002 binding to isoform 1 C162S to $11.1 \pm 1.8 \times 10^7 \text{ M}^{-1}$ for SB 203580 binding to isoform 2 C162S, almost an order of magnitude in range, while the binding enthalpies are similar, respectively, -54 ± 3 and $-50.0 \pm 0.2 \text{ kJ mol}^{-1}$. The binding constants of the weakest binding inhibitor SKF 86002 to isoform 1 C162S, isoform 2, and isoform 2 C162S are almost within experimental error at 25°C and to the two C162S mutants are almost within experimental error at 30 and 35°C in Tables 4-1 and 4-2. The higher binding constants of the drug-inhibitor, SB 203580, exhibit more of a

variation at 25°C, ranging from $2.8 \pm 0.6 \times 10^7 \text{ M}^{-1}$ for binding to isoform 1 C162S to $11.1 \pm 1.8 \times 10^7 \text{ M}^{-1}$ for binding to isoform 2 C162S.

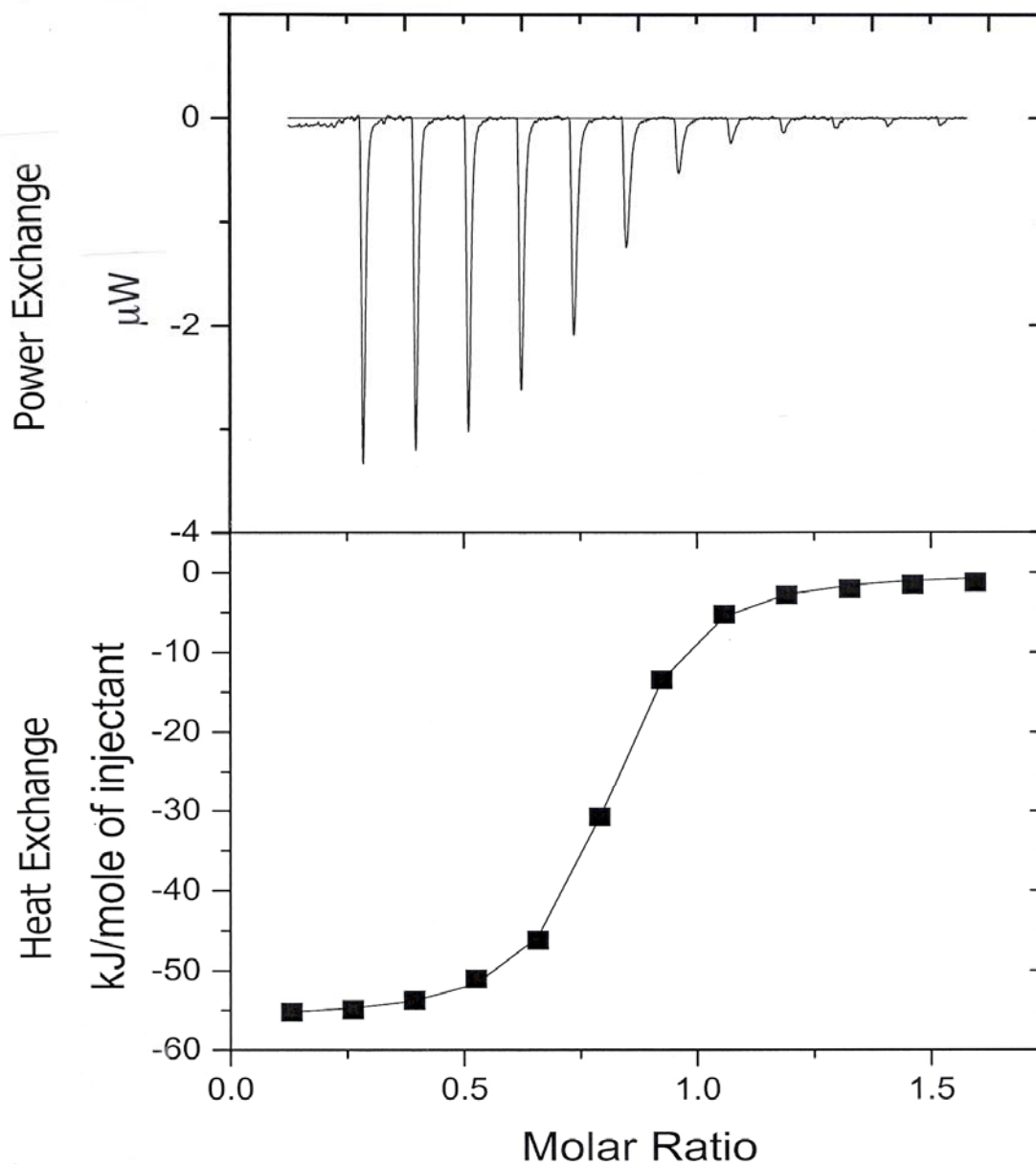


Figure 4-6. An ITC scan of 4 μL injections of a 0.399 mM SKF 86002 solution into a 8.71 μM solution of isoform 1 C162S at 25°C (top panel) and fit of a 1:1 binding model to the binding isotherm of this scan (bottom panel).

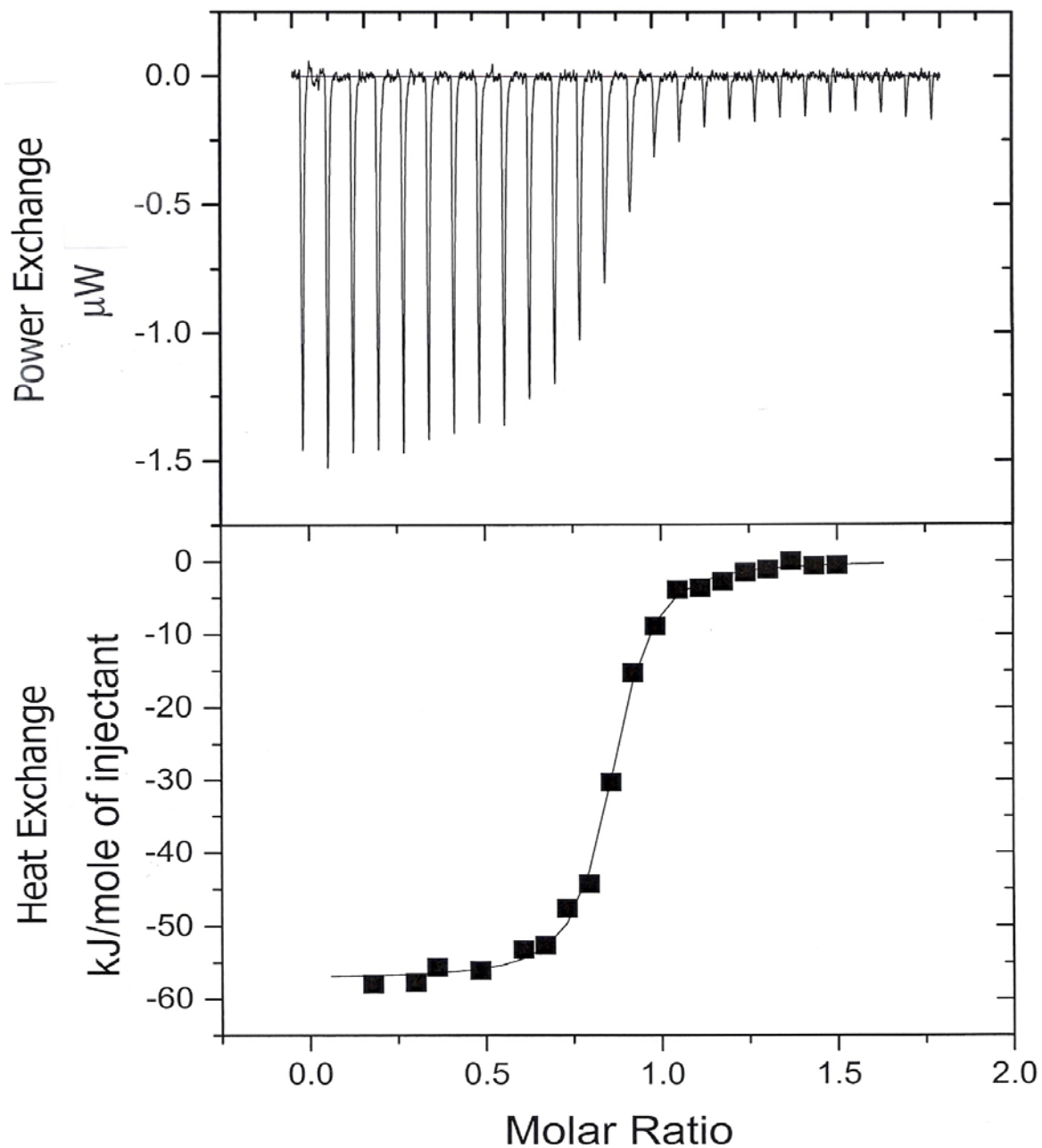


Figure 4-7. An ITC scan of 6 μL injections of a 0.1 mM SB 203580 solution into a 9.26 μM solution of isoform 1 C162S at 30°C (top panel) and fit of a 1:1 binding model to the binding isotherm of this scan (bottom panel).

Table 4-1. Thermodynamics of SB 203580 and SKF 86002 binding to isoform 1 and isoform 1 C162S in 5 mM HEPES buffer at pH 7.4 ± 0.1 from ITC measurements.

Drug-inhibitor	T °C	n	K_b 10^7 M^{-1}	$-\Delta_b G^\circ$ kJ mol ⁻¹	$-\Delta_b H^\circ$ kJ mol ⁻¹	$-\Delta_b S^\circ$ J mol ⁻¹ K ⁻¹
<i>Isoform 1</i>						
SB 203580	25.0 ± 0.1	0.88 ± 0.01	7.8 ± 0.8	45.0 ± 0.3	49.8 ± 0.3	16.1 ± 0.04
SB 203580	30.0 ± 0.1	0.86 ± 0.01	3.7 ± 0.3	43.9 ± 0.2	58.7 ± 0.3	48.8 ± 0.4
$\Delta_b C_p = -1.78 \pm 0.01 \text{ kJ mol}^{-1} \text{ K}^{-1}$						
<i>Isoform 1 C162S</i>						
SKF 86002	25.0 ± 0.1	0.77 ± 0.02	1.2 ± 0.2	40.4 ± 0.4	54 ± 3	45.6 ± 3.0
SKF 86002	30.0 ± 0.1	0.71 ± 0.01	0.83 ± 0.10	40.1 ± 0.3	61 ± 1	69.0 ± 1.2
SKF 86002	35.0 ± 0.1	0.64 ± 0.09	0.50 ± 0.18	39.5 ± 0.9	67 ± 1	89.2 ± 1
$\Delta_b C_p = -1.30 \pm 0.06 \text{ kJ mol}^{-1} \text{ K}^{-1}$						
SB 203580	25.0 ± 0.1	0.79 ± 0.01	2.8 ± 0.6	42.5 ± 0.12	58 ± 1	52.0 ± 1.1
SB 203580	30.0 ± 0.1	0.75 ± 0.12	4.5 ± 2.6	44.4 ± 1.5	58 ± 1	44.9 ± 1.8
SB 203580	35.0 ± 0.1	0.71 ± 0.01	5.8 ± 0.6	45.8 ± 0.3	64 ± 1	59.1 ± 1.0
$\Delta_b C_p = -0.63 \pm 0.37 \text{ kJ mol}^{-1} \text{ K}^{-1}$						

The uncertainties are standard deviations of the mean values.

Table 4-2. Thermodynamics of SB 203580 and SKF 86002 binding to isoform 2 and isoform 2 C162S in 5 mM HEPES buffer at pH 7.4 ± 0.1 from ITC measurements.

Drug-inhibitor	T °C	n	K_b 10^7 M^{-1}	$-\Delta_b G^\circ$ kJ mol ⁻¹	$-\Delta_b H^\circ$ kJ mol ⁻¹	$-\Delta_b S^\circ$ J mol ⁻¹ K ⁻¹
<i>Isoform 2</i>						
SKF 86002	25.0 ± 0.1	0.76 ± 0.01	1.30 ± 0.03	40.6 ± 0.1	55.6 ± 0.6	50.3 ± 0.6
SKF 86002	30.0 ± 0.1	1.17 ± 0.01	0.50 ± 0.03	38.9 ± 0.2	39.0 ± 0.2	0
SKF 86002	35.0 ± 0.1	1.06 ± 0.21	0.44 ± 0.02	39.2 ± 0.1	44.3 ± 9.3	16.6 ± 9.3
$\Delta_b C_p = 2.2 \pm 1.2 \text{ kJ mol}^{-1} \text{ K}^{-1}$						
SB 203580	30.0 ± 0.1	0.72 ± 0.05	5.3 ± 0.9	44.8 ± 0	59 ± 8	48 ± 8
<i>Isoform 2 C162S</i>						
SKF 86002	25.0 ± 0.1	0.68 ± 0.02	1.42 ± 0.47	40.8 ± 0.8	51.7 ± 1.5	36.6 ± 1.7
SKF 86002	30.0 ± 0.1	0.61 ± 0.01	0.89 ± 0.11	40.3 ± 0.3	52.6 ± 0.9	40.6 ± 0.9
SKF 86002	35.0 ± 0.1	0.56 ± 0.03	0.64 ± 0.13	40.2 ± 0.5	63.7 ± 3.6	76.3 ± 3.6
$\Delta_b C_p = -1.20 \pm 0.59 \text{ kJ mol}^{-1} \text{ K}^{-1}$						
SB 203580	25.0 ± 0.1	0.67 ± 0.02	11.1 ± 1.8	45.9 ± 0.4	50.0 ± 0.2	13.8 ± 0.4
SB 203580	30.0 ± 0.1	0.62 ± 0.07	5.4 ± 2.0	44.9 ± 0.9	60.5 ± 0.5	51.5 ± 1.0
SB 203580	35.0 ± 0.1	0.53 ± 0.01	4.9 ± 0.5	45.4 ± 0.3	63.0 ± 0.5	57.1 ± 0.6
$\Delta_b C_p = -1.30 \pm 0.46 \text{ kJ mol}^{-1} \text{ K}^{-1}$						

The uncertainties are standard deviations of the mean values.

Since ITC scans of the p38 INH.1 solution inhibitor into solutions of isoform 1 C162S, isoform 2 C162S, and isoform 2 yielded binding constants above the determination limit of 10^8 M^{-1} of the ITC, displacement ITC titrations were performed with this inhibitor by titrating p38 INH.1 solutions into the solutions of the protein already complexed with the SKF 86002 inhibitor. A typical ITC titration of p38 INH.1 into isoform 1 C162S complexed with SKF 86002 is shown in Fig. 4-8. In determining the best fit of the binding model to the ITC binding isotherm, a number of titration points were not used in the fit. The results of fits of the displacement ITC titrations employing the competitive binding model of Origin 7.0 are summarized in Table 4-3.

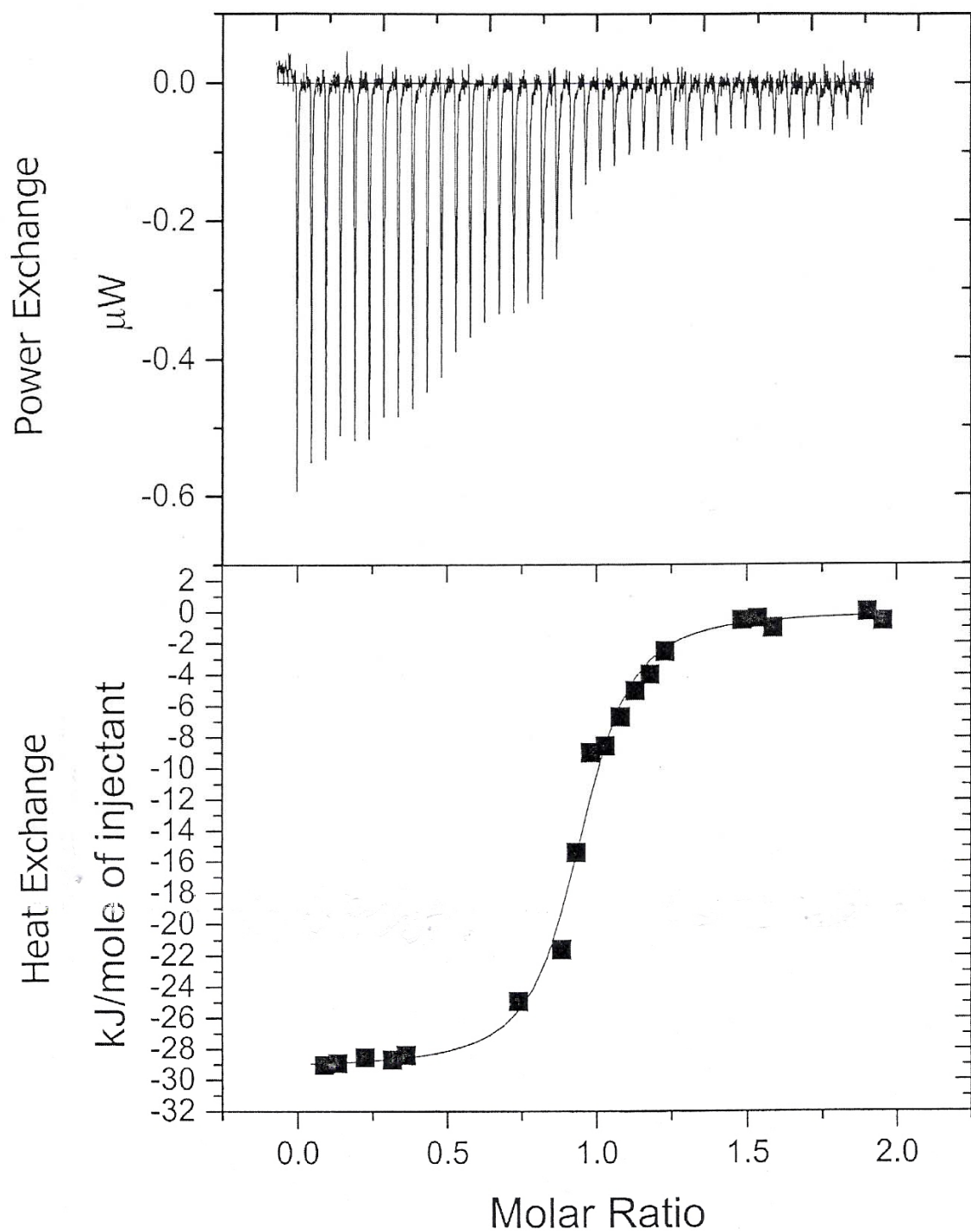


Figure 4-8. An ITC scan of 7 μL injections of a 0.0749 mM p38 INH.1 solution into a 8.42 μM solution of isoform 1 C162S complexed with SKF 86002 at 25°C (top panel) and fit of a 1:1 binding model to the binding isotherm of this scan (bottom panel).

Table 4-3. Thermodynamics of p38 INH.1 binding to the isoforms in 5 mM HEPES buffer at pH 7.4 ± 0.1 from ITC displacement measurements.

T	n	K_b	$-\Delta_b G^\circ$	$-\Delta_b H^\circ$	$-\Delta_b S^\circ$
$^\circ\text{C}$		10^7 M^{-1}	kJ mol^{-1}		$\text{J mol}^{-1} \text{ K}^{-1}$
<i>Isoform 1 C162S + SKF 86002 complex</i>					
25.0 ± 0.1	0.89 ± 0.02	1.93 ± 0.93	53.0 ± 1.2	80.3 ± 1.0	91.4 ± 1.5
35.0 ± 0.1	0.64 ± 0.02	0.57 ± 0.30	51.7 ± 1.3	102.5 ± 2.0	164.9 ± 2.4
$\Delta_b C_p = -2.22 \pm 0.22 \text{ kJ mol}^{-1} \text{ K}^{-1}$					
<i>Isoform 2 + SKF 86002</i>					
25.0 ± 0.1	0.82 ± 0.01	5.30 ± 1.70	55.5 ± 0.8	82.5 ± 0.7	90.5 ± 1.0
35.0 ± 0.1	0.82 ± 0.01	2.20 ± 1.60	55.1 ± 1.9	76.6 ± 1.1	69.8 ± 2.2
$\Delta_b C_p = 0.59 \pm 0.13 \text{ kJ mol}^{-1} \text{ K}^{-1}$					
<i>Isoform 2 C162S + SKF 86002 Complex</i>					
25.0 ± 0.1	0.71 ± 0.01	5.39 ± 1.34	55.5 ± 0.6	81.9 ± 0.5	88.6 ± 0.8
35.0 ± 0.1	0.61 ± 0.02	1.29 ± 0.71	53.7 ± 1.4	97.2 ± 1.8	141.2 ± 2.3
$\Delta_b C_p = -1.53 \pm 0.19 \text{ kJ mol}^{-1} \text{ K}^{-1}$					

The uncertainties are standard deviations of the mean values.

As shown under the DSC results (Table 4-5), the denaturation transition properties of the final product of ITC displacement reactions agree with those of the p38 INH.1-protein complex alone, indicating that the displacement of SKF 86002 by p38 INH.1 had indeed occurred. The p38 INH.1 binding constants are 10^2 times higher than for SKF 86002 and SB 203580 binding to the isoform C162S mutants and to isoform 2. The p38 INH.1 binding reactions are again enthalpically-driven as shown in Table 4-3. There are also substantial decreases in the p38 INH.1 binding entropies relative to the corresponding binding entropies of SKF 86002 and SB 203580 that compensate for the larger negative binding enthalpies for p38 INH.1. Furthermore, the p38 INH.1 binding constants at 25°C range from $1.9 \times 10^9 \text{ M}^{-1}$ for binding to isoform 1 C162S to $5.4 \times 10^9 \text{ M}^{-1}$ for binding to isoform 2 C162S, a range of values lower than the range observed for SB 203580 binding to these isoforms at 25°C. The binding enthalpies are almost a factor of 2 lower for binding of the strong inhibitor (p38 INH.1) than for the weaker binding SKF 86002 and SB 203580 inhibitors.

Changes in the binding heat capacities, $\Delta_b C_p$, were determined from assuming a linear dependence of the binding enthalpy on temperature and are also presented in Tables 4-1, 4-2, and 4-3. The binding heat capacities are negative for drug-inhibitor binding to the C162S mutants and to isoform 1 while, in contrast, for SKF 86002 binding to isoform 2 is positive and zero for p38 INH.1 binding to isoform 2.

Typical DSC scans of isoform 2 and its C162S mutant in the absence of drugs are shown as the low temperature single peaks in Figs. 4-9 and 4-10. The higher temperature transitions are of the proteins bound to SB 203580.

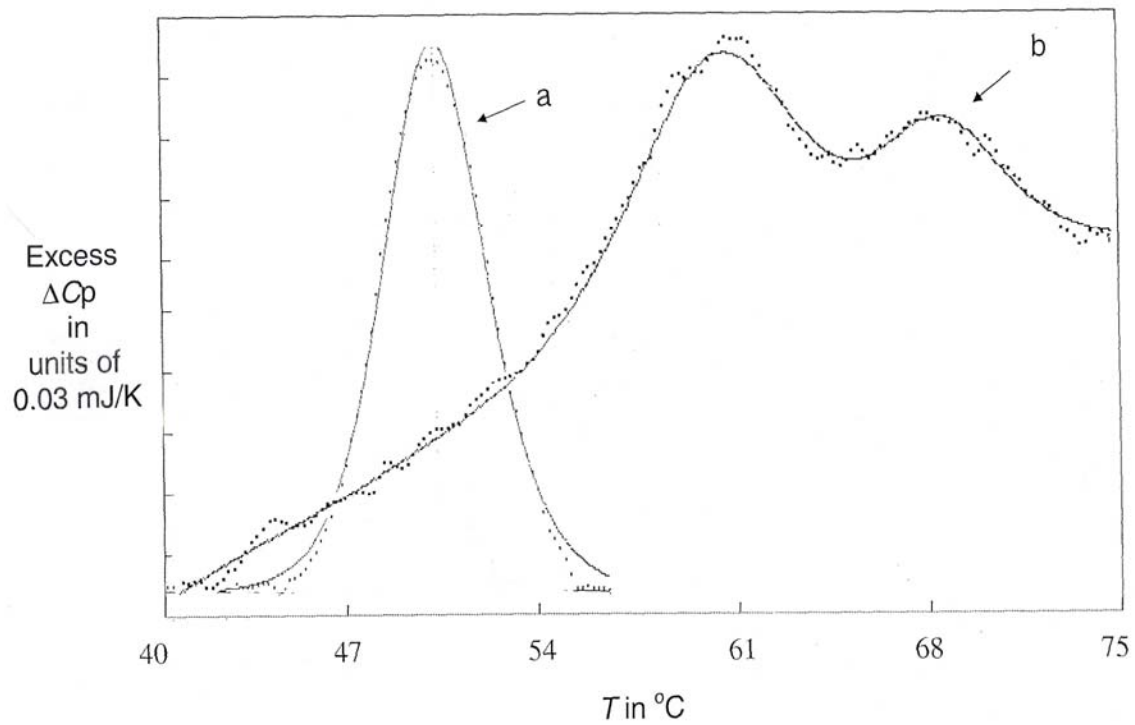


Figure 4-9. DSC scans at $60^{\circ}\text{C hr}^{-1}$ of $2.69 \mu\text{M}$ of isoform 2 (a) and of isoform 2 complexed with SB 203580 (b). The solid lines are the fits of a two-state thermodynamic transition model to the data.

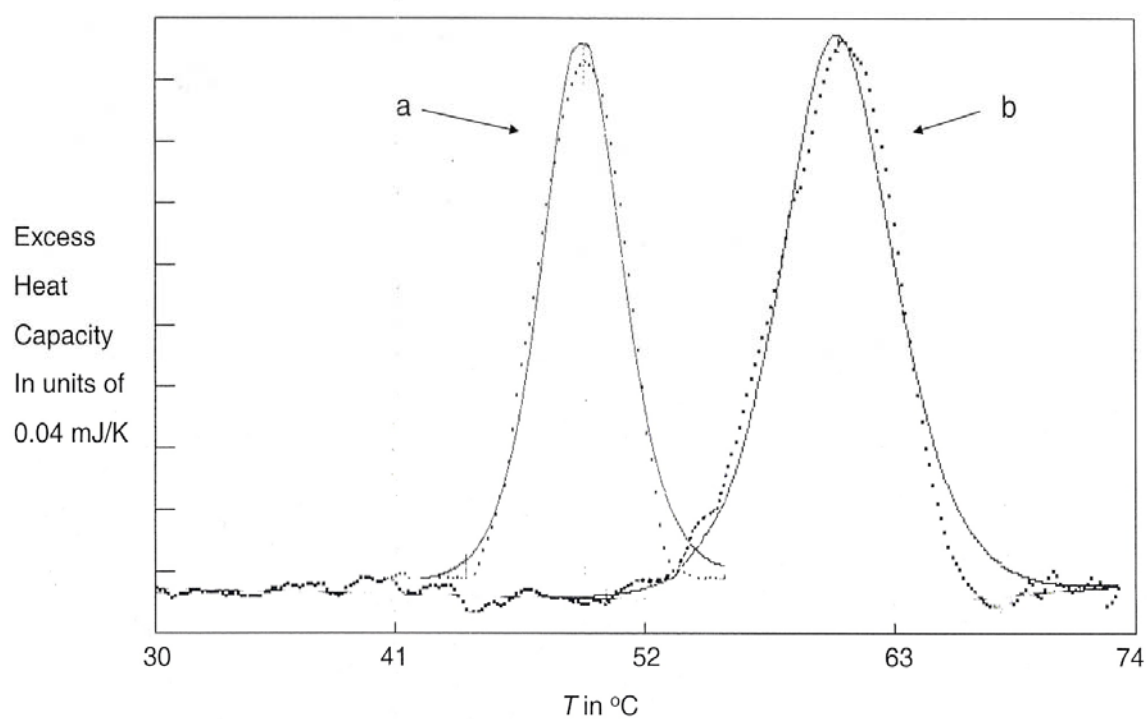


Figure 4-10. DSC scans at $60^{\circ}\text{C hr}^{-1}$ of $4.14\text{ }\mu\text{M}$ of isoform 2 C162S (a) and of $4.40\text{ }\mu\text{M}$ isoform 2 C162S complexed with SB 203580 (b). The solid lines are the fits of a two-state thermodynamic transition model to the data.

All the DSC unfolding transition data were best fitted to a $A \rightleftharpoons B$ thermodynamic transition model from EXAM [99] to yield values for the van't Hoff and calorimetric enthalpies and the transition temperatures for the two isoforms and their C162S mutants alone and with the bound inhibitors as summarized in Tables 4-4 and 4-5. Repeat scans of the protein samples and their inhibitor complexes did not exhibit the transitions that appeared in the initial scans. However, DSC scans at the lower scan rate of $15^{\circ}\text{C hr}^{-1}$ shown for isoform 2 in Table 4-5 and the C162S mutant of isoform 1 in Table 4-4 exhibit the same transition thermodynamic parameters as at the faster scan rate of $60^{\circ}\text{C hr}^{-1}$. Although the transitions do not re-appear during a re-scan of the solutions, Manly et al. [38] have justified analysis of the transitions in terms of a thermodynamic two-state transition model of those proteins that exhibit transition properties independent of scan rate. All the drug-inhibitor concentrations were in excess of the concentrations necessary to saturate the binding sites of the protein. DSC scans for all three proteins alone were performed using the storage buffer. To determine if there is any effect of the buffer composition on the thermodynamic unfolding properties, DSC scans for the C162S mutants were also performed with the HEPES buffer employed in the ITC titrations. As seen in Tables 4-4 and 4-5 the denaturation temperatures and enthalpies obtained with the HEPES buffer are within 2°C as those obtained with the storage buffer. In Tables 4-4 and 4-5, the transition temperature of isoform 2 of $50.0 \pm 0.1^{\circ}\text{C}$ is about 2°C higher than that of isoform 1 while the C162S mutants are lower but the same, $46.5 \pm 0.1^{\circ}\text{C}$ for isoform 1 C162S and $45.5 \pm 0.1^{\circ}\text{C}$ for isoform 2 C162S. The van't Hoff transition enthalpies are high in the range of 652 kJ mol^{-1} to 859 kJ mol^{-1} .

Table 4-4. Thermodynamic transition parameters of isoform 1 and its C162S mutant and in the presence of drug-inhibitors from fits of a two-state transition model to the DSC data.

[Protein] μM	Drug-inhibitor	T_G °C	$T_G(\text{cal.})^b$ °C	$\Delta_{\text{trs}}H_{\text{VH}}$ kJ mol ⁻¹	$\Delta_{\text{trs}}H$	Ratio
<i>Isoform 1</i>						
2.69–3.45 ^a		48.2 ± 0.1		652 ± 31	1081 ± 175	1.7 ± 0.4
7.88–11.5	SB 203580	54.3 ± 0.1	53.9	594 ± 46	548 ± 77	
	2 nd transition	59.0 ± 0.1	53.1	772 ± 106		
<i>Isoform 1 C162S</i>						
2.76–11.2 ^a		46.5 ± 0.1		760 ± 28	275 ± 6	0.36 ± 0.02
[4.14]		[44.0 ± 0.5]		[744 ± 5]	[318 ± 19]	[0.43 ± 0.03]
2.48		46.9 ± 0.1		851 ± 49	160 ± 34	0.19 ± 0.01
5.95–10.5	SKF 86002	52.4 ± 0.1	54.2	461 ± 35	407 ± 111	0.91 ± 0.25
3.10–6.50	SB 203580	55.4 ± 0.1	53.4	477 ± 40	610 ± 141	1.36 ± 0.42
3.53–3.82	p38 INH.1	61.4 ± 0.1	61.8	622 ± 30	267 ± 39	0.46 ± 0.10

Values in [] were determined from slower DSC scans at 15°C hr⁻¹.

The uncertainties are standard deviations of the mean values.

^a25 mM Tris, pH 8.0, 100 mM NaCl, 5 v/v % glycerol, 10 mM DTT and others in 5 mM HEPES, pH 7.4, 150 mM NaCl, 20 mM MgCl₂, and 2 v/v % DMSO.

^bCalculated T_G^* values were obtained by adding the temperature difference determined from equation (4.3) to the experimental T_G from DSC scan of just the protein solution.

Table 4-5. Thermodynamic transition parameters of isoform 2 and its C162S mutant and in the presence of drug-inhibitors from fits of a two-state transition model to the DSC data.

[Protein] μM	Drug-inhibitor	T_G $^{\circ}\text{C}$	$T_G(\text{cal.})^b$ $^{\circ}\text{C}$	$\Delta_{\text{trs}}H_{\text{vH}}$ kJ mol^{-1}	$\Delta_{\text{trs}}H$	Ratio
<i>Isoform 2</i>						
5.74 ^a		50.0 ± 0.1		831 ± 28	353 ± 42	0.43 ± 0.06
[2.87]		$[53.4 \pm 1.0]$		$[740 \pm 11]$	$[376 \pm 26]$	$[0.51 \pm 0.04]$
6.22–11.4	SKF 86002	54.9 ± 0.1	58.0	468 ± 27	460 ± 52	1.00 ± 0.14
4.35–9.94	SB 203580	57.3 ± 0.1		561 ± 31	392 ± 46	
	2 nd transition	65.1 ± 0.1		571 ± 29		
3.79–10.2	p38 INH.1	60.5 ± 0.1	65.0	525 ± 35	465 ± 65	
	2 nd transition	66.7 ± 0.1	64.2	843 ± 66		
<i>Isoform 2 complex from displacement ITC titration</i>						
6.73–10.0	p38 INH.1	61.5 ± 0.1	65.0	465 ± 45	388 ± 65	
	2 nd transition	66.3 ± 0.3	64.2	803 ± 73		
<i>Isoform 2 C162S</i>						
17.3–26.3 ^a		45.5 ± 0.1		859 ± 16	191 ± 16	0.22 ± 0.02
12		48.0 ± 0.1		828 ± 12	153 ± 9	0.18 ± 0.01
4.5–8.9	SKF 86002	57.4 ± 0.1	52.1	476 ± 7	573 ± 48	1.20 ± 0.17
7.08–15.4	SB 203580	60.0 ± 0.1	56.7	535 ± 11	468 ± 50	0.88 ± 0.10
6.35–14.3	p38 INH.1	65.1 ± 0.1	57.4	589 ± 15	577 ± 62	0.98 ± 0.11

The values in [] were determined at slower DSC scans of $15^{\circ}\text{C hr}^{-1}$. ^a25 mM Tris, pH 8.0, 100 mM NaCl, 5 v/v % glycerol, 10 mM DTT and others in 5 mM Hepes, pH 7.4, 150 mM NaCl, 20 mM Mg Cl₂, and 2 v/v% DMSO. ^bCalculated T_G^* values were obtained by adding the temperature difference determined from Equation (4.3) to the experimental T_G from DSC scan of just the protein solution. The uncertainties are standard deviations of the mean values.

The ratios of the calorimetric enthalpy to the van't Hoff enthalpy, 1.7 ± 0.4 for isoform 1 and 0.43 ± 0.06 for isoform 2, are within two standard deviations, respectively, of 0.9 and 0.6, ratios implying that the protein unfolds as a monomer in agreement with the observation that an $A \rightleftharpoons B$ transition model was best fitted to the DSC transition data instead of a $A \rightleftharpoons 2B$ for the typical unfolding of a dimer. Typical unfolding of a dimer would also exhibit a dependence of the transition temperature on concentration, which was not observed in the DSC results of both isoforms of p38 α MAP kinase and the C162S mutants.

The number of transitions at the higher temperatures in Figs. 4-9 and 4-10 and in Tables 4-4 and 4-5 for the drug-protein complexes depends on whether the isoform contains the C162S mutation. Two transitions are observed with SB 203580 binding to isoforms 1 and 2 and with p38 INH.1 binding to isoform 2 at temperatures 4°C (SB 203580-isoform 1 complex) to 20°C (p38 INH.1-isoform 2 C162S complex) higher than the temperatures of the protein alone. Two transitions are also observed with the SB 203580-isoform 2 complex in the presence of 5 mM DTT in the protein solution. In contrast, single transitions are observed with inhibitor binding to the C162S mutants and with the weak SKF 86002 binding to isoform 2. (DSC scans were not performed on the SKF 86002 and p38 INH.1 complexes of isoform 1.) Inhibitor binding to the proteins stabilizes the folded state as evident by the temperature shifts in the transition peaks to temperatures higher than those of the protein alone. In addition, two DSC runs were performed with the SKF 86002 mixed with the p38 INH.1-isoform 2 complex mixtures from the ITC displacement experiments. These results also shown in Table 4-5 were in agreement with the unfolding thermodynamics from DSC scans with just the p38 INH.1 –

isoform 2 complex solutions. Therefore, the ITC displacement reactions were successful in displacing the weaker binding inhibitor, SKF 86002, with the stronger binding inhibitor, p38 INH.1.

The higher transition temperatures of the complexes are due to an increase in the conformational stabilization of the protein in the folded complex state. The increases in T_G were calculated from the ITC results employing equation (4.2), which extrapolates K_b determined from the ITC results up to the denaturation temperature of the complex, and equation (4.3), which determines the increase in the denaturation temperature from the extrapolated value of K_b , the unfolding temperature of the protein, and the unfolding enthalpy. The calculated results are presented in Tables 4-4 and 4-5 in terms of a calculated T_G for the complex, $T_G(I)$. Calculated $T_G(I)$ values for isoform 1 C162S bound to SKF 86002 (54.2°C) and to SB 203580 (53.4°C) and for isoform 2 bound to SKF 86002 (58.0°C) are within 3°C of their experimental values, respectively, of 52.4 ± 0.1 , 55.4 ± 0.1 , and 54.9 ± 0.1 °C. The calculated $T_G(I)$ value for isoform 1 C162S bound to p38 INH.1 (61.8°C) is almost the same as its experimental value of 61.4 ± 0.1 °C and for p38 INH.1 bound to isoform 2, the calculated $T_G(I)$ values of 65.0 and 64.2°C are within 5°C, respectively, of 60.5 ± 0.1 and 66.7 ± 0.1 °C for the two transitions. The enhanced stabilities of the single peak transitions of the weaker bound SB 203580 and SKF 86002 complexes arise simply out of ligand binding only to the folded conformation of the protein. Since the SB 203580 inhibitor binds to the ATP binding site, which is located in the N-terminal domain, and the calculated $T_G(I)$ value for SB 203580–isoform 1 complex of 53.9°C in Table 4-4 exhibits the closest agreement to its experimental value (54.3 ± 0.1 °C) for the first transition, it is attractive to identify the

first transition with the unfolding of the N-terminal domain. The second transition of the drug-isoform complexes could be attributed to unfolding of the C-terminal domain where isoforms 1 and 2 differ in their amino acid sequences. This is substantiated by the difference between the temperatures of the higher temperature transitions of 65.1 – 66.7°C for isoform 2 and of 59.0°C for isoform 1. Interestingly, isoform 1 alone is also slightly less stable with a $T_G = 48.2 \pm 0.1^\circ\text{C}$ than isoform 2 with a $T_G = 50.0 \pm 0.1^\circ\text{C}$.

4.5 Discussion

Globally, the X-ray crystal structure of p38 α MAP kinase isoform 2 consists of a deep channel between two structural domains, the C-terminal domain and the N-terminal domain, connected by a linker of amino acid residues His107 to Ala111 ([80,90-92], see Fig. 4-4). Isoforms 1 and 2 are different in the amino acid sequence between Ile229 and Ala255 out of a total of 360 amino acid residues in a non-functional region of the C-terminal domain near the outer edge of the channel of the protein. Drug-inhibitor binding occurs in the channel at the co-factor ATP binding site in the N-terminal domain as a totally enthalpically-driven interaction with binding affinities ranging from $1.2 \times 10^7 \text{ M}^{-1}$ for SKF 86002 to $5.4 \times 10^9 \text{ M}^{-1}$ for p38 INH.1 at 25°C. The enthalpically-driven nature of the binding reactions can be correlated with the possible interactions described in the X-ray structures of the drug-inhibitor–p38 α MAP kinase isoform 2 complexes [79,90]. The aligned X-ray crystal structures of the wild type isoform 2 complexed with SB 203580 and the isoform 2 C162S complexed with p38 INH.1 are displayed on Fig. 4-11.

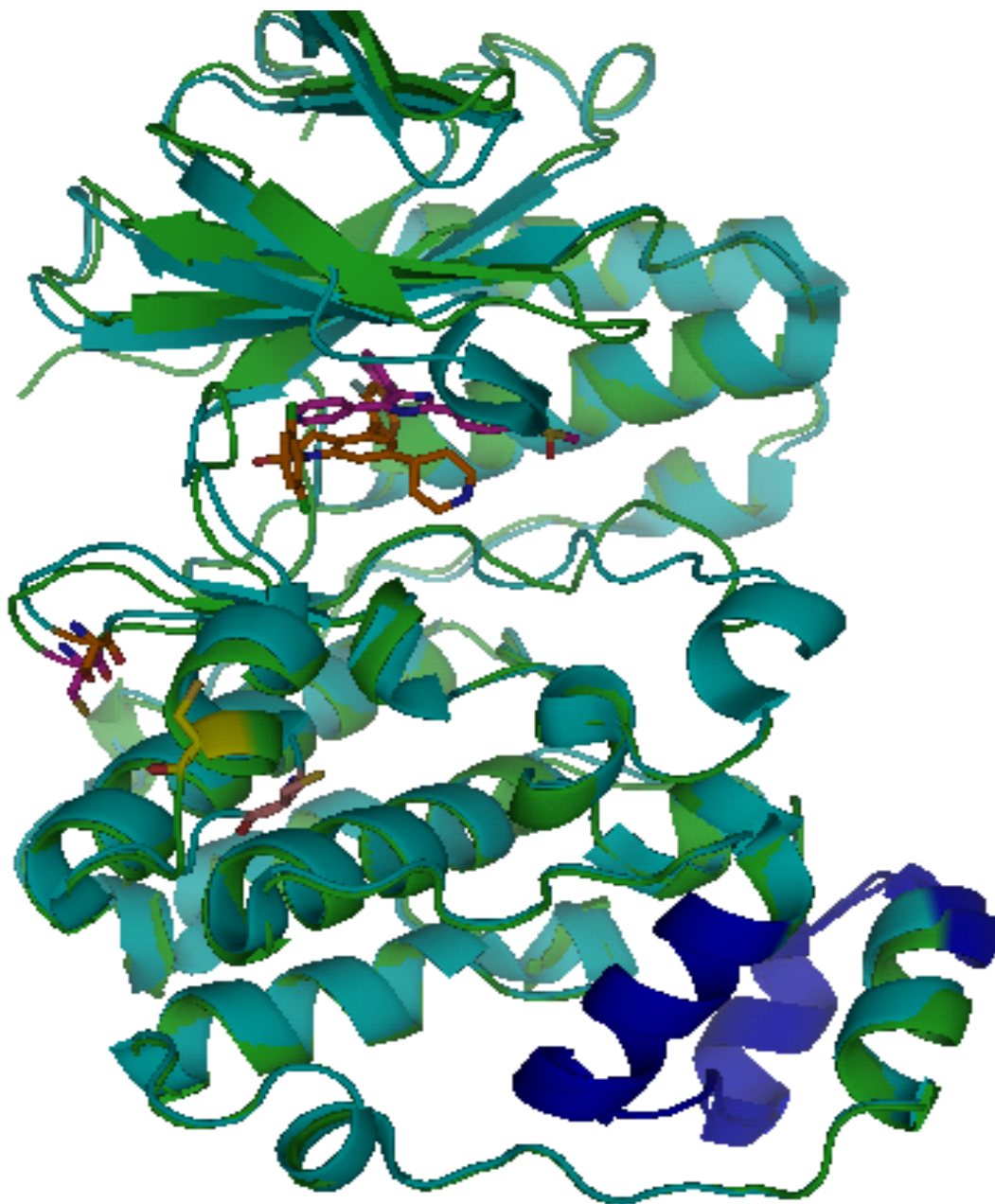


Figure 4-11. Aligned X-ray crystal structures for wt and mutant p38 α MAPK main isoform bound to SB 203580 and p38 INH.1, respectively. In green color is the wt protein with the Cys162 in magenta and in cyan color is the mutant protein with Ser162 in orange. SB 203580 is in magenta, whereas p38 INH.1 is in orange color. The 25- amino acid variable region is in blue.

The following possible interactions with p38 α MAP kinase are observed for all the drug-inhibitors: (1) an interaction between Met109 in the linker region and the pyrimidine groups of SKF 86002 and SB 203580 and the central quinoline group of p38 INH.1, (2) an interaction between Tyr35 in the N-terminal domain and the imidazole-thiazole ring of SKF 86002, the 4-methylsulfinylphenyl group of SB 203580, and the pyrimidine group of p38 INH.1, (3) interactions between a hydrophobic pocket (hydrophobic pocket I) in the N-terminal domain and the fluorophenyl group of SKF 86002 and SB 203580 and the difluorophenyl group of p38 INH.1. Hydrophobic pocket I is formed by the β -strands 3, 4, and 5, and the α -helix C in the N-terminal domain [90]. SKF 86002 exhibits the lowest binding affinities and low specificity as indicated at 30°C by the constancy of the binding constants to within two standard deviations to the isoforms and their C162S mutants. There is an additional possible interaction between the imidazole ring of SB 203580 and Lys53 of the N-terminal domain [79]. The binding affinities of SB 203580 are higher but less than an order of magnitude than the corresponding SKF 86002 binding affinities and also exhibit higher specificity. The $\Delta_b G$ values of SKF 86002 and SB 203580 are in the same range from -45 to -40 kJ mol $^{-1}$ at 25°C while p38 INH.1 exhibits the highest binding affinities with -56 to -53 kJ mol $^{-1}$ at 25°C. The crystal structure of p38 INH.1 bound to p38 α MAP kinase reveals additional possible interactions between the central quinoline group of p38 IHN.1 and His107 and Glu110 in the linker region and between the dichlorophenyl group and a second hydrophobic region (hydrophobic region II) [90]. Hydrophobic region II consists of Val30 in the N-terminal domain and Ile108, Asp112 and Ala111 in the linker region [90]. The additional

interactions would account for the additional $\Delta_b G$ of $\sim -10 \text{ kJ mol}^{-1}$ in the binding affinity of p38 INH.1 yet the specificity of p38 INH.1 is lower than that of SB 203580.

The appearance of two unfolding transitions for the SB 203580 and p38 INH.1 drug-kinase complexes in contrast to a single unfolding transition for the kinase alone shows how complexation with a drug-inhibitor alters the cohesive interactions within the kinase. A large number of new interactions between the drug-inhibitor and the N-terminal domain and linker region of the kinase would more successfully compete with the interactions between the N- and C-terminal domains across the deep channel of the protein. The sequences in the N-terminal domain of both isoforms are the same and the observed shift in the low temperature transition agrees with the estimate for the SB 203580–isoform 1 complex from equation (4.3) based upon drug binding to this domain, while the higher temperature transitions of the complexes are $59.0 \pm 0.1^\circ\text{C}$ for isoform 1 and 65.1 ± 0.1 to $66.7 \pm 0.1^\circ\text{C}$ for isoform 2, both of which have different sequences in the C-terminal domain (Fig. 4-2). Interestingly, these higher transition temperatures are almost the same for the SB 203580–isoform 2 complex as for the much tighter binding p38 INH.1-isoform 2 complex, implying little drug binding effect on the unfolding of the C-terminal domain. Isoform 2 also unfolds at a slightly higher transition temperature of $50.0 \pm 0.1^\circ\text{C}$ than $48.2 \pm 0.1^\circ\text{C}$ for isoform 1. The energetic difference in the stability of the C-terminal domains in the kinase-drug complexes between the two isoforms is $\Delta G = \Delta_{\text{trs}} H \{1 - T_G(\text{isoform 1})/T_G(\text{isoform 2})\} \sim 15 \text{ kJ mol}^{-1}$ and arises from the difference in the amino acid sequences of this domain shown in Fig. 4-3. Structural stability differences between the pure isoforms are also evident in the heat capacity changes upon drug binding. The binding heat capacity changes are negative for drug-inhibitor binding

to isoform 1 and to the C162S mutants of both isoforms while, in contrast, the heat capacity change for isoform 2 binding to SKF 86002 is $2.2 \pm 1.2 \text{ kJ mol}^{-1} \text{ K}^{-1}$ and to p38 INH.1 is $0.59 \pm 0.13 \text{ kJ mol}^{-1} \text{ K}^{-1}$. Negative heat capacity changes are normally observed upon ligand binding to proteins and are attributed to bulk water reorganization upon ligand binding as the ligand or drug-inhibitor goes from the bulk water environment into the hydrophobic binding channel of the protein (termed the hydrophobic effect). A zero or positive heat capacity change would imply that drug binding produces an increase in other contributions such as vibrational contributions of the protein to the heat capacity change that compensate for the hydrophobic effect [52].

The effect of the C162S mutation near the linker region, however, apparently compensates for the reduction in the interactions between the two domains upon high affinity drug binding and, thus, only one unfolding transition is observed for the C162S mutants. The C162S mutation, which is adjacent to a 117-123 surface loop, alters the conformation of the loop by bringing amino residues Cys119 and Gln120 inside the loop near the linker region [96]. The de-coupling between the N- and C-terminal domains upon drug binding could be viewed as the kinase in an “open” form and the coupling between the N- and C-terminal domains in the C162S mutants upon drug binding and in the free kinases as exemplified by a single unfolding transition could be viewed as the kinase in a “closed” form. This change in the conformational stability of the kinase could be important in the enzymatic function of the kinase. For example, the enzyme turnover rate of isoform 2 C162S is lower by 30 % than that of isoform 2 [96] perhaps due to the tendency of the C162S mutation to maintain the kinase in the closed form, thereby

limiting penetration into the channel of the ATP co-factor to its binding site or the ATP converted product ADP from leaving the binding site.

Chapter 5: Effect of the phosphate substrate on drug-inhibitor binding to human purine nucleoside phosphorylase

5.1 Abstract

The thermodynamics of the drug-inhibitors acyclovir, ganciclovir, and 9-benzylguanine binding to human purine nucleoside phosphorylase (hsPNP) were determined from isothermal titration calorimetry as a function of the substrate phosphate ion (Pi) concentration from 0 to 0.125 M and temperature from 15°C to 35°C. At 25°C and with an increase in the Pi concentration from 0 to 50 mM, acyclovir binding becomes more entropically-driven and ganciclovir binding becomes more enthalpically-driven. At 25°C, the tighter 9-benzylguanine binding reaction goes from an enthalpically-driven reaction in the absence of Pi to an entropically-driven reaction at 10 mM Pi, and the enthalpically-driven nature of the binding reaction is restored at 75 mM Pi. Since the dependencies of the driving-nature of the binding reactions on Pi concentration can be simulated by Pi binding to its catalytic site, it is believed that bound Pi affects the interactions of the side chains with the ribose catalytic site. However, the binding constants are unaffected by change in the bound Pi concentration because of enthalpy-entropy compensation. The enzymatic activity of hsPNP was determined by an ITC-based assay employing 7-methylguanosine and Pi as the substrates. The heat of reaction determined from the assay increased by 7.5 kJ mol⁻¹ with increase in Pi concentration from 50 to 100 mM and is attributed to weak binding of the Pi to a secondary regulatory site. Although the binding constants of acyclovir and ganciclovir at 20 µM hsPNP were in agreement with the inverse inhibition constants determined from the ITC enzyme inhibition assays at 60 nM, the binding constant of 9-benzylguanine, which interacts with

Phe159 from an adjacent subunit, decreased from $5.62 \times 10^5 \text{ M}^{-1}$ to $1.14 \times 10^5 \text{ M}^{-1}$. This reduction in the 9-benzylguanine binding affinity along with a 7-fold increase in the specific activity of hsPNP at 14.5 nM results from partial dissociation of the hsPNP trimer into monomers below the 60 nM level.

5.2 Introduction

Many drug-targeted enzymes, particularly the regulatory enzymes, are multi-substrate enzymes where it is not known how the potency of a drug-inhibitor targeting one substrate site is affected by the presence of the other substrate in an adjacent site. Many bi-substrate enzymes exhibit “substrate activation phenomenon” where the enzymatic reaction of the enzyme at low concentrations of one substrate is accelerated in the presence of the second substrate. Purine nucleoside phosphorylase (PNP) is a ubiquitous enzyme that utilizes ribo- and deoxyribonucleosides and phosphate in adjacent sites to catalyze the reversible cleavage of the N-glycosidic bond of the ribo- and deoxyribonucleosides and subsequent phosphorylation of the ribose moiety as shown in Fig. 5-1 [101,102]. PNP exhibits substrate activation phenomenon where the slow hydrolysis of the β -purine nucleoside is accelerated by the presence of phosphate ions (Pi) in the buffer solution. A decrease in the inhibition potency by drug-inhibitors is also observed for human PNP (hsPNP) in the presence of high concentrations of the phosphate substrate ion (Pi) [101].

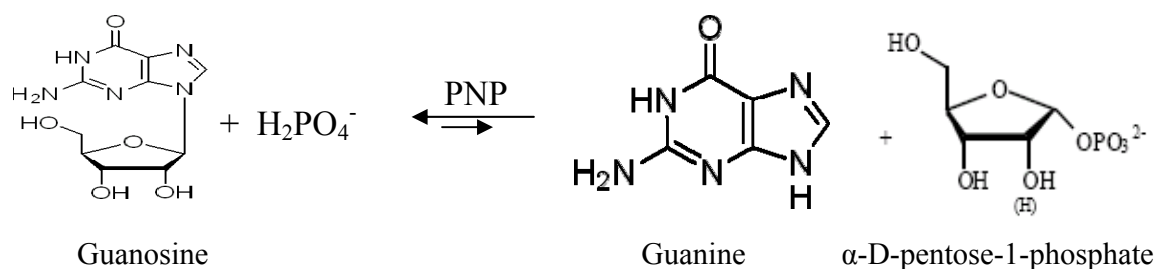


Figure 5-1. A schematic representation of the reaction catalyzed by purine nucleoside phosphorylase.

The enzyme reaction catalyzed by PNP is important in the salvage pathway for recycling purine ribo- and deoxyribonucleosides to generate free purine bases and is an alternative to the *de novo* purine biosynthetic pathway [103]. The enzymatic function of human PNP (hsPNP) has important medical implications. It was first described by Giblett et al. in 1975 as a rare autosomal recessive cellular immunodeficiency disorder in that hsPNP deficiency in humans leads to an impairment of T-cell function, usually with no apparent effects on B-cell function [101]. The mechanism by which hsPNP deficiency causes selectively impaired T-cell maturation and differentiation is not completely understood. However, it has been previously suggested that hsPNP deficiency causes the accumulation of dGTP, a potent feedback inhibitor of ribonucleotide reductase, which catalyzes the conversion of NDPs to dNDPs, and eventually impaired DNA synthesis [101]. Therefore, T-cell leukemias and lymphomas can be impaired by designing efficient inhibitors that target hsPNP. This has led to drug inhibition targeting of hsPNP for chemotherapeutic intervention in the treatment of cancer [102]. In addition, targeted

anticancer gene therapy is being developed by exploiting the distinct substrate specificity between *E. coli* PNP and hsPNP where adenosine is exclusively a natural substrate of the *E. coli* PNP [102]. The strategy here is to transfect human tumors with the gene for *E. coli* PNP to express the *E. coli* PNP in the tumor where it exclusively recognizes a chemotherapeutic prodrug of adenosine and subsequently cleaves the prodrug to an active, cytotoxic form that kills the tumor cells [102,104]. HsPNP has also been considered an attractive drug target in the treatment of other T-cell related autoimmune diseases, e.g. rheumatoid arthritis, and multiple sclerosis [102]. Furthermore, the role of hsPNP in T-cell mediated immunity makes it a drug target for the suppression of the host-graft response in organ transplantation [102]. The X-ray crystal structures of PNP from different organisms including various bacterial species show that *E. coli* PNP and *salmonella typhimurium* PNP are hexameric whereas mammal PNP is trimeric [101].

The crystal structure for hsPNP [105] as well as its structures with bound drug-inhibitors exhibit the following characteristics: the enzyme is an active trimer with three independent substrate binding sites located near the subunit interface: the purine-binding site, composed of Ala116, Phe200, Glu201, Val217, Met219, Thr242, and Asn243, is proximal to the ribose-binding site, composed of Tyr88, Phe159, Phe200, His86, His257, and Met219, and to the catalytic Pi-binding site, composed of Ser33, Arg84, His86, and Ser220. The residues Phe200 and Met219 are involved in binding of the purine and ribose, while His86 is involved in binding of both the ribose and Pi. There is evidence from the x-ray crystallography of hsPNP for an additional Pi-binding site, possibly a Pi regulatory-site that is composed of Gln44 and Arg148 [105]. The hsPNP binding sites are near the subunit interface so that residues Phe159 and Arg148 are from the adjacent

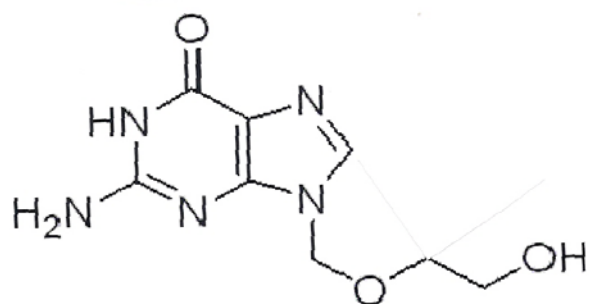
subunit [106,107]. A loop composed of residues 241-260 in the hsPNP crystal structure acts as a gate that opens upon substrate or drug-inhibitor binding [107-109]. This loop, which includes residues Thr242 and Asn243 from the purine-binding site and His257 from the ribose-binding site, becomes highly ordered upon substrate binding [110]. The mutation of Tyr249 of the loop to tryptophan in hsPNP yielded a maximum Trp fluorescence peak red-shifted to 358 nm, indicating that the loop is exposed to the solvent [110].

The role of the second substrate, Pi, is more complex since it also facilitates the rate-limiting release of the tightly-bound purine bases in PNP [110,111]. However, Pi also exhibits negative cooperativity in the calf spleen PNP (bsPNP) enzyme reaction, which was earlier attributed toward a conformational change, promoting dissociation to a more active monomer, or coupling between two Pi sites on the same monomer subunit [107]. A decrease of the Pi concentration from 50 mM to 1 mM increased the binding affinity of the multiphosphorylated acyclovir drug-inhibitors to hsPNP [112]. The fluorescence intensity of Trp249 of the Tyr249→Trp mutant of hsPNP increased upon saturation with bound Pi, indicating that Pi causes only a change in the environment of Tyr249 while retaining the water solvent exposure of the loop [110]. Previously performed enzyme kinetic studies on calf spleen PNP (bsPNP) also reported an increase in specific bsPNP activity upon dissociation of the enzyme and the dissociation was enhanced at higher Pi concentrations [107]. Alignment of the two protein sequences for bsPNP and hsPNP using BLAST from the NCBI website resulted in 87% identity at the amino acid level so it is highly possible that high Pi concentration may have a similar affect on hsPNP. It is not clear if the observed decrease in the potency of drug-inhibitors

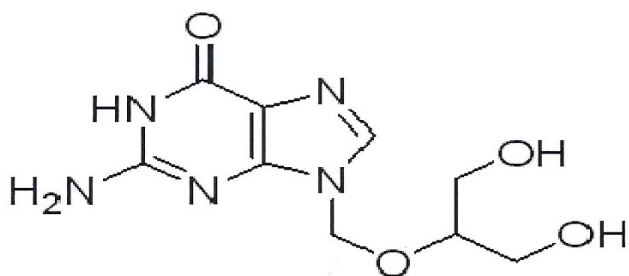
at high Pi concentration results from direct competition between the drug-inhibitor and the binding of Pi to the substrate binding site or from further hindrance of drug-inhibitor binding to the substrate binding site by an increase in Pi binding to the secondary Pi regulatory site composed of Gln44 and Arg148 [105].

The goal of this investigation is to determine how the potency/binding affinity of three drug-inhibitors, acyclovir, ganciclovir, 9-benzylguanine that basically target the purine binding site is affected by the presence of the second substrate, Pi, in its adjacent binding site. The binding thermodynamics of the three drug-inhibitors were determined from isothermal titration calorimetry (ITC) measurements as a function of the Pi concentration. The drug-inhibitors are guanine derivatives with different side chains attached to the N9 position of the guanine ring as shown in Fig. 5-2: acyclovir has a simple acyclic 2-hydroxy-ethoxy-methyl side chain, ganciclovir has a bulkier 2-hydroxy-1-methoxy-ethoxy-methyl side chain, and 9-benzylguanine has benzyl ring for the side chain. The inverse binding constants have been previously determined as inhibition constants (K_i) from enzyme inhibition assays employing Kalckar's assay [113]. Kalckar's assay follows the phosphorolysis catalyzed reaction by monitoring spectrophotometrically oxidation of the product, hypoxanthine, into uric acid in the presence of an enzyme, xanthine oxidase, subsequently added to the reaction mixture [113]. Acyclovir, an antiviral agent, is a weak competitive inhibitor of hspNP with an inhibition constant $K_i = (91 \pm 9.7) \mu\text{M}$ [112,114]. Ganciclovir, a pro-drug nucleoside analog used in cancer research, possesses a 3-fold lower inhibition constant than acyclovir with a K_i value of $30 \mu\text{M}$ also at 50 mM Pi concentration and pH = 7.4 [114].

a)



b)



c)

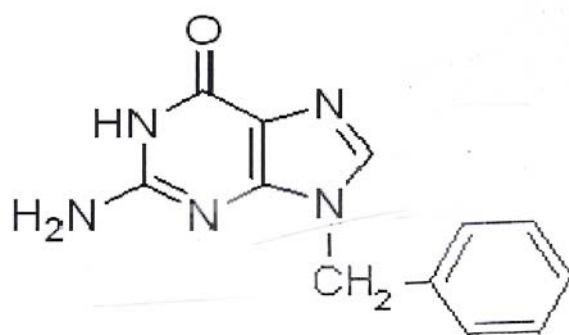


Figure 5-2. Structures of the drug-inhibitors for hsPNP: a) Acyclovir; b) Ganciclovir; c) 9-benzylguanine

9-Benzylguanine exhibits the highest potency with the lowest inhibition constant of $7.0 \pm 0.9 \mu\text{M}$ at 1 mM Pi concentration [115].

Recently reported ITC measurements on the binding of bsPNP to a acyclovir derivative where the $-\text{CH}_2-\text{O}-\text{C}_2\text{H}_4-\text{OH}$ side chain is replaced by a longer phosphonate side chain, $-\text{CH}_2-\text{CH}(\text{CH}_3)-\text{O}-\text{CH}_2-\text{PO}_3$, exhibited a more than two-fold increase in the binding enthalpy in the presence of 0.35 mM Pi without any change in the binding affinity [116]. An X-ray crystal structure of this complex also showed that in contrast to Pi, the phosphonate group re-directs the side-chain of Arg84 away from the binding site and, thus, lowers the expected inhibitory potency of the drug-inhibitor [116]. In addition, the specific enzymatic activity of hsPNP and inhibition of the enzyme activity by the 3 drug-inhibitors was determined as a function of hsPNP and Pi concentration by a simple ITC method not involving the addition of extraneous xanthine oxidase as employed in Kalckar's method. Since the dissociation of bsPNP at low PNP concentrations increased its activity and possibly its drug inhibition, the degree of association of the hsPNP was also monitored at the low hsPNP concentrations of the enzyme inhibition assays by size exclusion chromatography.

5.3 Materials and Methods

5.3.1 Materials

Human recombinant purine nucleoside phosphorylase (hsPNP) expressed in *E.coli* was obtained from Calbiochem with a specific activity ≥ 25 units/mg and used without any further purification. A 10% SDS electrophoresis gel exhibited only one band at the molecular mass of the monomer, $32,000 \text{ g mol}^{-1}$, thus, validating the purity of the

PNP. Since the detection level is about 0.1 μg and the band contained 0.9 μg of PNP, the PNP was at least 90 % pure protein. The acyclovir and ganciclovir were obtained from Sigma-Aldrich and were reagent quality. The 9-benzylguanine was also obtained from Sigma-Aldrich. A HPLC analysis of the drugs with a C18 column exhibited a single elution peak for each of the drugs, indicating > 95 %. The sodium monophosphate, sodium diphosphate, potassium monophosphate, potassium diphosphate, 7-methylguanosine substrate, HEPES, and Trizma base were obtained from Sigma-Aldrich and were reagent quality. The hsPNP was extensively dialyzed in the appropriate buffer prior to the binding and enzyme kinetics measurements. The concentration of the hsPNP monomer in solution was determined from UV absorption measurements using a calculated extinction coefficient of $2.883 \times 10^4 \text{ M}^{-1}\text{cm}^{-1}$ at 280 nm [117]. The drug-inhibitor solutions were made by dissolving known mass amounts of the drug in the buffer dialysate and determining the concentrations from UV absorption measurements. The extinction coefficients of acyclovir and ganciclovir were from Aldrich-Sigma and were $1.18 \times 10^4 \text{ M}^{-1}\text{cm}^{-1}$ at 255 nm for acyclovir and $1.20 \times 10^4 \text{ M}^{-1}\text{cm}^{-1}$ at 256 nm for ganciclovir. An experimentally extinction coefficient of $1.06 \times 10^4 \text{ M}^{-1}\text{cm}^{-1}$ at 271 nm was determined for 9-benzylguanine from dissolving known masses of the 9-benzylguanine in 100 % ethanol and assuming the extinction coefficients would be the same as in water.

5.3.2 Drug-inhibitor Binding Reactions by ITC

For all of the ITC binding experiments, the sample vessel of a Microcal, Inc. VPITC was filled with the hsPNP solution at monomer concentrations $20 \times$ lower than

the drug-inhibitor concentrations in the stirrer syringe. For the binding experiments reported in this paper, fifteen different buffers were used, 50 mM Tris-HCl buffer with 0, 1.0, 5.0, 10, 50 75 and 100 mM sodium phosphate at pH = 7.4, and just 1.0, 2.5, 5.0, 10, 50, 75, 100 and 125 mM sodium phosphate buffer at pH = 7.4. ITC measurements were also performed in 10 mM sodium phosphate buffer at pH 7.4 containing different amounts of salt, 0.150 M NaCl and 0.500 M NaCl. The appropriate dialysis buffer was in the reference vessel of the ITC, and used for rinsing of the sample vessel for preparation of the ITC experiment. The drug-inhibitor solution was first titrated into the dialysate to determine any heats of dilution of the drug-inhibitor solution. Then the sample vessel of the ITC was rinsed thoroughly several times with the dialysis buffer and filled with 5 to 50 μ M of the hsPNP solution. Five to ten microliter aliquots of the drug-inhibitor solution were added to the hsPNP solution until well past saturation of the hsPNP binding sites as evident by the appearance of titration peaks of the same amplitude as those of the drug-inhibitor dilution titration peaks. The analysis of the titration of the drug-inhibitor solution into the hsPNP solution consisted of first subtracting an average heat of dilution of the drug-inhibitor solution from the binding isotherm and then fitting the resulting binding isotherm to a single site 1:1 binding model equation employing the monomer concentration of the hsPNP to determine values for n , $\Delta_b H$, and K_b as described previously [28]. The fitting procedure was performed by the software program Origin from Microcal, Inc. Values of the binding free energy change ($\Delta_b G^\circ$) and the binding entropy ($\Delta_b S^\circ$) were then determined from the fundamental equation of thermodynamics:

$$\Delta_b G^\circ = - RT \ln \{ K_b \} = \Delta_b H^\circ - T \Delta_b S^\circ \quad (5.1)$$

The heat capacity change for the binding reaction, $\Delta_b C_p$, was determined as the slope of the assumed linear dependence of the binding enthalpy on temperature.

Uncertainties in n , K_b , and $\Delta_b H^\circ$ for each ITC scan were generated from the final iterative fit of the single site binding model to the ITC isotherm data. Each ITC reaction was performed at least twice and the uncertainties in the values of n , K_b , and $\Delta_b H^\circ$ of each ITC scan were employed as weighing factors in determining average values for n , K_b , and $\Delta_b H^\circ$ from the ITC reactions. The uncertainties are, thus, reported as standard deviations of the average n , K_b , and $\Delta_b H^\circ$ values.

5.3.3 Enzyme Assays by ITC

The enzyme kinetic assays were performed with the same VP ITC from Microcal, Inc., as employed in the drug binding measurements. The enzyme kinetics of hsPNP with the substrate 7-methylguanosine were determined in terms of the Michaelis constant (K_m), the catalytic constant (k_{cat}), and the enzymatic heat of reaction ($\Delta_r H$). The hsPNP solution obtained from Calbiochem, Inc. was dialyzed against the dialysis buffer consisting of in 100 mM HEPES buffer at pH = 7.0 containing 50 mM or 100 mM potassium phosphate. A 5 mM 7-methylguanosine substrate solution was loaded into the injector syringe and the dialysis buffer into the sample vessel of the ITC. Several injections of the substrate into just the dialysis buffer were performed to determine the heat of dilution for the substrate. After the sample cell was rinsed several times with the dialysis buffer, the cell was filled with the protein solution and several single-injection experiments were performed with an injection volume of 25 μ L of the 5 mM substrate solution into the protein solution. Sufficient time was programmed into the ITC to allow

for the baseline to re-equilibrate to its original level before continuing on to the next injection. After each injection the resulting profile was analyzed using the Origin 7.0 enzyme/substrate model to obtain values for K_m , k_{cat} , and $\Delta_r H$ for the enzymatic reaction. The analysis is essentially based on the direct proportionality between the rate of a reaction and the thermal power (heat/time) generated during the enzymatic reaction,

$$\text{Rate} = (1/V * \Delta_r H) * dQ/dt \quad (5.2)$$

where dQ/dt is the thermal power generated by the enzymatic reaction, $\Delta_r H$ is an experimentally determined molar enthalpy for the enzymatic reaction, and V is the cell volume [118]. Since Michaelis-Menten kinetics are assumed, the rate R_t can be expressed as follows:

$$R_t = (k_{cat} * [E]_{tot} * [S]_t) / ([S]_t + K_m * (1 + [I]/K_i)) \quad (5.3)$$

where $[E]_{tot}$ is the total enzyme concentration, and $[S]_t$ is the instantaneous substrate concentration. The equation is valid both in the absence as well as in the presence of a competitive inhibitor at concentration $[I]$ with inhibition constant K_i [119]. This analysis assumes no product inhibition of the enzyme reaction. The kinetic parameters obtained after fitting the Origin 7.0 model for each single injection of a series of injections were within experimental error and thus there was no product inhibition of the reaction velocity. The values of K_m , k_{cat} , and $\Delta_r H$ were determined as average values of the parameters obtained after analysis of several single-injection experiments. For the competitive drug inhibition measurements, the drug-inhibitor at a concentration of 0.012 mM was mixed in the ITC sample vessel containing 60 nM hsPNP prior to the 25 μ L injections of the 5 mM substrate solution into the sample vessel. Each single-injection experiment was analyzed with the Origin 7.0 enzyme/substrate/inhibitor model

by imputing values for the drug-inhibitor concentration and the previously obtained values for K_m , k_{cat} , and $\Delta_r H$ from the single-injection kinetic experiments in the absence of the inhibitor. Values for the inhibition constant (K_i) were determined from the best non-linear least squares fit of the Michaelis-Menten model to the ITC data. The final reported K_i value for each inhibitor was an average of the values from several single injection ITC experiments.

5.3.4 Static light scattering

For investigating the oligomeric state of hsPNP in solution, static light scattering experiments were performed using a miniDAWN TREOS (Wyatt Technology, Santa Barbara, CA). The protein or protein-inhibitor complex samples were filtered with 0.2 μ m filters before loading on the HPLC size exclusion column, Shodex Protein KW-800 Series. Four different buffers were used as the mobile phase: 1) 10 mM HEPES, pH 7.4, 100 mM $(\text{NH}_4)_2\text{SO}_4$, 0.1 mM EDTA, 0.01% NaN_3 ; 2) 10 mM sodium phosphate buffer, pH 7.4 containing 0.12 mM acyclovir; 3) 50 mM Tris-HCl, pH 7.4; and 4) 0.1 M sodium phosphate buffer, pH 7.4. An isocratic pump, Agilent Technologies 1200 Series was used with flow rate set at 0.5 mL/min and all measurements were performed at room temperature. The sample solution was loaded in the 20 μ L loop and subsequently injected onto the column by an Agilent 1200 Series manual injector. The light scattering detector was coupled with Agilent 1200 Series Variable Wavelength UV detector and Optilab rEX RI detector. For each particular experimental set-up, at least two repeat experiments were performed. The average molecular mass of hsPNP in solution was determined from analysis of a Zimm plot of the light scattering as described previously [120]. Bovine

serum albumin (BSA), 20 mg/mL was used as standard to calibrate the measurements. The light scattering data were analyzed using the ASTRA 5.3.1 software program from Wyatt Technology Corporation.

5.3.5 Size exclusion chromatography

For further investigation of any effect of inorganic phosphate on the oligomeric state of hsPNP in solution size exclusion chromatography experiments were performed with an Amersham Pharmacia Biotech instrument supplied with a UV detector. The experimental read-out was the UV absorbance at 280 nm. Two columns were used in our study, Superdex 200 HR 10/30 from Amersham Pharmacia Biotech and Superdex 75 10/300 GL from GE Healthcare. The main property which distinguishes between the two columns is their different optimal separation range for globular proteins. In particular, for Superdex 200 the range is from 10,000 to 600,000 Da M_r , whereas for Superdex 75 it is from 3,000 to 70,000 Da M_r . Since Superdex 75 has a narrower optimal separation range, the presence of hsPNP monomer of 32,000 Da would be better resolved with this column and therefore the experimental results reported later on are obtained using Superdex 75. Each column was calibrated with the appropriate molecular weight standard globular proteins. In particular, Superdex 75 was calibrated with a solution mixture of conalbumin at 75,000 Da, carbonic anhydrase at 29,000 Da, ribonuclease A at 13,700 Da, and aprotinin at 6,500 Da. The composition of the experimental buffer was 100 mM HEPES, 50/100 mM potassium phosphate, 150 mM NaCl at pH = 7.0. The experimental buffer was filtered through 0.2 μ m filter before use and the protein solution sample was centrifuged at high speed for 20 minutes to pellet any aggregates before loading on the

column. All experiments were done at room temperature. For each run the sample volume loaded on the column was 100 μ L. The flow rates during the elution runs were kept within the pressure limits of each column and 0.5 mL fractions were collected during each elution run. The software used for analyzing the size exclusion chromatography data was Unicorn 4.12. In addition, the collected fractions were analyzed separately for PNP activity. The used enzyme assay consisted of monitoring the decrease of the absorbance at 260 nm of the substrate 7-methylguanosine as it gets converted to the product 7-methylguanine by hsPNP.

5.4 Results

Typical ITC titrations of acyclovir and ganciclovir binding to, respectively, 20 and 12.3 μ M hsPNP in, respectively, 5 mM and 100 mM Pi buffer (pH=7.4) at 25°C along with their binding isotherms are shown in Figs. 5-3 and 5-4. A typical ITC titration of 9-benzylguanine binding to 30.2 μ M hsPNP in the presence of 0.1 M Pi (pH=7.4) at 25°C along with its binding isotherm is shown in Fig. 5-5. The thermodynamic parameters of acyclovir, ganciclovir, and 9-benzylguanine binding to hsPNP were determined from fits of an identical single-site binding model to the binding isotherms, employing the monomer concentrations of hsPNP.

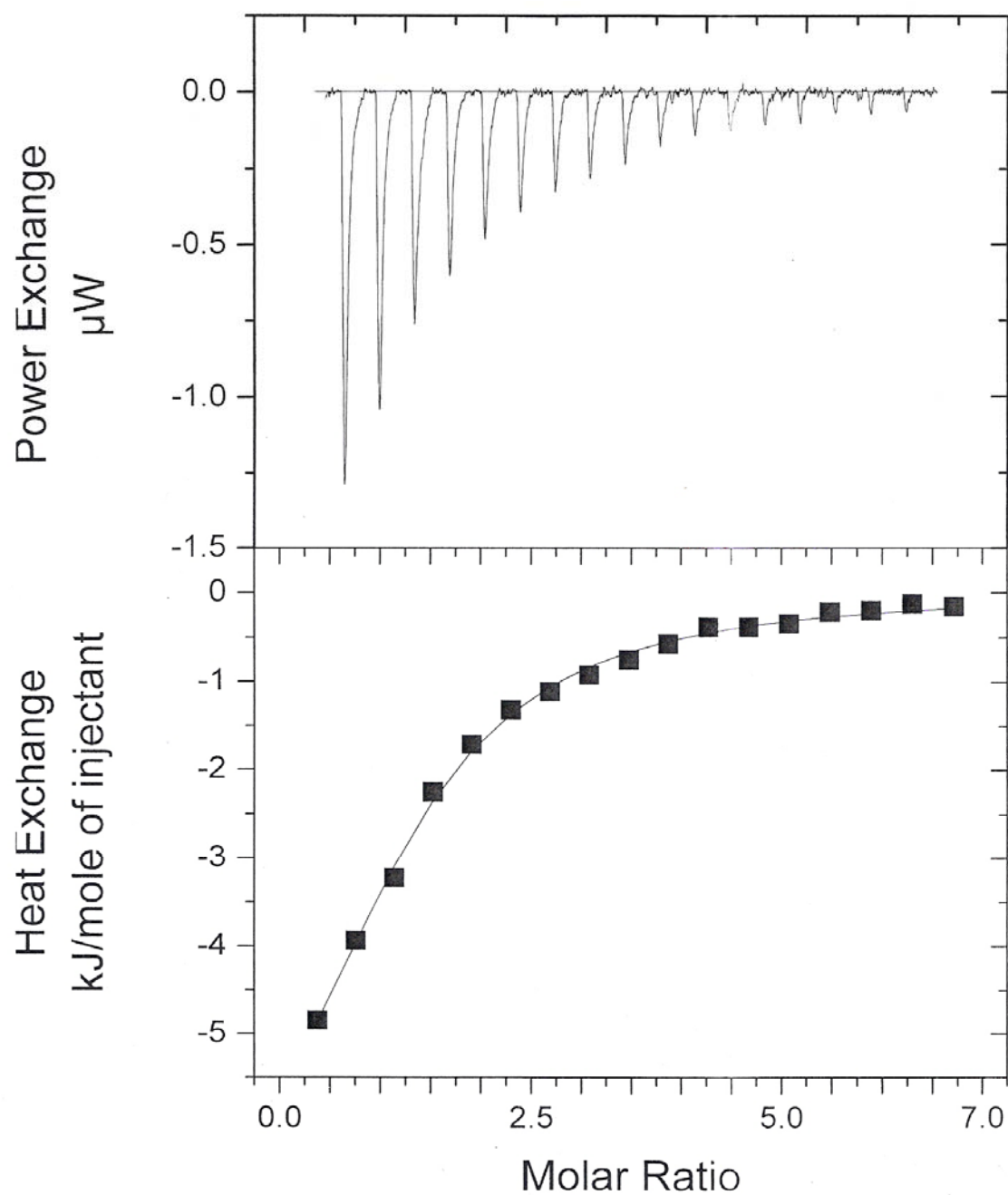


Figure 5-3. An ITC scan of 8 μL aliquots of 1.32 mM acyclovir into 20 μM of hsPNP in 5 mM phosphate buffer (pH = 7.4) at 25 $^{\circ}\text{C}$ (top panel) and fit of a 1:1 binding model to the binding isotherm of this scan (bottom panel).

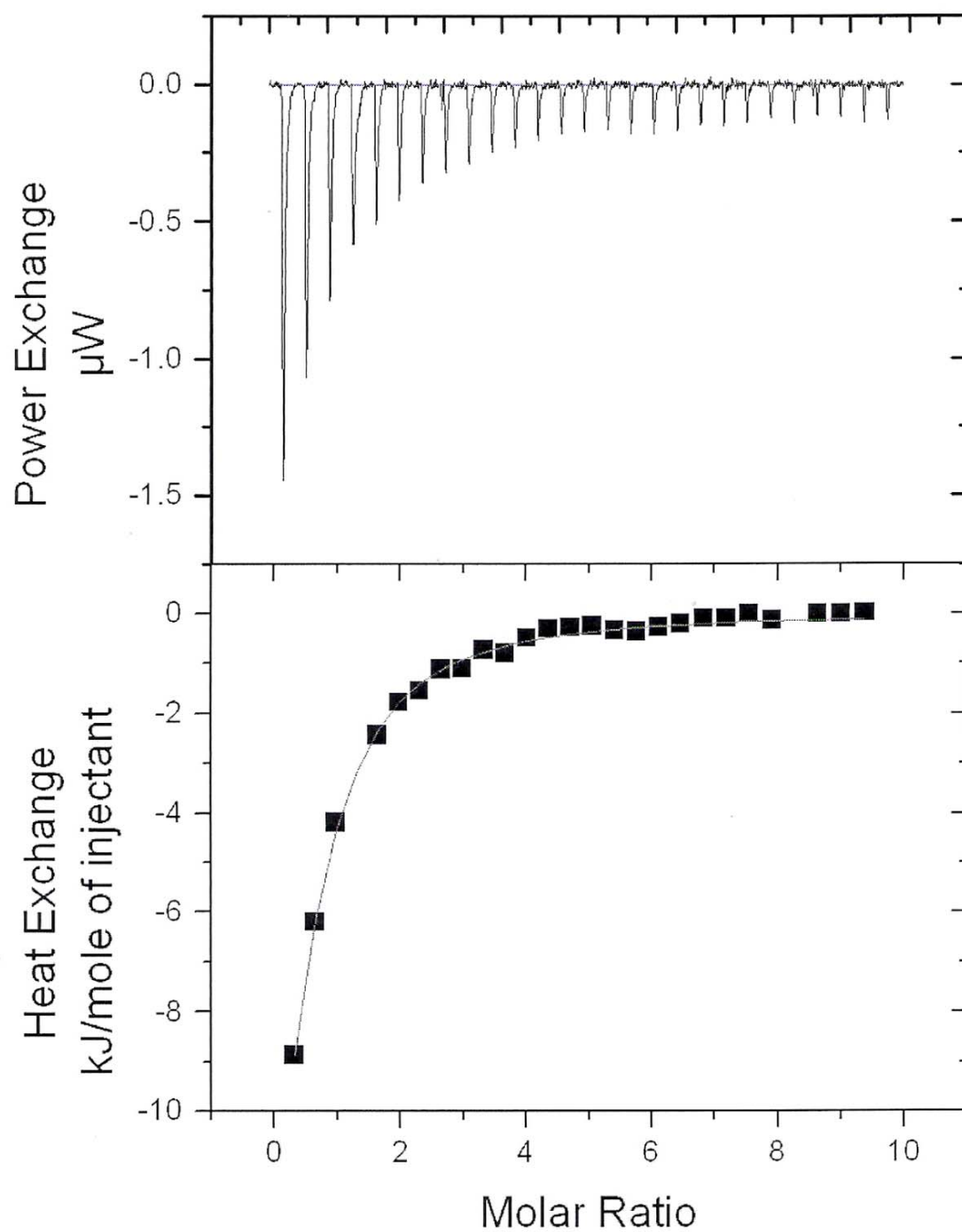


Figure 5-4. An ITC scan of 7 μL injections of a 0.802 mM ganciclovir solution into a 12.3 μM solution of hsPNP in 100 mM phosphate buffer at 25 $^{\circ}\text{C}$ (top panel) and fit of a 1:1 binding model to the binding isotherm of this scan (bottom panel).

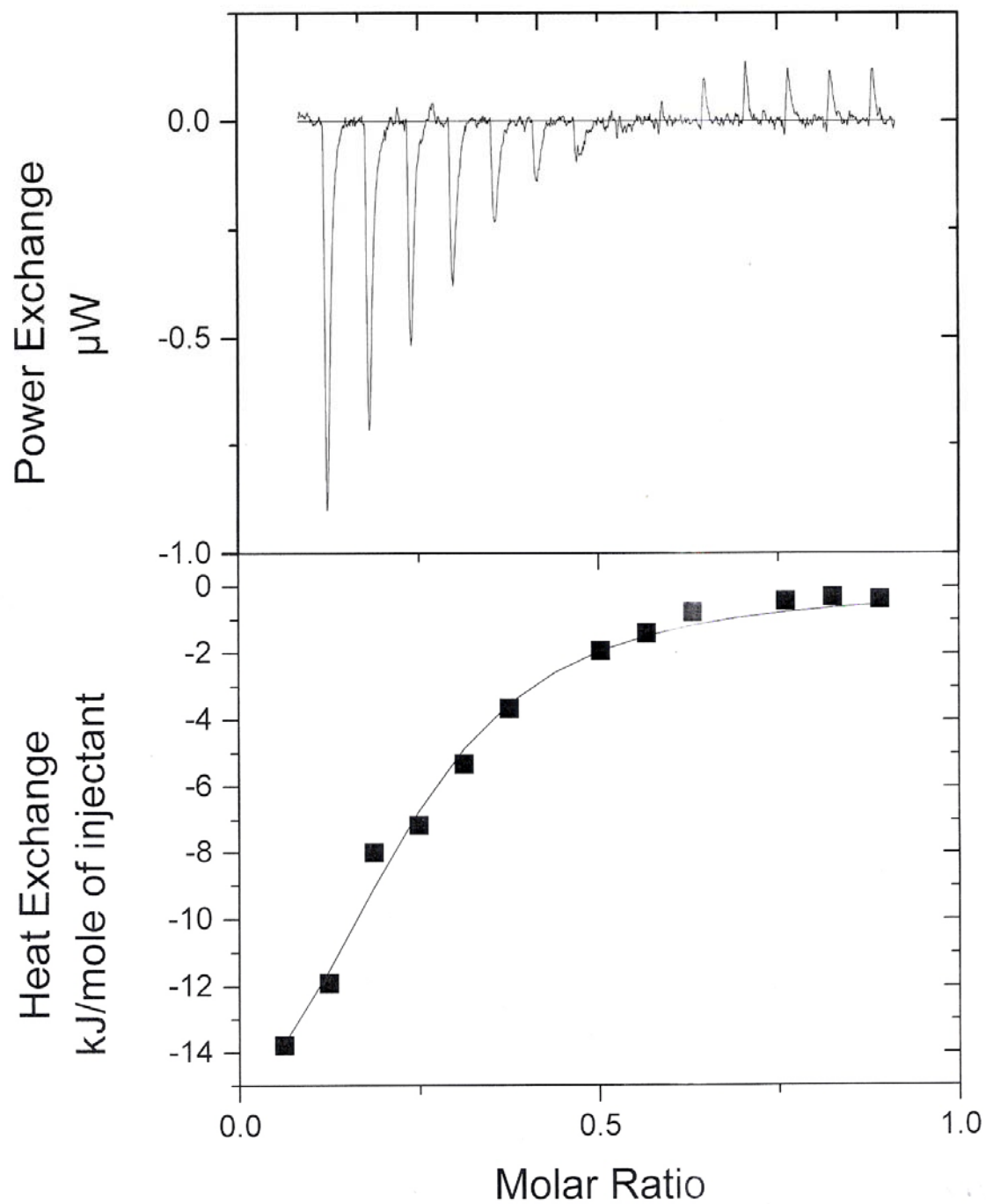


Figure 5-5. An ITC scan of 6 μL aliquots of 0.44 mM 9-benzylguanine into 30.2 μM of hsPNP in 100 mM [Pi] buffer at 25 $^{\circ}\text{C}$ (top panel) and fit of a 1:1 binding model to the binding isotherm of this scan (bottom panel).

Average values of the thermodynamic binding quantities of two to four titrations under different conditions of temperature, salt concentration, Pi concentration in the buffer, and buffer are summarized for acyclovir in Table 5-1, for ganciclovir in Table 5-2, and for 9-benzylguanine in Table 5-3. The hsPNP concentrations ranged from 5 μ M to 33 μ M and the drug concentrations were 14 to 65 \times higher than the corresponding PNP monomer concentrations in the ITC measurements. The ITC measurements were performed at temperatures ranging from 15°C to 35°C, well below the temperature onset of 55°C for denaturation of hsPNP, as observed in preliminary differential scanning calorimetry measurements on hsPNP. The average stoichiometries for acyclovir, ganciclovir, and 9-benzylguanine binding to hsPNP are, respectively, 0.86, 0.93, and 0.42. Since the average stoichiometries for acyclovir and ganciclovir binding to hsPNP are close to one, the concentrations of ganciclovir, acyclovir, and hsPNP determined from UV absorption measurements are assumed to be accurate. In addition, the concentrations of the drug-inhibitors in solution from 0.1 mM to 1.3 mM were unaffected by serial dilution of the phosphate concentration from 10 to 100 mM.

Table 5-1. Thermodynamics of Acyclovir Binding to hsPNP in Buffer at pH 7.4 ± 0.1 from ITC

Results

T °C	[PO ₃] mM	[NaCl]	n	K_b 10^5 M^{-1}	$-\Delta_b G^\circ$	$-\Delta_b H^\circ$ kJ •mol ⁻¹	$T\Delta_b S^\circ$	% Enthalpic
15.0±0.1	10.0	0	0.62±0.23	1.17±0.30	28.0±0.6	12.5±2.1	15.5±2.2	45±8
15.0±0.1	100	0	1.06±0.06	0.82±0.07	27.1±0.2	6.5±0.1	20.6±0.2	24±1
(25.0±0.1	0		0.59±0.03	0.74±0.10	27.8±0.3	21.8±1.4	6.0±1.4	78±5)
25.0±0.1	1.0	0	0.75±0.03	0.63±0.06	27.4±0.2	15.9±1.6	11.5±1.6	58±6
25.0±0.1	2.5	0	0.93±0.11	0.59±0.10	27.2±0.4	11.5±1.7	15.7±1.7	42±6
25.0±0.1	5.0	0	1.06±0.13	0.60±0.14	27.3±0.6	10.5±2.7	16.8±2.8	38±10
25.0±0.1	10.0	0	0.84±0.20	0.72±0.18	27.7±0.6	10.2±1.2	17.5±1.3	37±4
25.0±0.1	50.0	0	0.93±0.15	0.82±0.25	28.0±0.8	6.3±0.1	21.7±0.8	23±1
25.0±0.1	75.0	0	1.02±0.06	0.90±0.10	28.3±0.3	6.0±0.4	22.3±0.5	21±1
25.0±0.1	100	0	0.76±0.28	0.59±0.12	27.2±0.5	10.8±0.1	16.4±0.5	40±1
25.0±0.1	125	0	0.85±0.11	0.65±0.10	27.5±0.4	8.2±1.2	19.3±1.3	30±4
25.0±0.1	10.0	15.0	0.72±0.09	0.94±0.09	28.4±0.2	15.6±2.3	12.8±2.3	55±8
25.0±0.1	10.0	50.0	0.64±0.15	1.42±0.46	29.4±0.8	18.5±7.8	10.9±7.8	63±27
30.0±0.1	10.0	0	0.98±0.04	0.52±0.02	27.4±0.1	12.2±1.6	15.2±1.6	45±6
35.0±0.1	10.0	0	1.10±0.14	0.58±0.14	28.1±0.6	10.9±1.3	17.2±1.4	39±5

() In 50 mM tris buffer at pH =7.4.

Table 5-2. Thermodynamics of Ganciclovir Binding to hsPNP in Buffer at pH 7.4 ± 0.1 from ITC

Results

T °C	[PO ₃] mM	[NaCl]	n	K_b 10^5 M^{-1}	$-\Delta_b G^\circ$	$-\Delta_b H^\circ$ kJ •mol ⁻¹	$T\Delta_b S^\circ$	% Enthalpic
15.0±0.1	10.0	0	0.80±0.03	1.76±0.57	28.9±0.8	10.2±3.0	18.7±3.1	35±10
15.0±0.1	100	0	0.52±0.08	1.77±0.02	29.0±0.3	23.3±3.3	5.7±3.3	80±11
(25.0±0.1	0		1.62±0.27	0.61±0.13	27.3±0.5	5.7±1.2	21.6±1.3	21±4)
25.0±0.1	2.5	0	1.45±0.16	0.86±0.19	28.2±0.5	8.9±0.5	19.3±0.7	32±2
25.0±0.1	5.0	0	1.34±0.10	1.52±0.28	29.6±0.5	7.2±0.7	22.4±0.9	24±2
25.0±0.1	10.0	0	0.63±0.01	0.89±0.16	28.3±0.4	20.8±2.3	7.5±2.3	73±8
25.0±0.1	50.0	0	0.41±0.01	1.08±0.14	28.7±0.3	26.5±2.3	2.2±2.3	92±8
25.0±0.1	75.0	0	0.56±0.14	1.12±0.21	28.8±0.5	21.7±6.2	7.1±6.2	75±21
25.0±0.1	100	0	0.48±0.08	0.95±0.06	28.4±0.2	29.3±2.8	-0.9±2.8	100±10
25.0±0.1	125	0	0.59±0.02	0.74±0.05	27.8±0.2	27.8±0.5	0.0±0.5	100±1.2
25.0±0.1	10.0	15.0	1.15±0.12	0.89±0.11	28.3±0.3	10.0±1.2	18.3±1.2	35±4
25.0±0.1	10.0	50.0	0.99±0.08	1.11±0.12	28.8±0.3	13.2±1.3	15.6±1.3	46±5
30.0±0.1	10.0	0	0.79±0.04	1.02±0.01	29.1±0.2	17.9±1.8	11.2±1.8	62±6
30.0±0.1	100	0	0.78±0.15	0.79±0.11	28.4±0.4	19.9±2.3	8.5±2.3	70±8
35.0±0.1	10.0	0	1.19±0.13	1.28±0.01	29.9±0.3	9.8±0.3	20.1±0.4	33±1
35.0±0.1	100	0	1.50±0.03	0.52±0.01	30.5±0.1	11.2±0.8	19.3±0.8	37±3

() In 50 mM tris buffer at pH =7.4.

Table 5-3. Thermodynamics of 9-Benzylguanine Binding to hsPNP in Buffer at pH 7.4 ± 0.1 from ITC

T °C	[PO ₃] mM	[NaCl]	<i>n</i>	K _b 10 ⁵ M ⁻¹	−Δ _b G°	−Δ _b H° kJ •mol ⁻¹	TΔ _b S°	% Enthalpic
(15.0±0.1	10.0	0	0.28±0.03	6.93±1.84	32.2±0.6	15.3±0.6	16.9±0.8	48±2)
(25.0±0.1		0	0.32±0.01	2.20±0.07	30.5±0.08	47.5±9.0	-17.0±9.0	100±20)
(25.0±0.1	1.0	0	0.26±0.02	8.08±1.77	33.7±0.1	27.3±2.6	6.4±2.6	81±8)
(25.0±0.1	5.0	0	0.50±0.02	3.42±0.39	31.6±0.3	23.1±1.1	8.5±1.1	73±4)
(25.0±0.1	10.0	0	0.50±0.03	5.62±1.43	32.8±0.6	13.9±1.3	18.9±1.4	42±4)
(25.0±0.1	50.0	0	0.28±0.01	5.24±0.51	32.6±0.2	14.8±0.7	17.8±0.7	45±2)
(25.0±0.1	75.0	0	0.30±0.01	8.11±2.01	33.7±0.6	17.8±1.1	15.9±1.3	53±3)
(25.0±0.1	100	0	0.29±0.09	3.94±0.57	31.9±0.4	22.4±2.6	9.5±1.1	70±8)
(30.0±0.1	10.0	0	0.55±0.23	3.14±0.27	31.9±0.2	23.0±2.0	8.9±2.0	72±6)
(35.0±0.1	10.0	0	0.73±0.06	7.19±1.17	34.6±0.4	19.5±0.3	15.1±0.5	56±1)

() In 50 mM tris buffer at pH =7.4.

The binding constants of acyclovir and ganciclovir to hsPNP are about the same and range from $0.52 \times 10^5 \text{ M}^{-1}$ to $1.77 \times 10^5 \text{ M}^{-1}$ for ganciclovir binding at, respectively, 35°C and 15°C. The acyclovir and ganciclovir binding constants at 25°C are about a factor of 3 less than the average binding constant of $4.76 \pm 2.06 \times 10^5 \text{ M}^{-1}$ for 9-benzylguanine. Since the drug-inhibitors, acyclovir, ganciclovir, and 9-benzylguanine

bind competitively to the purine substrate binding to inhibit the enzymatic reaction, their drug-inhibitor binding constants are the same as the reciprocals of their enzyme inhibition constants. The average binding constant of $1.08 \times 10^5 \text{ M}^{-1}$ for ganciclovir binding to hsPNP at 50 mM Pi concentration and 25°C (Table 5-2) is about 3 × higher than $3.3 \times 10^4 \text{ M}^{-1}$, the reciprocal of the reported inhibition constant at 50 mM Pi concentration and 25°C [114]. Similarly, the lower limit of the binding constant of $3.42 \pm 0.39 \times 10^5 \text{ M}^{-1}$ for 9-benzylguanine binding to hsPNP at 5 mM Pi (Table 5-3) is about 2 × higher than $1.4 \times 10^5 \text{ M}^{-1}$, the reciprocal of the reported inhibition constant at 1 mM Pi and 25°C [115]. The binding constants of ganciclovir and acyclovir remain within 2X their average standard deviations with increase in Pi concentration up to 0.125 M and, with the exception of the binding constants of 9-benzylguanine at 50 and 75 mM, the binding constants of 9-benzylguanine are almost within 2 × their average standard deviations over the same increase in Pi concentration. Since values within twice their standard deviations are statistically the same, the binding constants of acyclovir, ganciclovir, and 9-benzylguanine are unaffected by change in the Pi concentration from 0 to 0.125 M. The binding constants of acyclovir and ganciclovir in, respectively, Tables 5-1 and 5-2 are also not affected by an increase in added NaCl concentration from 0 to 0.50 M. The binding reactions are all exothermic from 15.0°C to 35.0°C as shown in Tables 5-1, 5-2 and 5-3, but the driving force of the binding reaction depicted by the percentages of the enthalpic contributions to the binding free energy changes ($\Delta_b H^\circ / \Delta_b G^\circ$) shown in the last column of the tables change with increase in Pi concentration. As the Pi concentration increases from 0 to 50 mM for acyclovir binding to hsPNP at 25°C, the enthalpically-driven nature of the binding reaction decreases from 78 to 23 %. In

contrast, as the Pi concentration increases from 0 to 50 mM for ganciclovir binding to hsPNP at 25°C, the enthalpically-driven nature of the binding reaction increases from 21 to 92 %. The entropically-driven nature of the acyclovir binding reactions and the enthalpically-driven nature of the ganciclovir binding reactions tend to level-off above 50 mM Pi concentration. As the Pi concentration increases from 0 to 10 mM for 9-benzylguanine binding to hsPNP at 25°C, the enthalpically-driven nature of the binding reaction decreases from 100 to 42 % and then increases from 42 to 70 % as the Pi concentration increases from 10 to 100 mM. The dependencies of the acyclovir and the 9-benzylguanine binding entropies and the ganciclovir binding enthalpies on Pi concentration are shown in Fig. 5-6. The functional dependencies of the acyclovir and the 9-benzylguanine binding entropies and the ganciclovir binding enthalpies on Pi concentration appear to follow saturation of a Pi binding site of hsPNP, as shown by the solid lines in Fig. 5-6. However, the solid lines are determined with different Pi binding constants ranging from 250 M⁻¹ for ganciclovir binding to 2.2×10^3 M⁻¹ for acyclovir binding, which is actually the lower limit of the literature Pi binding constant of $4.5 \pm 2.3 \times 10^3$ M⁻¹ [121]. The two solid lines displayed with the 9-benzylguanine results are the same as the solid lines on the displays of the other two drug-inhibitors. A drug-inhibitor to protein binding reaction would be expected to be enthalpically-driven in the absence of any other enthalpically-contributing processes such as a conformational change in the protein or dissociation of the protein upon drug binding. Furthermore, attempts to determine the binding constants of Pi to hsPNP by ITC, even in the presence of acyclovir, and in the presence of ribose, were unsuccessful since there was no detectable exchange of heat upon Pi binding.

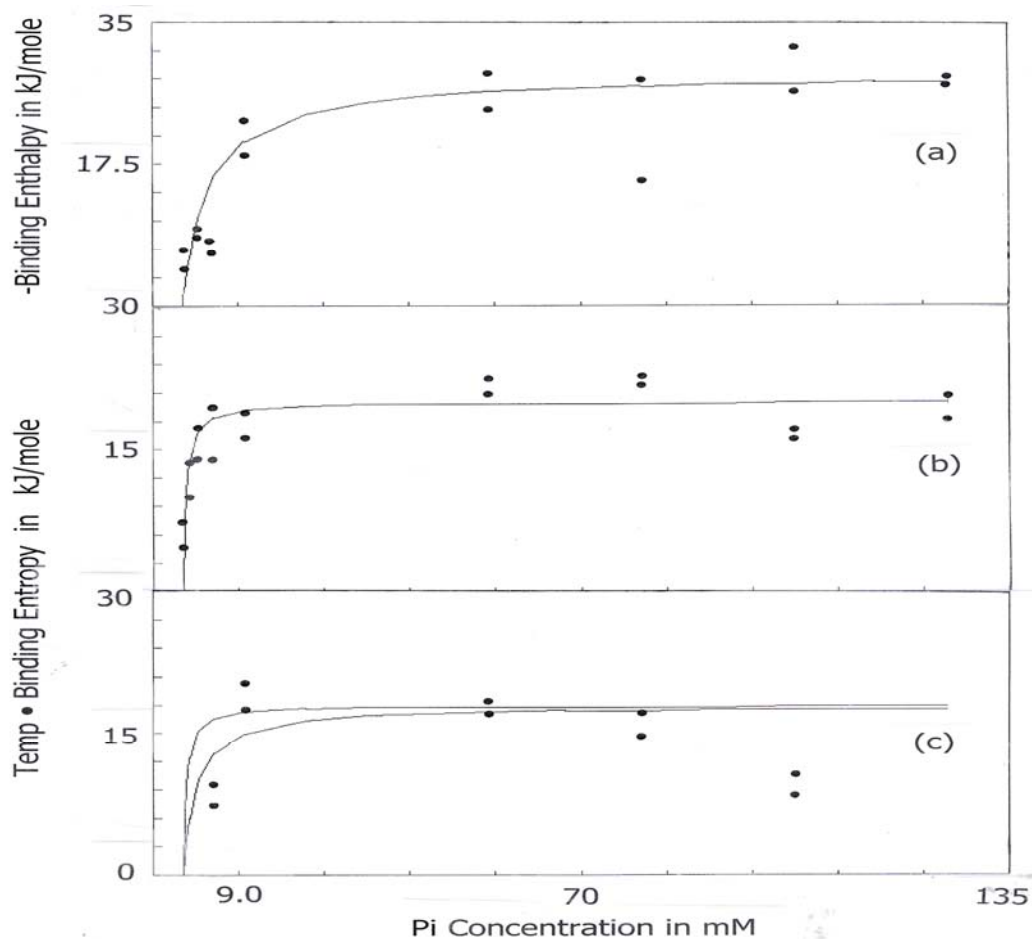


Figure 5-6. Drug-inhibitor thermodynamic binding quantities as a function of Pi concentration. The binding enthalpy of ganciclovir (●●●) as a function of Pi concentration with the extent of saturation of the Pi substrate site calculated using a binding constant of 250 M^{-1} (—) in Panel (a). The product of temperature X binding entropy of acyclovir (●●●) as a function of Pi concentration with the extent of saturation of the Pi substrate site calculated using a binding constant of 2200 M^{-1} (—) in Panel (b). The product of temperature X binding entropy of 9-benzylguanine (●●●) as a function of Pi concentration with the extent of saturation of the Pi substrate site calculated using a binding constant of 2200 M^{-1} (upper —) and a binding constant of 500 M^{-1} (lower —) in Panel (c).

In addition, the application of spectrofluorimetry was attempted in order to obtain a binding constant for Pi to hsPNP. Out of the 289 amino acid residues of hsPNP three are tryptophan (Trp) and nine are tyrosine (Tyr) residues. Therefore, the change of the intrinsic fluorescence of hsPNP was monitored as a function of phosphate concentration. However, the use of intrinsic protein fluorescence in the case of hsPNP as a reporter of phosphate binding did not yield analyzable results, since the measured fluorescence intensity was insensitive to increasing Pi concentrations. Therefore, the use of an extrinsic fluorophore was attempted. The fluorescence properties of the used compound, 2-Aminopurine-2'-deoxyribose-5'-Triphosphate are exclusively due to the adenine analog, 2-aminopurine (2-AP). 2-AP is known as a DNA base analog used to monitor the DNA conformation and dynamics, since its emission is highly sensitive to its environment [46]. However, the fluorescence intensity of the fluorescent phosphate analog was insensitive to addition of hsPNP. Therefore, the application of spectrofluorimetry in order to determine a binding constant of Pi to hsPNP proved unsuccessful.

Since the drug-inhibitor binding sites of each of the sub-monomer units of hsPNP are adjacent to the monomer interfaces in hsPNP, there is a possibility that drug-inhibitor binding would initiate dissociation of the hsPNP trimer during the ITC titration. The results of the light scattering measurements on the hsPNP and the drug-inhibitor hsPNP complexes at ITC concentrations of above 10 μ M, presented on Fig. 5-7, indicate that hsPNP remains in the trimeric state upon drug-inhibitor binding

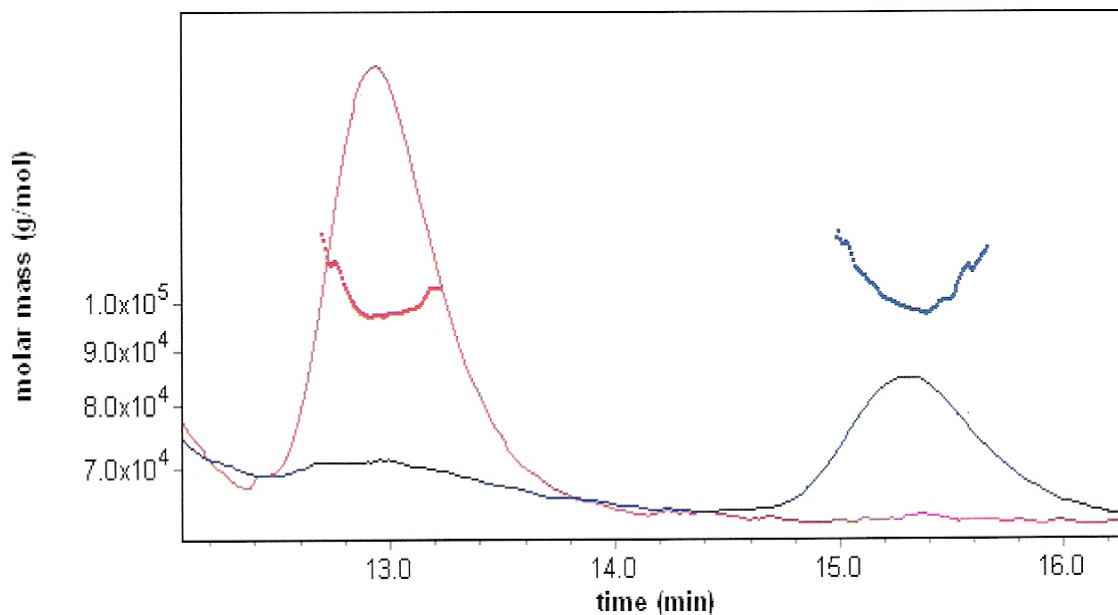


Figure 5-7. Molar mass distribution plot of hsPNP alone (blue color) and in the presence of acyclovir (red color). The solid lines indicate the trace from the refractive index detector and the dotted lines represent the weight-average molecular weights determined for each peak ‘slice’ measured every 0.5 s.

Typical single injection enzyme reaction data from the ITC are presented in Fig. 5-8 and the resulting fit of the Michaelis-Menten reaction model to the ITC data is shown in Fig. 5-9. The reaction goes to completion within 250 s as indicated by the return of the data points to the original baseline. Values for K_m , k_{cat} , and $\Delta_r H$ averaged from several single injections are presented in Table 5-4. At both Pi substrate concentrations and with the exception of 1.33 μM hsPNP at the 50 mM Pi level, all the values of K_m remain within 2X the standard deviations of their average values as the hsPNP concentration decreases from 14.4 μM to 14.2 nM hsPNP as shown in Table 5-4. The values of K_m are in agreement with reported values of K_m of 15 μM from a stopped flow

fluorescence enzyme assay [121] and 14.7 μM and 16.6 μM from a direct spectrophotometric enzyme assay in the presence of 50 mM Pi [121, 122]. Values of k_{cat} , however, at the 50 mM Pi substrate concentration level, exhibit an increase from $9.21 \pm 1.36 \text{ s}^{-1}$ to $73.1 \pm 1.6 \text{ s}^{-1}$ with a decrease of the hsPNP concentration from 1.33 μM to 14.5 nM. Values of k_{cat} at 0.1 M Pi substrate concentration increase from $6.23 \pm 0.71 \text{ s}^{-1}$ to only $24.7 \pm 0.2 \text{ s}^{-1}$, over the same decrease in hsPNP concentration. An increase in k_{cat} at the 50 mM Pi level is responsible for the increase in the specific enzyme activities from $20 \pm 6 \mu\text{mol min}^{-1} \text{ mg}^{-1}$ at 1.33 μM hsPNP to $139.0 \pm 39 \mu\text{mol min}^{-1} \text{ mg}^{-1}$ at 14.5 nM hsPNP. This is in contrast to the constancy of the specific activities at 0.1 M Pi concentration, $46 \pm 2 \mu\text{mol min}^{-1} \text{ mg}^{-1}$ at 28.3 nM hsPNP and $47 \pm 1 \mu\text{mol min}^{-1} \text{ mg}^{-1}$ at 14.5 nM hsPNP. The specific activities at the 50 mM Pi level are in the range of $72 \mu\text{mol min}^{-1} \text{ mg}^{-1}$ from the stopped-flow fluorescence enzyme assay [121] and $82.3 \pm 0.6 \mu\text{mol min}^{-1} \text{ mg}^{-1}$ from the direct spectrophotometric enzyme assay [121] below 0.35 μM bsPNP concentration.

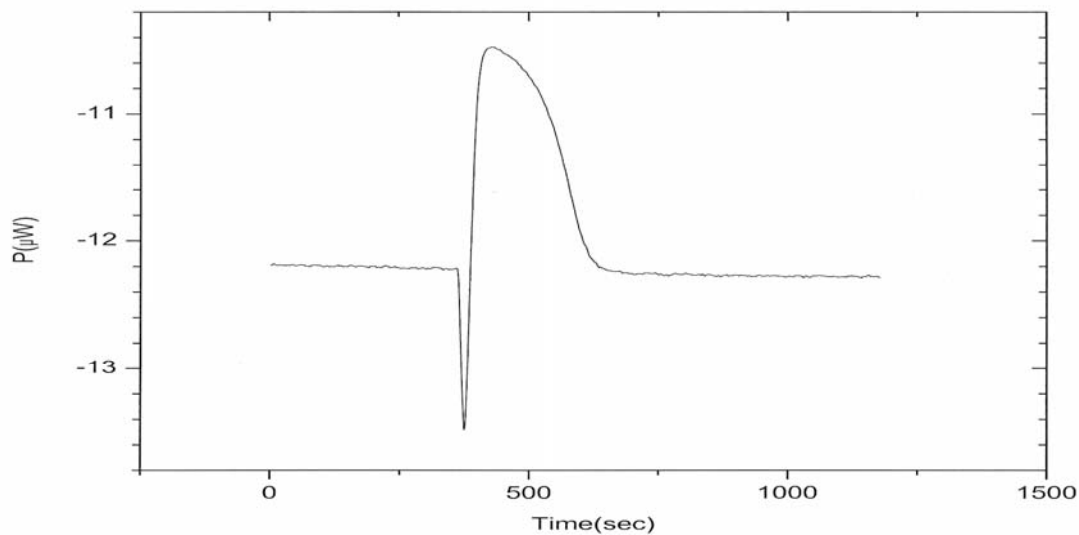


Figure 5-8. An ITC enzyme kinetics scan of a 25 μL single injection of 5 mM 7-methylguanosine into 29.5 nM hsPNP solution in HEPES buffer, pH 7.0 with 50 mM potassium phosphate, at 25°C.

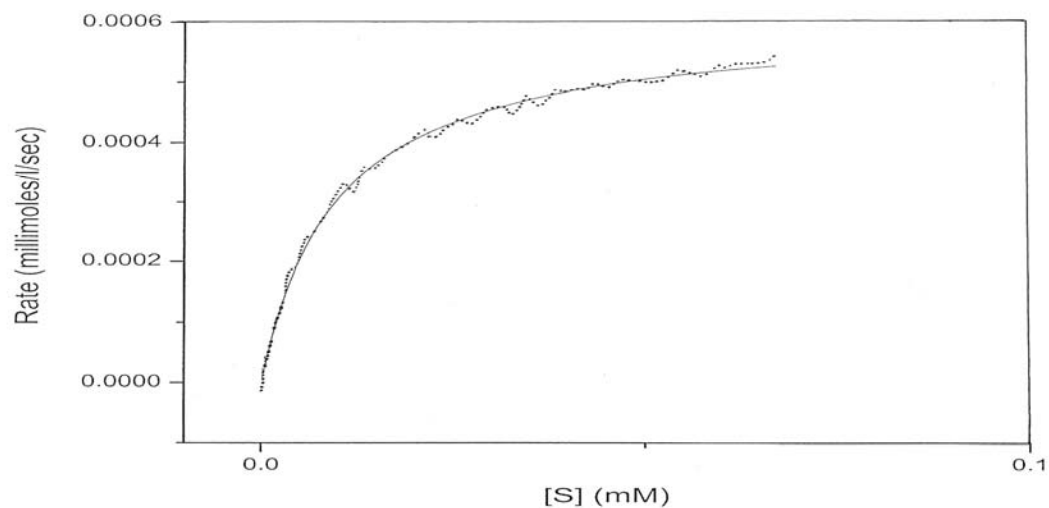


Figure 5-9. A fit of the Michaelis-Menten model (solid line) to the hsPNP enzyme reaction rate as a function of the added 7-methylguanosine concentration derived from the ITC data shown in Figure 4-8.

The lack of product inhibition upon phosphorylation of the hydrolysis products of 7-methylguanosine was observed in the repeatability of the kinetic results upon subsequent ITC injections of the substrate solution into the enzyme solution. The lack of product inhibition was also observed by Kulikowska et al. [122] in earlier enzyme activity assays employing spectrophotometry.

Table 5-4. Enzyme kinetic parameters for hsPNP determined from ITC measurements using 7-methylguanosine as a substrate and calculated specific activity values at 25°C.

[E] _o	k_{cat}	K_{m}	$k_{\text{cat}}/K_{\text{m}}$	specific activity	$\Delta_{\text{r}}H$
M	s ⁻¹	μM	s ⁻¹ • mM ⁻¹	μmol • min ⁻¹ • mg ⁻¹	kJ mol ⁻¹
<u>100 mM HEPES + 50 mM potassium phosphate buffer, pH 7.0 :</u>					
1.33E-06	9.21 ± 1.36	39.3 ± 10.4	240 ± 68	20±6	1.99
2.84E-08	20.4 ± 0.3	9.20 ± 0.51	2256 ± 169	41±3	2.27
1.45E-08	73.1 ± 1.6	12.5 ± 0.9	5860 ± 401	139±10	2.46
<u>100 mM HEPES + 100 mM potassium phosphate buffer, pH 7.0:</u>					
1.44E-06	6.23 ± 0.71	13.0 ± 4.1	488 ± 166	12±4	9.41
2.83E-08	23.0 ± 0.2	13.9 ± 0.5	1674 ± 59	46±2	9.71
1.42E-08	24.7 ± 0.2	16.3 ± 0.3	1548 ± 36	47±1	9.60

The calculated values for the PNP specific activity using the experimentally obtained catalytic constant values (k_{cat}) and the MW of 32kDa for the PNP monomer agree with the reported value for the commercially obtained human PNP (hsPNP) used in this study, in particular specific activity ≥ 25 units/mg.

A large increase in the heat of reaction, $\Delta_r H$, with increase in the Pi substrate concentration, from 2.5 kJ mol⁻¹ at the 50 mM Pi level to 9.6 kJ mol⁻¹ at the 0.1 M Pi level is also observed in the ITC enzyme activity measurements. The gel filtration results in Fig. 5-10 apparently show that hsPNP retains its trimeric state from 15.6 μ M hsPNP down to 60 nM hsPNP, close to the detection level of this method.

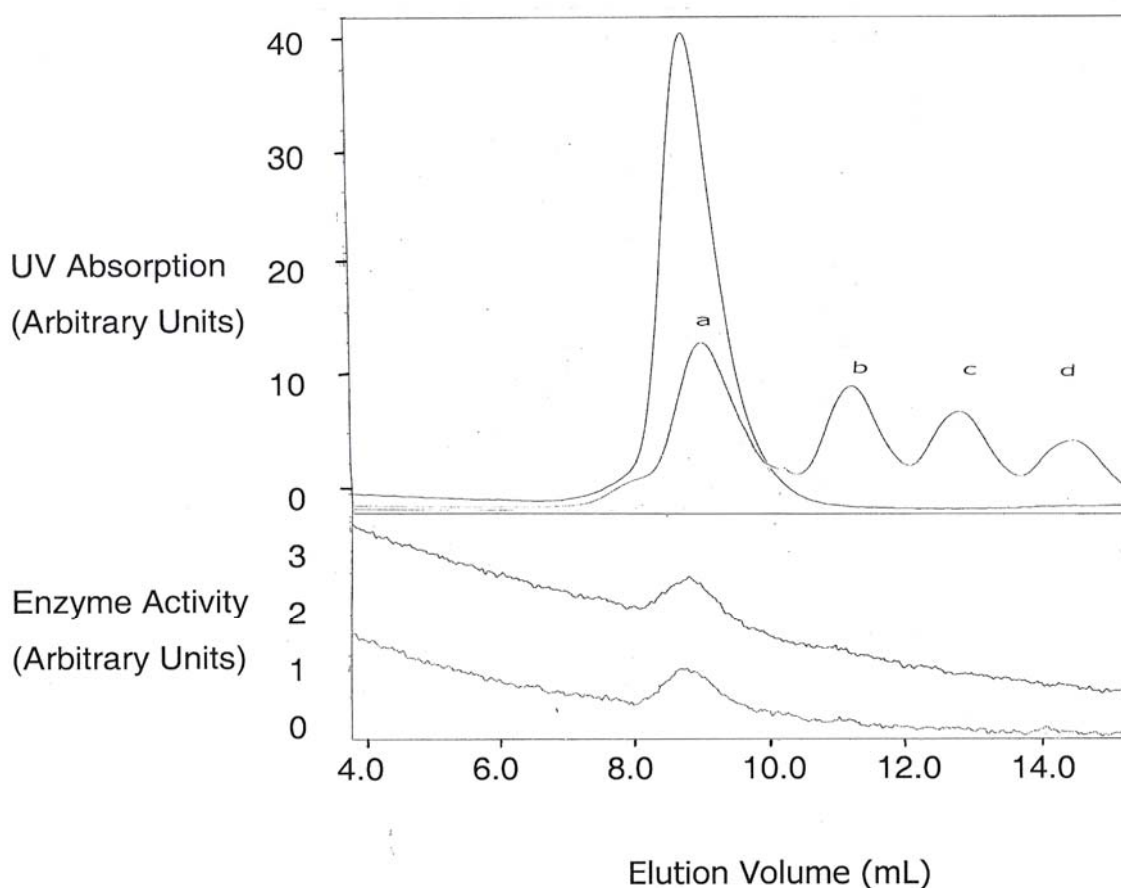


Figure 5-10. Gel filtration chromatography results : (upper plots) elution peak for 15.6 μ M hsPNP solution and four elution peaks for the standard globular proteins used for column calibration labeled **a**) 75 kDa ; **b**) 29 kDa ; **c**) 13.7 kDa, and **d**) 6.5 kDa ; (lower plots) elution peaks for 313 nM hsPNP solution (upper) and 60 nM hsPNP solution (lower).

Typical ITC enzyme inhibition data at 25°C are shown in Fig. 5-11 and a fit of the Michaelis-Menten model to the ITC data is shown in Fig. 5-12. The ITC injection in Fig. 5-11 consists of a 25 μ L injection into a solution of 58 nM hsPNP and 11.6 μ M acyclovir in the buffer at the 50 mM Pi substrate concentration level in the reaction mixture. The calorimetric enzyme inhibition assays at 58 nM hsPNP yield average inverse inhibition constants of $0.94 \pm 0.03 \times 10^5 \text{ M}^{-1}$ for acyclovir and $1.24 \pm 0.20 \times 10^5 \text{ M}^{-1}$ for ganciclovir, as summarized in Table 5-5. The inverse inhibition constants of acyclovir and ganciclovir are close to their ITC determined binding constants in the higher 10 μ M hsPNP concentration range. This agreement would tend to validate the ITC enzyme inhibition assay for the determination of the binding constants of the drug-inhibitors to hsPNP. The inverse inhibition constant of 9-benzylguanine determined by the ITC assay is $1.14 \pm 0.09 \times 10^5 \text{ M}^{-1}$ at 58 nM hsPNP (Table 5-5) and this is lower than the $5.24 \pm 0.51 \times 10^5 \text{ M}^{-1}$ for the binding constants of 9-benzylguanine at 50 mM Pi concentration and the higher ITC hsPNP concentrations.

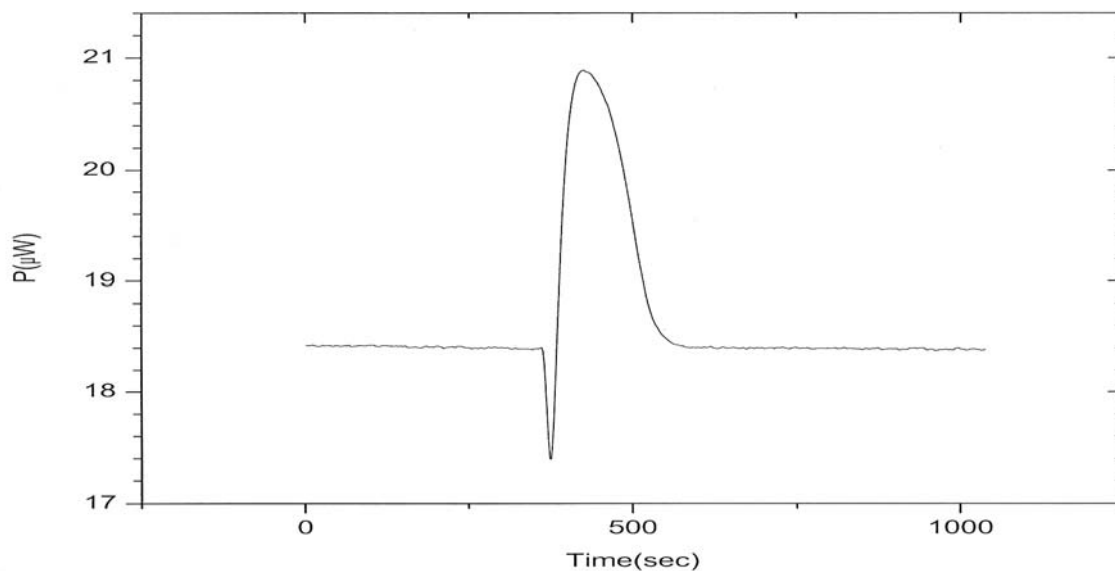


Figure 5-11. An ITC enzyme inhibition assay scan of a 25 μL single injection of 5 mM 7-methylguanosine into 58 nM hsPNP solution and 11.6 μM acyclovir in HEPES buffer, pH 7.0 with 50 mM potassium phosphate, at 25°C.

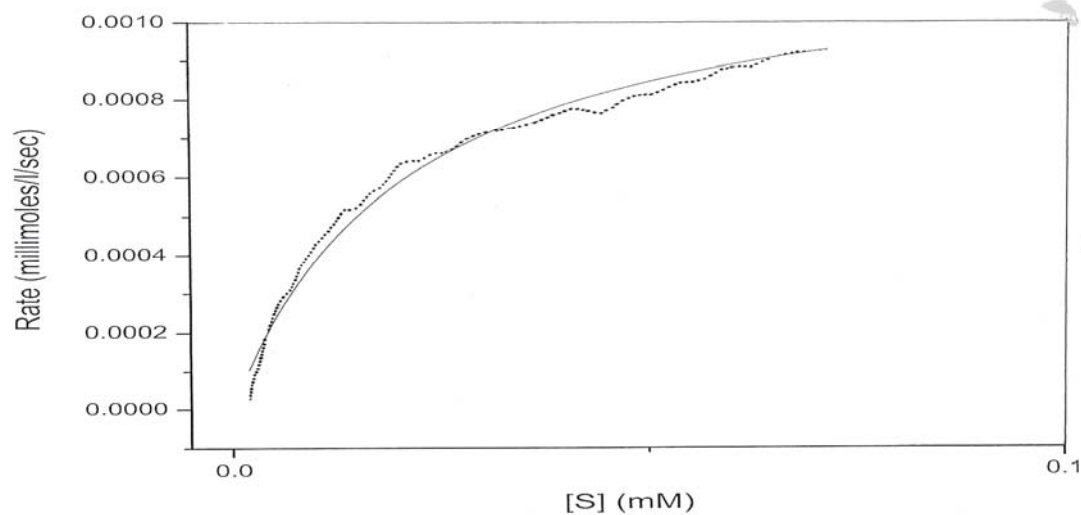


Figure 5-12. A fit of the Michaelis-Menten model (solid line) to the hsPNP enzyme reaction rate in the presence of 11.6 μM acyclovir as a function of the added 7-methylguanosine concentration derived from the ITC data shown in Figure 4-11.

Table 5-5. Enzyme Inhibition constants determined from enzyme kinetic measurements in 100 mM HEPES + 50 mM potassium phosphate buffer at pH =7.0 and 25°C from ITC Measurements

[E] ₀ 10 ⁻⁸ M	[I] 10 ⁻⁵ M	K_i mM	$1/K_i$ 10 ⁵ M ⁻¹
<u>+ Acyclovir</u>			
5.6	1.12	0.0109 ± 0.0016	0.95 ± 0.14
5.7	1.14	0.0111 ± 0.0011	0.92 ± 0.10
5.8	1.16	0.0103 ± 0.00054	0.97 ± 0.05
5.9	1.18	0.0111 ± 0.00038	0.91 ± 0.04
		Average	1/K_i = 0.94 ± 0.03
<u>+ Ganciclovir</u>			
5.4	1.08	0.0096 ± 0.0002	1.04 ± 0.02
5.6	1.12	0.0080 ± 0.0004	1.25 ± 0.05
5.7	1.14	0.0070 ± 0.00024	1.43 ± 0.04
		Average	1/K_i = 1.24 ± 0.20
<u>+9-Benzylguanine</u>			
5.4	1.08	0.00973 ± 0.00038	1.03 ± 0.05
5.6	1.12	0.00808 ± 0.00045	1.26 ± 0.055
5.7	1.14	0.00882 ± 0.00035	1.13 ± 0.040
5.8	1.13	0.00891 ± 0.00065	1.12 ± 0.072
		Average	1/K_i = 1.14 ± 0.09

5.5 Discussion

Although changes in the Pi substrate concentration do not affect the binding affinities of acyclovir, ganciclovir, and 9-benzylguanine to hsPNP, they do affect the nature of the driving force of the drug-inhibitor binding reactions to hsPNP. More specifically with increase in the Pi concentration from 0 to 50 mM Pi concentration, acyclovir binding to hsPNP changes from a 78 ± 5 % to a 23 ± 1 % enthalpically-driven reaction, ganciclovir binding changes from a 31 ± 15 % to a 92 ± 8 % enthalpically-driven reaction, and 9-benzylguanine binding switches from a 100 % to a 42 ± 8 % enthalpically-driven reaction at 10 mM Pi concentration and then reverts back to a 70 ± 8 % enthalpically-driven reaction at 0.1 M Pi concentration. The conversion from an entropically-driven to an enthalpically-driven reaction for ganciclovir binding is also observed in the ITC results on the binding of a phosphonoate derivative of acyclovir to bsPNP, where the $\Delta_b G^\circ$ remains the same, $-34.9 \text{ kJ mol}^{-1}$, but the binding enthalpy of $-11.7 \text{ kJ mol}^{-1}$ (34 % enthalpically-driven reaction) in the absence of Pi decreases to a binding enthalpy of $-25.1 \text{ kJ mol}^{-1}$ (72 % enthalpically-driven reaction) in the presence of 0.35 mM Pi. [116]. Changes in the driving-nature of the binding reactions do not result from any increase in the electrostatic effect by increase in Pi concentration, such as ion release upon drug-inhibitor binding, since changes in the binding enthalpies are not observed for acyclovir and ganciclovir binding with increase from 0.15 to 0.50 M in NaCl concentration in Tables 5-1 and 5-2. Although the binding enthalpies of acyclovir, ganciclovir, and 9-benzylguanine to hsPNP change with change in Pi concentration, their binding affinities to hsPNP remain essentially the same because of entropy-enthalpy

compensation. In entropy-enthalpy compensation, changes in the binding enthalpy are compensated by changes in the binding entropy.

The only differences between acyclovir, ganciclovir, and 9-benzylguanine are differences in their purine N9 side-chains (Fig. 5-2) so that changes in the driving-nature of the drug-inhibitor binding reaction must be related to these differences. Acyclovir has a simple ether side-chain, $-\text{CH}_2\text{-O-CH}_2\text{-CH}_2\text{-OH}$, that is not as bulky as the branched side-chain of ganciclovir, $-\text{CH}_2\text{-O-CH-(CH}_2\text{OH)}_2$, while the side-chain of 9-benzylguanine is a benzyl ring, $-\text{CH}_2\text{-C}_6\text{H}_5$. There is abundant evidence from x-ray crystallography that the purine N9 side chains of the guanine drug-inhibitors interact in different ways with the amino-acid residues of the ribose and Pi binding sites adjacent to the purine binding site in PNP. X-ray crystal structures of acyclovir bound to hsPNP do not exhibit any direct hydrogen-bonding interactions between the side chain and the amino acid residues of the ribose and Pi catalytic pockets of hsPNP [108]. However, X-ray studies of bsPNP complexed with a phosphonate derivative of acyclovir with the more complex side-chain, $-\text{CH}_2\text{-CH(CH}_3\text{)-O-CH}_2\text{-PO}_3$, show interactions between the methyl group on the second carbon and Phe159 of the ribose binding side, as well as a water-bridged interaction between the ether O and Tyr88 of the ribose binding site and interactions between the terminal PO_3 group on the side-chain and Ser33 and Ala116 of the Pi binding site [116]. X-ray crystallographic data on 9-benzylguanine-hsPNP complexes show that the aromatic rings of Phe159 and Phe200 interact with the benzene ring of 9-benzylguanine in the classic herringbone arrangement as reported for many aromatic systems [106]. A water molecule is observed close to Phe159 and Phe200 of the

ribose binding site in X-ray crystallography analysis of pure hsPNP in the absence of phosphate [105].

The functional dependence of the binding entropies of acyclovir and of the binding enthalpies of ganciclovir and 9-benzylguanine on Pi concentration tends to level-off at Pi concentrations above 50 mM. This behavior is indicative of a dependence of the thermodynamic quantities of the binding reaction on the extent of saturation of the adjacent Pi substrate site in hsPNP. Evidence for the effect of bound Pi on the thermodynamics of drug-inhibitor binding to PNP has been observed in enzyme inhibition studies. Enzyme inhibition studies show that decreasing the concentration of Pi from 50 mM to 1 mM increases the binding affinities of the mono, di, and triphosphate esters of acyclovir to hsPNP, as would be expected from competitive binding between Pi and the phosphate ester groups of the acyclovir side chain to the adjacent Pi catalytic binding site [112]. Increases in the binding affinities with decrease in the Pi concentration has also been observed for bulkier 9-side chain derivatives of guanine [123]. X-ray crystallographic analysis of hsPNP-drug-inhibitor complexes show significant displacements of the drug-inhibitors in the catalytic binding site that result from close contacts between the bound drug-inhibitor and a sulfate ion occupying the Pi binding site [124]. An indirect effect of Pi concentration on the drug-inhibitor side chain interaction with the substrate binding sites may also arise from an overall conformational change in the two-substrate binding site induced by bound Pi in hsPNP. A flexible gate of amino acid residues 241-260 that controls access to the catalytic site is formed in the open position upon guanine binding [109]. This loop decreases in flexibility with the extent of Pi binding, as shown by an increase in the fluorescence intensity of Trp249 of

the 241-260 loop of an hsPNP mutant with increasing Pi concentration [110]. More generally, specific Pi binding can affect the binding enthalpy of protein-protein binding interactions. ITC studies of the effect of Pi concentration on the binding enthalpy of the protein-inhibitor turkey ovomucoid third domain binding to serine protease indicated enthalpic contributions to the binding enthalpy from the displacement of water molecules at a specific Pi binding site on the protein-protein product by the Pi [125].

Although it has not been elucidated on the molecular level as to precisely how the extent of saturation of the Pi substrate site changes the driving force of the binding reaction to hsPNP, there can be some speculation as to how interactions of the drug-inhibitor side chains with the substrate binding sites are affected by bound Pi. For example, differences between the binding enthalpies of acyclovir and ganciclovir in the absence of Pi could be explained by an interaction between the ether O of the acyclovir side chain and Tyr88 of the ribose binding site bridged by a water molecule, whereas the bulkier side chain of ganciclovir would inhibit its penetration into the adjacent ribose binding site. Pi binding to the adjacent Pi site would not only displace the bridging water molecule to reduce the acyclovir binding enthalpy, but also induce displacement of the ganciclovir in the purine binding site to facilitate a hydrophobic interaction between its bulky side-chain and the ribose binding site, resulting in an increase in its binding enthalpy. The side chain of 9-benzylguanine would involve displacement of the water molecules at Phe159 in free hsPNP so that the benzyl ring would interact with the aromatic side chain of Phe159 in the absence of Pi, resulting in a high binding enthalpy. Saturation of the adjacent Pi site with Pi would induce displacement of the bound 9-benzylguanine so that its binding enthalpy would be restored following a decrease to a

minimum level at 10 mM Pi concentration. The different dependencies of the experimentally determined binding quantities of acyclovir, ganciclovir and 9-benzylguanine on the extent of saturation of the Pi binding site in Fig. 5-6 would reflect differences in the interactions of the different side-chains with the adjacent ribose and Pi catalytic sites.

The specific activities from values for K_m and k_{cat} determined in the ITC enzymatic assays are in good agreement with their corresponding literature values. In general, the specific activities tend to increase with decrease in the hsPNP concentration from 1.33 μ M to 28.3 nM. Moreover, at 50 mM Pi concentration, the specific enzymatic activity exhibits a more dramatic increase from $41 \pm 3 \mu\text{mol min}^{-1} \text{mg}^{-1}$ at 28.4 nM hsPNP to $139 \pm 10 \mu\text{mol min}^{-1} \text{mg}^{-1}$ at 14.5 nM hsPNP, in contrast to the near-constancy of the specific enzyme activity over this same decrease in hsPNP concentration at 100 mM Pi. An increase in the specific activity of bsPNP with decrease in the bsPNP concentration from 1 μ M to 10 nM at 50 mM Pi is similarly observed using Kalckar's enzyme assay and is attributed to dissociation of the bsPNP to a more active monomer at the lower bsPNP concentration [107]. The gel filtration enzyme activities, as determined by UV spectral changes in the 7-methylguanosine substrate, were, however, only sensitive down to the 60 nM hsPNP concentration and, thus, would not be applicable to the 14–28 nM range of hsPNP concentrations. This increase in the specific activity at the lower 14.5 nM hsPNP level could, thus, indicate some dissociation of the hsPNP trimer into more active enzyme monomers as was observed for bsPNP [107].

Partial dissociation of hsPNP below the 60 nM level would also reduce the contributions of Phe159 and Arg148 from the adjacent subunit to, respectively, the ribose

binding site and a Pi regulatory site. Since X-ray crystallographic data shows that the aromatic ring of Phe159 interacts with the benzene ring of 9-benzylguanine [106], this interaction would be reduced upon partial dissociation of the hsPNP into monomers below 60 nM so that the 9-benzylguanine binding constant is reduced, as is indeed observed, at 54–58 nM hsPNP in Table 5-5. In contrast, the acyclovir and ganciclovir binding constants remain the same at all concentrations of hsPNP, as indicated by the absence of any interaction between these drug-inhibitors and the amino acid residues from the adjacent subunits of hsPNP. Interestingly, the heat of the hsPNP enzyme reaction increases from $2.24 \pm 0.35 \text{ kJ mol}^{-1}$ at 50 mM Pi concentration to $9.57 \pm 0.21 \text{ kJ mol}^{-1}$ at 100 mM Pi concentration. Since changes in the driving-nature of the drug-inhibitor binding reactions show that the catalytic Pi site is nearly saturated at 50 mM, the change in the enzymatic heat of reaction from 50 to 100 mM Pi concentration may result from weak binding of Pi to a secondary regulatory site consisting of Gln44 and Arg148, as inferred from x-ray crystallography results [105]. A much weaker Pi binding constant of 20 M^{-1} for this regulatory site, for example, would increase the extent of Pi saturation of this site from 50 to 67 % and may be partially responsible for the increase in the heat of reaction from 50 to 100 mM Pi concentration. There is very little change in the heat of reaction as the hsPNP concentration is decreased from 1 μM to 10 nM so that the weak binding of Pi to the Pi regulatory site appears to be unaffected by removal of Arg148 of the adjacent subunit. However, it should be emphasized that the Pi concentrations in living cells increase only from 0.4 mM to 6.0 mM [107] so that an increase in the enzymatic heat of reaction from 50 mM to 100 mM Pi concentration is not relevant to drug-inhibitor targeting of the cell. Apparently, the binding affinities/potency of these

simple drug-inhibitors targeting the purine site of hsPNP is not affected by binding of the second substrate P_i to an adjacent site.

Chapter 6: Conclusions

Rational drug design is based on the simultaneous application of computational and experimental strategies to design chemical structures that bind specifically to targeted proteins [2]. The applicability of the theoretically established relationships important for developing efficiently designed drugs for protein targets needs to be validated by measurements under various experimental conditions. In our research project we have emphasized the experimental approach to elucidate the effect of several factors on the energetics of protein-drug interactions. In particular, these include the role of water at the site of interaction, various modifications of the protein target away from the binding site, complexity of the binding site and conformational changes away or at the binding site. The results suggest that the development of effective drugs for protein targets should involve characterization of the factors that influence the energetics of the drug-protein binding reactions. The focus of our research project were three different experimental systems with varying levels of complexity. To begin with, the host/guest interactions between anti-inflammatory drugs and naturally occurring cyclodextrins provide a simplified model system to study protein-drug interactions. Cyclodextrins with their hydrophobic cavity mimic proteins, but unlike real proteins possess rigid, well-defined structures. Therefore, the effects of protein plasticity reflected in conformational changes upon binding of ligands are irrelevant in describing the model of protein-drug interactions. Furthermore, the lack of flexibility of cyclodextrins as protein models allows for studying the effects of various experimental factors, such as salt, ionic strength, temperature on the interactions of drugs with cyclodextrins without considering any conformational change contributions due to “induced fit” events. Moreover, the role

of water in modulating the interactions can be reliably determined and the results used as a foundation in elucidating the more complex water behavior in real protein-drug interactions. The second experimental system involves the interactions between p38 α MAP kinase and drug-inhibitors. The level of complexity is increased by considering the property of structural flexibility common to real proteins. The kinase is a monomer with a single binding site for drug-inhibitors. More interestingly, in contrast to the structurally static cyclodextrins, the domain structure of the kinase allows for elucidating the effect of drug-inhibitor binding on the interdomain interactions through mutagenesis away from the binding site. The third experimental system consists of the more complex oligomer hsPNP interacting with drug-inhibitors. The level of complexity is increased not only by the fact that hsPNP is an active trimer with three independent sites for drug-inhibitor binding but also by the interaction of the protein with an additional substrate necessary for catalysis.

6.1 Binding affinities of drug-protein interactions

The binding affinity for an interaction is dependent on the binding enthalpy and entropy changes reflected in the free energy changes through the fundamental law of thermodynamics:

$$\Delta G^{\circ}(T) = \Delta H^{\circ} - T\Delta S^{\circ} \quad (6.1)$$

The free energy change for a binding reaction at equilibrium is

$$\Delta_b G^{\circ}(T) = -RT \ln \{K_b\} \quad (6.2)$$

where K_b is the binding or equilibrium constant. It is evident from equation (6.2) that the higher the binding constant for the interaction, the more favorable the free energy change

characterizing the binding reaction. The goal of initial drug design is the development of more potent drugs for a target protein to achieve the most energetically favorable drug-protein interaction. The typically adopted strategy is to promote favorable intermolecular interactions between the drug and its target protein in order to optimize the binding affinity of the interaction. This drug design strategy gives desirable results when developing drug-inhibitors against p38 α MAP kinase, as described in chapter 4. The affinity of the drug-inhibitor increases with more intermolecular interactions at the binding site, in particular the binding affinity is in the 10^7M^{-1} range for SB 203580 and SKF 86002 and increases to 10^9M^{-1} range for the larger p38 INH.1 drug-inhibitor, since this inhibitor is designed to interact with an additional hydrophobic pocket on the kinase ([14], see chapter 4, discussion). In the case of drug-inhibitors interacting with hsPNP the binding affinity in the 10^5M^{-1} range is modulated by a small degree with additional interactions within the binding site of a single subunit or by additional interactions with an adjacent subunit, since 9-benzylguanine binds slightly tighter to the enzyme than does acyclovir with a smaller ether side chain ([15], see chapter 5). Another observation is that the specificity of a drug-inhibitor does not depend on the binding affinity alone. Since low binding affinity is usually observed for non-specific binding, such as the binding of ions to a protein, it would be assumed that high binding affinity would indicate high specificity. However, the high affinity drug-inhibitor of p38 α MAP kinase, p38 INH.1, appears to be less specific than the drug-inhibitor SB 203580 with a 2-fold lower binding constant value. This conclusion is based on the observation that the range of binding constants for p38 INH.1 binding to the mutants isoform 1 C162S and isoform 2 C162S at 25°C is about 2.8 fold lower than the 4 fold range observed for

SB 203580 binding to these isoforms at 25°C ([14], see chapter 4). Furthermore, the binding affinity can be modulated by other factors, such as the dissociation of the trimeric hsPNP. Partial dissociation of the oligomer could account for the observed lower K_b value for 9-benzylguanine at low hsPNP concentrations since 9-benzylguanine also interacts with an adjacent subunit at high hsPNP concentrations. The effect of dissociation of the hsPNP trimer to more enzymatically active monomers is further reflected in the observed increase of the specific activity of hsPNP at low nM concentrations ([15], see chapter 5).

Optimization of the binding affinity can be achieved by either favorable binding enthalpy changes as for the drug-inhibitors binding to p38 α MAP kinase or by favorable entropy changes. Drug design strategies are challenged by the so called entropy-enthalpy compensation as implied by equation (6.1) where, frequently, a favorable enthalpy change is compensated by an unfavorable entropy change such that the resulting binding affinities remain unchanged. In the cyclodextrin–drug interactions described in detail in chapter 3, entropy-enthalpy compensation is manifested in the absence of any change in the binding affinities of NPX interacting with β -cyclodextrin and γ -cyclodextrin, as well as the constancy within experimental error of the binding affinity of FLP and NAB interacting with β -cyclodextrin ([13], see chapter 3). Furthermore, there is evidence for enthalpy-entropy compensation in the interaction of acyclovir and ganciclovir with hsPNP, since their binding affinities remain the same within experimental error as a function of the second substrate P_i concentration, although the P_i concentration does affect the driving-nature of the binding reaction. Therefore, the enthalpy and entropy

changes upon binding as well as their effect on the free energy change for the interaction are important considerations for the development of drug design strategies.

6.2 The importance of determining the driving-nature of the binding reaction

It is important to determine whether a drug binding reaction is enthalpically-driven or entropically-driven. This can be seen where the driving-nature of the binding reaction is influenced by the properties of the binding site, such as its size as in the cyclodextrins, its location with respect to the domain arrangement of the protein in the case of the distinct N-and C-terminus domains of p38 α MAP kinase, its proximity to the subunit interface of the trimeric hsPNP, and the presence of an adjacent binding site for the phosphate substrate in hsPNP. For example, the binding reactions of NSAIDs to β -cyclodextrin with a smaller hydrophobic cavity are enthalpically driven, whereas the binding reactions to γ -cyclodextrin with a 40 vol% bigger cavity are entropically driven. Furthermore, the structural properties of the individual drugs determine the specific interactions with the protein binding site, thus influencing the driving force of the binding reaction. The enthalpic nature of the binding is favored by formation of more van der Waals contacts between the drug and the β -cyclodextrin cavity ([13], see chapter 3). The binding reactions of drug-inhibitors to wild type and mutant p38 α MAP kinases are enthalpically-driven with various interactions favorably contributing to the enthalpic nature of the binding reaction such as the formation of additional hydrogen bonds, hydrophobic interactions, and van der Waals interactions. The structural properties of the individual drugs determine the specific interactions with the hsPNP binding site, thus influencing the driving force of the binding reaction in the absence of phosphate.

Specifically, the drug-inhibitors differ in the bulkiness and the nature of their N9-side chains and form less or more interactions with amino acid residues within a single subunit or also interactions with the adjacent second substrate binding site and with the adjacent subunit of the hsPNP trimer ([15], see chapter 5). Interestingly, in the case of drug-inhibitors binding to hsPNP the binding enthalpy or entropy changes are influenced by the concentration of the second substrate for the enzyme, inorganic phosphate. The phosphate effect on the drug-inhibitor–hsPNP interactions could be explained considering a combination of factors. Increasing the phosphate concentration affects a conformational change accompanying the enzymatic reaction by causing a decrease in the flexibility of the loop involved in the conformational change. As a result, the enthalpic nature of the binding reaction is reduced by the unfavorable contributions reflected in the enthalpy of the conformational change. Increasing phosphate concentrations also leads to the displacement of a bridging water molecule contributing to the acyclovir-hsPNP interaction and this results in reducing the binding enthalpy. In addition, binding of the phosphate promotes hydrophobic interactions resulting in increase of the binding enthalpy for the ganciclovir–hsPNP interaction. Changes in the heat of the enzymatic reaction catalyzed by hsPNP could be attributed to an additional effect of phosphate. More specifically, weak binding of phosphate to an additional regulatory site other than the catalytic phosphate site could be responsible for the observed increase in the enzymatic heat of reaction ([15], see chapter 5). Dependence of the enthalpy and the entropy change on temperature is reflected in a different thermodynamic parameter, the binding heat capacity change.

6.3 Heat capacity changes favoring or hindering drug-protein interactions

A major source of heat capacity changes accompanying a drug-protein interaction is the hydrophobic effect. The general nature of the hydrophobic effect is reflected in the formation of cages of structured water of abnormally high heat capacity and low entropy around nonpolar groups [52]. As the hydrophobic drug gets excluded from the aqueous environment as it interacts with the protein binding pocket the cages of structured water around the nonpolar solute are disrupted. As a result, disorder in the water structure is induced and the heat capacity of the system decreases implying a negative heat capacity change. On the other hand, introducing hydrophobic clusters in the polar water environment induces an ordering of the water structure as it forms cages around the nonpolar groups and this results in a positive heat capacity change. This is the case of unfolding of proteins. The tight fits of NSAIDs in the smaller β -cyclodextrin cavity result from the reorganization of the bulk water structure when the drug leaves the bulk water environment to bind in the hydrophobic cavity of the β -cyclodextrin cavity with little water retained in the cavity. This results in a more negative heat capacity change. Alternatively, less negative or zero heat capacity changes describe the binding of NSAIDs within the larger γ -cyclodextrin cavity. In this case, the larger γ -cyclodextrin cavity allows for retention of more water upon drug binding and little bulk water structure reorganization occurs ([13], see chapter 3, discussion).

Negative or positive heat capacity changes can reflect differences in the structural stability of the target protein upon drug binding. For example, the binding of drug-inhibitors to the native p38 α MAP kinase isoform 1 and to the C162S mutants of both isoforms results in negative heat capacity changes. On the other hand, positive and

close to zero heat capacity changes characterize drug-inhibitor binding to the native p38 α MAP kinase main isoform. Positive or close to zero heat capacity changes could imply that the drug-inhibitor binding produces an increase in other contributions, for example, in the vibrational contributions to the heat capacity change that can compensate for the hydrophobic effect [52].

6.4 The role of water in the energetics of drug-protein interactions

The entropic contribution to the drug binding affinity of the release of water molecules from the protein-drug binding interface should be incorporated as an important component of drug design strategies [5]. The effect of water proves to be very pronounced in affecting the driving-nature of the drug-inhibitor-cyclodextrin interactions. The water environment near hydrophobic cavities, such as those of the cyclodextrins, is composed of two distinct regions of water molecules, the regions that are typical of the bulk liquid, where most molecules form four hydrogen bonds and the regions typically near the hydrophobic interface that form three or fewer hydrogen bonds [126]. Binding of drugs to the larger 40 vol % γ -cyclodextrin hydrophobic cavity is characterized by little reorganization of the bulk water structure with retention of water in the γ -cyclodextrin cavity. This results in “looseness” of the drug fits in the γ -cyclodextrin cavity causing a decrease in the van der Waals interactions and, thus, a decrease in the binding enthalpy contribution ([13], see chapter 3, discussion). On the other hand, the increase of the entropic component characterizing the binding of drugs to γ -cyclodextrin could be attributed to the “loose” drug fits in terms of higher configurational entropic contributions, ΔS_{conf} , to $\Delta_b S_{\text{exp}}$ ([13], see chapter 3, equation 3.6). Accordingly, the drug

binding reactions to γ -cyclodextrin become mainly entropically-driven. Verification of the presence of water in the cyclodextrin binding sites was found by the effect of water on the fluorescence intensities of the NSAIDs in the binding sites. The fluorescence intensities of the drugs in aqueous environments are enhanced relative to their intensities in hydrophobic environments. The incomplete fluorescence enhancement of FLP at the saturation binding limit within β -cyclodextrin compared to its complete fluorescence enhancement in the hydrophobic environment of isopropanol suggests partial retention of individual water molecules at the drug interface in the β -cyclodextrin cavity ([13], see chapter 3). The retention of localized water molecules may also contribute favorably to the binding enthalpy, as observed previously for lysozyme antigen-antibody binding [66]. In enthalpy-entropy compensation, there is an entropic penalty of trapping a water molecule on the binding interface and restricting its degrees of freedom and a compensatory enthalpic gain from the formation of new hydrogen bond network by water directly interacting with residues of the binding site or by water mediating the drug-protein interaction [67]. Furthermore, the displacement of a bridging water molecule contributing to the acyclovir-hsPNP interaction in the presence of phosphate could explain the observed reduction of the binding enthalpy ([15], see chapter 5, discussion).

6.5 Importance of correlating thermodynamic and structural data in characterizing drug-protein interactions

From X-ray crystal structure studies on binding of drug-inhibitors to p38 α MAP kinase it is evident that the binding interaction is characterized by ordered water molecules creating a hydrogen bond network at the binding interface with no direct

interactions with the bound ligand [79, 90]. These additional water-mediated hydrogen bonds contribute favorably to the enthalpy change of the binding reaction, and this contribution is reflected in the enthalpic nature of the binding reactions between the drug-inhibitors and p38 α MAP kinase. Furthermore, the correlation of the obtained DSC experimental data on SB 203580 and p38 INH.1 binding to the kinase with structural information on the protein alone or in complex with drug-inhibitors helped us to assign each of the two observed unfolding transitions to a particular protein domain, N- or C-terminal domain. Correlation between the DSC obtained transition temperatures, T_m 's with the structure of p38 α MAP kinase helps to conclude that there is little drug binding effect on the unfolding of the non-interacting with the drug C-terminal domain. In addition, the differences in the sequence of the p38 α MAP kinase splice variants, in particular within a twenty-five-amino-acid region in the C-terminus as shown in Fig. 4-3 is reflected in the T_m values of the unfolding transition for the proteins and therefore, in the energetic protein stability. Moreover, the conformational stability of the domain structure of p38 α MAP kinase may be related further to other important data on the protein properties, such as the enzymatic activity of the mutated versus the native protein.

Furthermore, the comparison between the available X-ray crystal structures of hsPNP alone and in complex with acyclovir show a conformational change reflected in the flexibility of a surface loop [105, 108]. This conformational change may affect the driving-nature of the binding reactions as determined from ITC experiments. The reduction of the K_b for 9-benzylguanine at dilute hsPNP concentrations could be explained by the available structural data on the specific amino acid interactions between adjacent hsPNP subunits, specifically their interactions with the side chain of 9-

benzylguanine and the loss of these interactions upon dissociation of the enzyme at low concentrations. The close proximity of the purine and phosphate binding sites, as observed in the crystal structure, can explain the observed effects of the different side chains of the drug-inhibitors on the driving-nature of the binding reaction as measure by ITC.

In conclusion, our research project presents a study on systems of varying complexities from the simple cyclodextrin–NSAIDs interactions as model for protein-drug interactions, through the more flexible and mutated p38 α MAP kinase interacting with drug-inhibitors, to the multiple binding sites of the multi-substrate hsPNP. The specific experimental results and determined relationships can be discussed in the light of fundamental parameters governing drug-protein interactions. Therefore, their incorporation in a computational database can prove useful for the development of more efficient drug design strategies.

Appendices

Appendix A - UV-Vis Spectrophotometry

Absorption spectroscopy characterizes the transitions of molecules from a ground to an excited state. Each molecule can be regarded as composed of electronic states consisting of different vibrational and rotational levels. Absorption is the event of a molecule transitioning from its ground electronic state to any vibrational level of its excited electronic state. The lifetime of absorption events is on the order of 10^{-15} seconds, whereas the transitions between the vibrational levels are on the order of 10^{-12} seconds. Since absorption is a very fast process, it is possible to monitor the electronic transitions of molecules without any loss of energy occurring due to slower vibrational transitions within the excited electronic state. UV-Vis spectroscopy monitors the electronic transitions of molecules, since the required energy for these transitions is found in the visible and ultraviolet (UV) spectra of light, in the range 10^2 - 10^3 nm. In general, during a single measurement the sample to be studied is placed in a cuvette and light coming from a light source hits the sample. Some of the incident light is absorbed by the sample and the transmitted light intensity in the UV-visible region of the light spectrum is read by a detector. The instrument measures the intensity of the transmitted light I and compares it to the intensity of the incident light I_0 , expressed as the ratio I/I_0 in percentage, referred to as the % transmittance, %T. It is found experimentally that transmittance is proportional to the concentration of the absorbing species and the path length of the light through the sample and this relationship is given by the Beer-Lambert law:

$$\log T = -\epsilon \times c \times l \quad (\text{A.1})$$

where c is the concentration of the sample, l is the path length and ϵ is the molar extinction coefficient, also referred to as the molar absorptivity. The extinction coefficient depends on the frequency of the incident light and is proportional to the square of the transition dipole moment [127]. It is commonly reported in units of $\text{Lmol}^{-1} \text{cm}^{-1}$. Though the Beer-Lambert law is empirical, it can be understood considering that the intensity of absorption is proportional to the light intensity inside the sample [127]. The sample in the cuvette can be viewed as composed of a stack of infinitesimal slices or layers with thickness dx . The change in intensity, dI , when light passes through one particular slice is proportional to the thickness of the layer, dx , the concentration of the absorbing species, c , and the intensity of the incident light hitting the layer, I . Considering that dI is negative, since the light intensity is reduced by absorption, the expression for dI becomes:

$$dI = -\epsilon c I dx \quad (\text{A.2a})$$

so that

$$dI/I = -\epsilon c dx \quad (\text{A.2b})$$

an expression which applies to each layer. The light intensity after it passes through a sample with thickness l is from integration of the above expression,

$$\ln(I/I_0) = -\epsilon c l. \quad (\text{A.2c})$$

This expression shows that the transmitted light intensity decreases exponentially with the length of the sample [127]. Substituting $\log(I/I_0)$ with the dimensionless quantity A known as the absorbance or optical density(OD) of the sample yields:

$$A = \epsilon c l. \quad (\text{A.2f})$$

Throughout our research we have used a double-beam Perkin-Elmer Lambda 4 UV-Vis spectrophotometer, where the absorbance of a sample is compared to the absorbance of a reference to correct for any solvent effects. The concentrations of all the drug-inhibitors, NSAIDs, CSAIDs and hsPNP drug-inhibitors were determined from UV absorbance measurements since since they all have various aromatic ring systems that absorb in the 200 to 350 nm region of the spectrum. The concentrations of the p38 α MAP kinases and hsPNP were also determined from absorbance measurements of their tyoasine and tryptophan aromatic amino acid residues.

Appendix B - HPLC analysis of FLP, NPX, NAB, and 9-benzylguanine

The main applications of High Pressure Liquid Chromatography (HPLC) are the separation, identification and quantification of compounds. The basis of the technique is the separation of components of non-volatile samples (solutes) due to the different migration rates of the components through a stationary phase by a liquid mobile phase (the elutant). The physical parameter that indicates the distribution of solutes between the stationary phase and the elutant is called the distribution or partition coefficient. The equilibrium partition coefficient (K) is defined as the ratio of the molar concentrations of the solute in the stationary and mobile phase:

$$K = C_s/C_m \quad (B.1)$$

where C_s and C_m are the concentrations of the solute in the stationary and mobile phases, respectively. Therefore, the separation of different solutes through HPLC depends on their different equilibrium partition coefficients. Migration of solutes through the

stationary phase occurs only when they are in the mobile phase and therefore solutes with high K values elute more slowly than solutes with low K values.

In HPLC, the sample to be investigated is injected onto a column that holds chromatographic packaging material (the stationary phase), while a solvent (the mobile phase) is pumped through the column and the partition coefficient of the analyzed sample depends on its specific chemical or physical interactions with the stationary phase. The composition of the solvent used as a mobile phase also affects the partition coefficient of the studied sample and therefore the degree of its retention on the column and the time for the sample to come out at the end of the column. The polarity of the used solvent can be varied for single experiments or even during a single experiment by mixing different solvents during running of the HPLC and this is known as gradient elution. Depending on the polarity of the stationary and the mobile phase, HPLC can be classified as normal phase or reversed phase. In particular, for the analysis of the purity and identification of NSAIDs and one of the hsPNP inhibitors, 9-benzylguanine we used reversed phase HPLC. Reversed phase HPLC is characterized by a non-polar stationary phase and an aqueous, moderately polar mobile phase. For our purposes, we used an C₁₈ column, with straight chain alkyl group composed of 18 carbons for the stationary phase and a mixture of 70%:30% methyl alcohol:water for the mobile phase. In this case the retention time is longer for more non-polar compounds and more polar compounds elute faster. Prior to analysis, the proper performance of the column was checked by running a uracil and naphthalene solution mixture where the uracil would elute faster than the naphthalene, as suggested by the manufacturer, Waters Corporation, MA. Each of the analyzed compounds was diluted in the methanol/water mixture, loaded into a 20 µL sample loop

and then manually injecting the contents of the loop into the column. The collected data consisted of the UV absorbance peaks of the sample as a function of time since UV detection was employed as the detector.

Appendix C - Circular Dichroism Measurements

Dichroism is the phenomenon that describes the variation of light absorption with different directions of polarized light. In circularly polarized light, the electric vector component is constant in magnitude, but varies in orientation and, thus, is described as either a right- or left-handed helical vector [128]. Circular Dichroism (CD) is based on the differences in the absorption of the left and right circularly polarized light [129, 128]. A CD absorption peak results from the optical activity of asymmetric molecules, since the area under a CD band is related to the rotational strength of the molecule. In symmetric molecules, the magnetic and the electric transition dipoles are perpendicular resulting in the absence of rotational strength and no CD peak [128]. In biopolymers, even though the absorbing moieties are symmetric exhibiting no CD, CD bands arise because of the interactions between their transition dipoles and transition dipoles in other parts of the molecule. Therefore, characterizing the interactions between transition dipoles by CD would yield information about the biopolymer structure [128]. Furthermore, CD occurs only at energies where normal UV absorption occurs with the CD bands being either positive or negative, unlike UV absorption bands. The CD instrument, called a spectropolarimeter has a setup similar to a normal absorption instrument with an additional optical element, a polarizer, to produce the polarized incident light [128, 129]. For practical purposes the absorbance of the solution subjected

to CD should not exceed 1.0. As for UV-Vis spectroscopy described in appendix A, the validity of the Beer-Lambert Law also holds for CD measurements. CD is expressed in terms of absorbance as the difference in extinction coefficients between left- and right-handed circularly polarized light:

$$\Delta\epsilon = \epsilon_L - \epsilon_R \quad (\text{C.1})$$

multiplied by the concentration c and the path length l :

$$\Delta A = \Delta\epsilon \times l \times c. \quad (\text{C.2})$$

The raw CD output in ΔA as a function of wavelength in nm can be converted to units of ellipticity θ in degrees following the relationship:

$$\Delta A = \theta / 32.98 \quad (\text{C.3})$$

which can be further converted to molar ellipticity in $\text{deg} \cdot \text{cm}^2 \cdot \text{dmol}^{-1}$:

$$\Delta\epsilon = [\theta] / 3298. \quad (\text{C.4})$$

CD peaks in biopolymers, ie. proteins, arises from the interaction between the transition dipoles of left and right circular polarized light and therefore, the technique is extremely sensitive to the conformation of the biopolymer. In the far UV region (240-180 nm), which corresponds to peptide bond absorption, the CD measurements give information about the secondary structure of proteins [129]. The major chromophore in proteins is the amide group and the band corresponding to the amide $\pi \rightarrow \pi^*$ transition appears at 195 nm. Typical bands appear for the secondary structure elements, α -helices and β -strands. For example, for an α -helix, a characteristic negative band appears at about 222 nm due to the $\pi \rightarrow \pi^*$ transition and also a negative and positive couplet at about 208 nm and 190 nm due to the parallel and perpendicular components of the $\pi \rightarrow \pi^*$ transition, respectively. For a β -strand, the CD profile is characterized by the appearance of two

bands, a negative one at about 215 nm and a positive one at about 198 nm [128]. The positions and the intensities of the characteristic bands for a native protein vary considerably depending on the amount of its component secondary structure. Changes in secondary structure often involve changes in the α -helical content with the largest change occurring at 220 nm and therefore, the CD signal at this wavelength is often used to monitor changes in secondary structure. In addition, in the near UV region (320-260 nm) CD bands arise from changes in the environments of the aromatic amino acid side chains and thus CD spectra can give information about the tertiary structure of proteins [129]. Furthermore, CD spectroscopy is useful for monitoring changes in the protein conformation due to melting, solvent change, binding of ligands or any other variation [128].

It has been suggested from crystal structure studies that upon binding of acyclovir in the active site of hsPNP there is a change in protein conformation, which leads to the adoption of helical conformation by amino acid residues 257-265 [108]. Therefore, we wanted to check for any observable CD effects of binding of the drug-inhibitor acyclovir to hsPNP on the secondary structure of hsPNP. The experiments were carried out at 25°C with hsPNP dialyzed in 10 mM sodium phosphate buffer, pH 7.4 and acyclovir solution prepared in the dialysate buffer. The amount and concentration requirements for the sample depended on the path length of the cuvette used for the CD measurements. If the cuvette width is 1 cm, the amount and the concentration of the sample should be 1 mL and 25 mg/mL, respectively, whereas if the cuvette length is 0.1 cm, the corresponding amount and concentration of the sample should be 0.3 mL and 250 mg/mL, respectively. For my particular set of experiments I used a 1 cm cuvette with hsPNP concentration of

0.781 μM and acyclovir concentration of 4.91 μM . The CD spectrum of each solution separately was measured, as well as that of the complex solution between acyclovir and hsPNP. The CD spectrum of the acyclovir solution alone was determined as a control to check for any artifact contribution of the inhibitor solution. After comparison of the CD spectrum for the protein alone and the one for the protein-drug-inhibitor complex, no change was observed at 220 nm, the typical wavelength for the detection of any change in the secondary structure of proteins. The overlayed CD spectra of the protein alone as well as the protein-inhibitor complex is displayed on Fig. C-1 below.

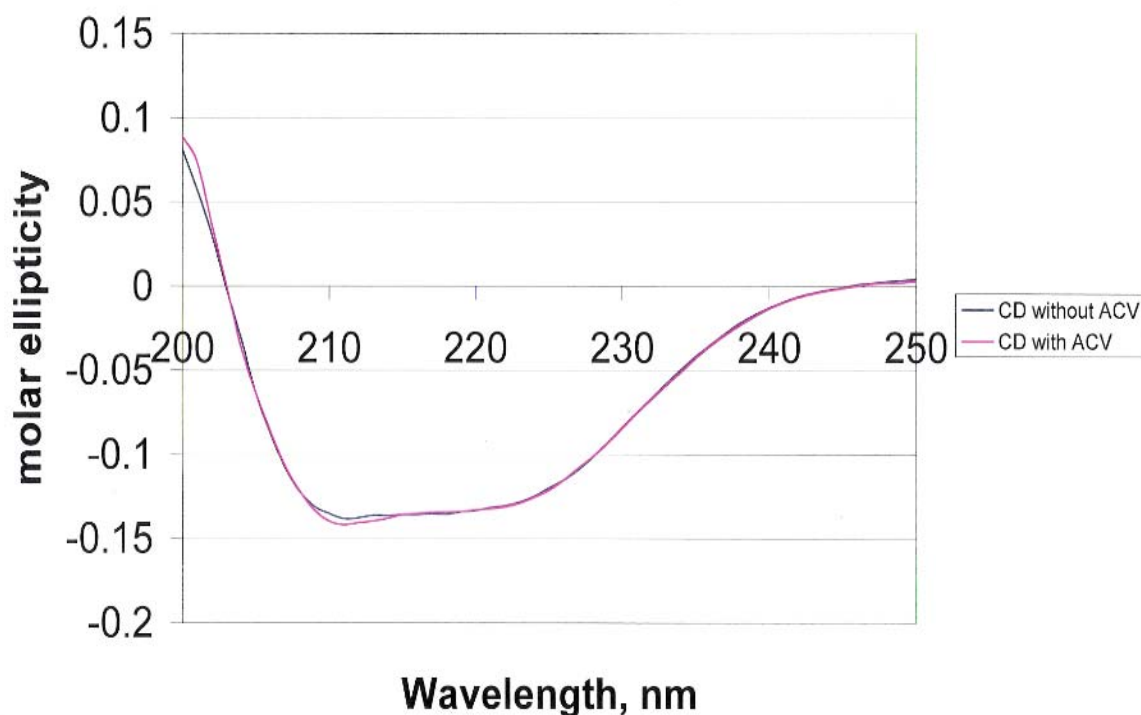


Figure C-1. Overlayed CD of hsPNP alone and in complex with acyclovir.

Appendix D- Size-exclusion chromatography

Size exclusion chromatography is used for the determination of the oligomerization of proteins in solution as well as for analysis of ligand binding on the oligomeric state of proteins. The basis of the technique is separation of proteins according to their size, or hydrodynamic radius. The main components as with HPLC are the stationary phase and the mobile phase. The aqueous mobile phase is pumped through the stationary phase, a column tightly packed with small porous polymer beads with pores of different sizes, which can either be depressions on the bead surface, or channels through the bead. Since the larger particles cannot enter into as many of the smaller pores, they will elute faster than the smaller particles whose elution would be slowed down because of interaction within more of the pores. Similarly to HPLC described in appendix B, the best characteristic of the elution of the sample is the so called partition coefficient:

$$K_{av} = (V_e - V_0)/(V_t - V_0) \quad (D.1)$$

Where V_e is the elution volume of the sample, V_0 is the so-called void volume, which is the elution volume of those molecules too large to enter the matrix pores so that they pass straight through the packed bed, and V_t is the total volume of the packed bed [130]. K_{av} is a measure of the elution behavior of samples and is independent of column dimension and packing. Furthermore, the partition coefficient K_{av} is related to the molecular weight (M_r) of the sample, so that the relationship between K_{av} and the logarithm of the sample M_r is sigmoidal for molecules with similar shape and density [130]. The M_r of the analyzed protein can be determined from a standard curve, constructed by plotting the logarithms of known molecular weights of standard protein samples versus their experimentally determined elution volumes. Columns with different separation ranges

consisting of different pore sizes can be used for the separation of proteins with different M_r values. Moreover, columns differ not only on their pore size but also on the properties of their packaging material referred to as gel filtration medium. For example, Superdex as a gel filtration medium was used for our measurements presented in chapter 5 since its properties allow for high resolution fractionation combined with short run times and good recovery.

It is important to note that for accurate determination of molecular weights the standard proteins used for calibration of the column should exhibit the same relationship between M_r and size as the analyzed sample [130]. Otherwise, the constructed calibration curve cannot be used reliably for extrapolation in order to determine the M_r of the analyzed sample. Bearing this in mind, in chapter 5 we have utilized size-exclusion chromatography only to detect any evidence of dissociation of hsPNP, without being concerned with the exact determination of the molecular weight of the protein. For more reliable determination of the molecular weight of hsPNP we have utilized static light scattering.

Appendix E- Static light scattering

Static light scattering is a technique used for the determination of molecular weights of proteins and their complexes in solution and for monitoring protein oligomerization in solution. The use of static light scattering has also recently been reported in the characterization of the stoichiometry of a protein-protein complex, in particular the association between the human tumor necrosis factor- α (TNF- α) trimer and the extracellular domain of the TNF type 1 receptor, or two glycoprotein-protein

interactions [131]. The basis of the light scattering technique is to improve the sensitivity of size-exclusion chromatography (SEC) technique (see appendix D) by coupling SEC with laser light scattering, refractive index, and UV detection [131].

The method is based on the proportionality between the amount of scattered light and the size of the product in terms of its weight-average molecular weight (MW, molar mass) and its concentration (c in g/mL):

$$LS \sim MW \cdot c. \quad (E.1)$$

The relationship between the excess scattered light and MW follows:

$$(K \cdot c)/R(\theta) = (1/(MW \cdot P(\theta))) + 2A_2c \quad (E.2)$$

where $R(\theta)$ is the excess intensity of scattered light measured at angle θ , $P(\theta)$ describes the angular distribution of the scattered light, and K^* is a function of the refractive index of the solvent, the measured refractive index, and the wavelength of the incident light [132]. Since relatively low concentrations (usually $< 0.1 \text{ mg/mL}$) are used with the technique, the term $2A_2c$ can be neglected. Furthermore, there are several fitting methods for the analysis of the light scattering profile in order to determine MW of the sample of interest. The fitting procedure we have used for the static light scattering measurements described in chapter 5 is the Zimm fitting method. This method is based on constructing a plot of $K \cdot c/R(\theta)$ against $\sin^2(\theta)$ and fitting a polynomial to the data, thereby obtaining the MW from the intercept of the plot at zero angle [132].

The two major advantages of static light scattering are that it is a fast and accurate for protein MW measurements. For example, the advantage of light scattering over SEC is that the measured MW is independent of the elution time and of any effects of sample

interaction with the size-exclusion column. The determination of MW depends only on the light scattering (LS) and refractive index (RI) detectors [132].

Appendix F - Derivation of equation used for analyzing fluorescence data

The general reaction expression for the cyclodextrin-drug interaction is:



If $[CD \cdot D] = x$, $[CD]_0$ and $[D]_0$ are, respectively, the initial concentrations of cyclodextrin and drug, then the binding constant, K_b for the interaction is:

$$K_b = [x]/([CD]_0 - x)[D]_0 - x). \quad (F.2a)$$

Which becomes the following quadratic equation:

$$[x]^2 - (1/K_b + [CD]_0 + [D]_0)[x] + [CD]_0[D]_0 = 0 \quad (F.2b)$$

of the general form

$$a \cdot x^2 + b \cdot x + c = 0 \quad (F.2c)$$

with solutions

$$x = \{-b \pm (b^2 - 4 \cdot a \cdot c)^{1/2}\} / 2 \cdot a \quad (F.2d)$$

where, $a = 1$, $b = -(1/K_b + [CD]_0 + [D]_0)$ and $c = [CD]_0[D]_0$.

so that,

$$x = \{(1/K_b + [CD]_0 + [D]_0) - ((1/K_b + [CD]_0 + [D]_0)^2 - 4 \cdot [CD]_0[D]_0)^{1/2}\} / 2 \quad (F.2e)$$

From the experimental fluorescence intensity measurements

$$F([CD]) = (1 - x(F))F_0 + x(F)F_f([CD]) \quad (F.3a)$$

where $F([CD])$ is the increase in the drug fluorescence intensity upon addition of

cyclodextrin, $x(F)$ is the fractional increase of the bound drug, F_0 is the initial drug

fluorescence intensity in the absence of cyclodextrin and $F_f([CD])$ is the maximum drug

fluorescence intensity in the presence of saturating amount of cyclodextrin. Therefore, solving for $x(F)$ gives the expression:

$$x(F) = (F([CD]) - F_0)/(F_f([CD]) - F_0) \quad (F.3b)$$

or

$$x(F) = \Delta F/\Delta F_{\max} \quad (F.3c)$$

where ΔF is the change in drug fluorescence intensity upon addition of cyclodextrin and ΔF_{\max} is the maximum drug fluorescence intensity change at saturating cyclodextrin concentrations.

Since $\Delta F \sim [CD \cdot D]$ and at saturation, $\Delta F = \Delta F_{\max}$, $[CD \cdot D] = [D]_0$, the assumption is made that

$$\Delta F/\Delta F_{\max} = [CD \cdot D]/[D]_0. \quad (F.3d)$$

Therefore, the final expression (F.3e) for the relationship between $x(F)$ and K_b becomes:

$$x(F) = \{ (1/K_b + [CD]_0 + [D]_0) - ((1/K_b + [CD]_0 + [D]_0)^2 - 4*[CD]_0*[D]_0)^{1/2} \} / 2*[D]_0.$$

Appendix G- Determination of K_b from the shift in the transition temperature induced by binding of the drug in the folded state of the protein and temperature shift calculations from DSC experiments

The general van't Hoff equation for equilibrium processes as a function of temperature is

$$d \ln K_{eq} / d(1/T) = -\Delta H(T) / R. \quad (G.1a)$$

where $\Delta H(T)$ is the temperature dependent enthalpy change for the process. For a binding reaction K_{eq} becomes K_b and $\Delta H(T)$ becomes the binding enthalpy change, $\Delta H_b(T)$. Integration of equation (G.1a) from a known temperature T to the denaturation

temperature T_G of the protein yields,

$$\ln[K_b(T_G)/K_b(T)] = [(-\Delta H(T) + \Delta C_p * T)/R]*(1/T_G - 1/T) + (\Delta C_p/R)*\ln(T_G/T) \quad (G.1b)$$

Assuming that the unfolding of a protein is a two-state transition,



where F is the folded state and U is the unfolded state. In the absence of ligand and at the transition temperature,

$$\Delta_{trs}G^0 = 0 = \Delta_{trs}H^0 - T_G \Delta_{trs}S^0 \quad (G.2)$$

In the presence of ligand bound to the folded state of the protein, there is a small stabilization of the folded state so that at the new denaturation temperature, T_G'

$$\Delta_{trs}G(T_G') = \Delta_{trs}H - T_G' \Delta_{trs}S - RT_G' \ln(1 + K_b[L_f]) = 0 \quad (G.3)$$

where $[L_f]$ is the concentration of the free ligand in the sample. After simplifying, rearranging and substituting $\Delta_{trs}S^0$ with $\Delta_{trs}H^0/T_G$ from Equation (G.2) into Equation (G.3) based on the assumption that $\Delta_{trs}S^0$ with $\Delta_{trs}H^0$ do not change with the slight increase in the denaturation temperature of the ligand-protein complex [133].

$$1/T_G' - 1/T_G = (R/\Delta_{trs}H^0) \ln(1 + K_b[L_f]). \quad (G.4)$$

Since $[L_f]$ is not know, the free drug-inhibitor concentration can be approximated by:

$I \sim I_0 - P_0/2$, where I_0 is the initial drug-inhibitor concentration greater than the initial protein concentration, P_0 , and at the denaturation temperature the native protein concentration is half of the initial protein concentration [39]. Therefore, equation (G.4) becomes:

$$1/T_G' - 1/T_G = (R/\Delta_{trs}H^0) \ln.\{1 + ([I_0] - [P_0]/2)*K_b\} \quad (G.5)$$

which is the same as equation (4.3) in the experimental section of chapter 4.

Bibliography

1. Dror, O., et al., *Predicting molecular interactions in silico: I. A guide to pharmacophore identification and its applications to drug design*. Curr Med Chem, 2004. **11**(1): p. 71-90.
2. Schneidman-Duhovny, D., R. Nussinov, and H.J. Wolfson, *Predicting molecular interactions in silico: II. Protein-protein and protein-drug docking*. Curr Med Chem, 2004. **11**(1): p. 91-107.
3. Warren, G.L., et al., *A critical assessment of docking programs and scoring functions*. J Med Chem, 2006. **49**(20): p. 5912-31.
4. Minai, R., et al., *Method for comparing the structures of protein ligand-binding sites and application for predicting protein-drug interactions*. Proteins, 2008. **72**(1): p. 367-81.
5. Hamelberg, D. and J.A. McCammon, *Standard free energy of releasing a localized water molecule from the binding pockets of proteins: double-decoupling method*. J Am Chem Soc, 2004. **126**(24): p. 7683-9.
6. Atkins, P. and J. de Paula, *Physical Chemistry*, Seventh edition, W.H. Freeman and Company, New York, 2002.
7. Crespo, A. and A. Fernandez, *Induced disorder in protein-ligand complexes as a drug-design strategy*. Mol Pharm, 2008. **5**(3): p. 430-7.
8. Whitesides, G.M. and V.M. Krishnamurthy, *Designing ligands to bind proteins*. Q Rev Biophys, 2005. **38**(4): p. 385-95.
9. Creighton, T.E., *Proteins. Structures and Molecular Properties*, Second edition, W.H. Freeman and Company, New York, 1993.
10. Lohman, T.M. and D.P. Mascotti, *Thermodynamics of ligand-nucleic acid interactions*. Methods Enzymol, 1992. **212**: p. 400-24.

11. DeLauder, S., et al., *Thermodynamic analysis of heparin binding to human antithrombin*. Biochim Biophys Acta, 1992. **1159**(2): p. 141-9.
12. Privalov, P.L., et al., *What drives proteins into the major or minor grooves of DNA?* J Mol Biol, 2007. **365**(1): p. 1-9.
13. Todorova, N.A. and F.P. Schwarz, *The role of water in the thermodynamics of drug binding to cyclodextrin*. J Chem Thermodynamics, 2007. **39**: p. 1038-48.
14. Todorova, N.A., et al., *Effect of the distal C162S mutation on the energetics of drug binding to p38 α MAP kinase*. Arch Biochem Biophys, 2008. **469**(2): p. 232-42.
15. Todorova, N.A. and F.P. Schwarz, *Effect of the phosphate substrate on drug-inhibitor binding to human purine nucleoside phosphorylase*. Arch Biochem Biophys, in press.
16. Schwarz, F. P., T. Reinisch, H.J. Hinz, and A. Surolia, *Recommendations on measurements and analysis of results obtained on biological substances using isothermal titration calorimetry*. Pure Appl Chem, 2008. **80**: p. 2025-40.
17. Velazquez-Campoy, A., S. Vega, and E. Freire, *Amplification of the effects of drug resistance mutations by background polymorphisms in HIV-1 protease from African subtypes*. Biochemistry, 2002. **41**(27): p. 8613-9.
18. Ohtaka, H., et al., *Overcoming drug resistance in HIV-1 chemotherapy: the binding thermodynamics of Amprenavir and TMC-126 to wild-type and drug-resistant mutants of the HIV-1 protease*. Protein Sci, 2002. **11**(8): p. 1908-16.
19. Vega, S., L.W. Kang, A. Velazquez-Campoy, Y. Kiso, L. Mario Amzel, and E. Freire, *A structural and thermodynamic escape mechanism from a drug resistant mutation of the HIV-1 protease*. Proteins: Structure, Function, and Bioinformatics, 2004. **55**: p. 594-602.
20. Muzammil, S., P. Ross, and E. Freire, *A major role for a set of non-active site mutations in the development of HIV-1 protease drug resistance*. Biochemistry, 2003. **42**(3): p. 631-8.

21. Ohtaka, H., A. Schon, and E. Freire, *Multidrug resistance to HIV-1 protease inhibition requires cooperative coupling between distal mutations*. *Biochemistry*, 2003. **42**(46): p. 13659-66.
22. Velazquez-Campoy, A., Y. Kiso, and E. Freire, *The binding energetics of first- and second-generation HIV-1 protease inhibitors: implications for drug design*. *Arch Biochem Biophys*, 2001. **390**(2): p. 169-75.
23. Lafont, V., et al., *Compensating enthalpic and entropic changes hinder binding affinity optimization*. *Chem Biol Drug Des*, 2007. **69**(6): p. 413-22.
24. Carbonell, T. and E. Freire, *Binding thermodynamics of statins to HMG-CoA reductase*. *Biochemistry*, 2005. **44**(35): p. 11741-8.
25. Leavitt, S. and E. Freire, *Direct measurement of protein binding energetics by isothermal titration calorimetry*. *Curr Opin Struct Biol*, 2001. **11**(5): p. 560-6.
26. Velazquez Campoy, A. and E. Freire, *ITC in the post-genomic era...? Priceless*. *Bisophys Chem*, 2005. **115**(2-3): p. 115-24.
27. Sigurskjold, B.W., *Exact analysis of competition ligand binding by displacement isothermal titration calorimetry*. *Anal Biochem*, 2000. **277**(2): p. 260-6.
28. Wiseman, T., et al., *Rapid measurement of binding constants and heats of binding using a new titration calorimeter*. *Anal Biochem*, 1989. **179**(1): p. 131-7.
29. Sigurskjold, B.W., C.R. Berland, and B. Svensson, *Thermodynamics of inhibitor binding to the catalytic site of glucoamylase from *Aspergillus niger* determined by displacement titration calorimetry*. *Biochemistry*, 1994. **33**(33): p. 10191-9.
30. Buurma, N.J. and I. Haq, *Advances in the analysis of isothermal titration calorimetry data for ligand-DNA interactions*. *Methods*, 2007. **42**(2): p. 162-72.
31. Andujar-Sanchez, M., V. Jara-Perez, and A. Camara-Artigas, *Thermodynamic determination of the binding constants of angiotensin-converting enzyme inhibitors by a displacement method*. *FEBS Lett*, 2007. **581**(18): p. 3449-54.

32. Khalifah, R.G., et al., *Thermodynamics of binding of the CO₂-competitive inhibitor imidazole and related compounds to human carbonic anhydrase I: an isothermal titration calorimetry approach to studying weak binding by displacement with strong inhibitors*. Biochemistry, 1993. **32**(12): p. 3058-66.
33. Zhang, Y.L. and Z.Y. Zhang, *Low-affinity binding determined by titration calorimetry using a high-affinity coupling ligand: a thermodynamic study of ligand binding to protein tyrosine phosphatase 1B*. Anal Biochem, 1998. **261**(2): p. 139-48.
34. Todd, M.J. and J. Gomez, *Enzyme kinetics determined using calorimetry: a general assay for enzyme activity?* Anal Biochem, 2001. **296**(2): p. 179-87.
35. Morin, P.E. and E. Freire, *Direct calorimetric analysis of the enzymatic activity of yeast cytochrome c oxidase*. Biochemistry, 1991. **30**(34): p. 8494-500.
36. ITC Data Analysis in Origin, Tutorial Guide, Version 7.0, Ultrasensitive Calorimetry for the Life Sciences, MicroCal, 2004.
37. Hinz, H.J. and F.P. Schwarz, *Measurements and analysis of results obtained on biological substances with differential scanning calorimetry*. Pure Appl Chem, 2001. **73**(4): p. 745-759.
38. Manly, S.P., K.S. Matthews, and J.M. Sturtevant, *Thermal denaturation of the core protein of lac repressor*. Biochemistry, 1985. **24**(15): p. 3842-6.
39. Schwarz, F.P., *Interaction of cytidine 3'-monophosphate and uridine 3'-monophosphate with ribonuclease a at the denaturation temperature*. Biochemistry, 1988. **27**(22): p. 8429-36.
40. Ghosaini, L.R., A.M. Brown, and J.M. Sturtevant, *Scanning calorimetric study of the thermal unfolding of catabolite activator protein from Escherichia coli in the absence and presence of cyclic mononucleotides*. Biochemistry, 1988. **27**(14): p. 5257-61.

41. Schwarz, F.P., et al., *Thermodynamics of monosaccharide binding to concanavalin A, pea (Pisum sativum) lectin, and lentil (Lens culinaris) lectin*. J Biol Chem, 1993. **268**(11): p. 7668-77.
42. Schwarz, F.P., et al., *Thermodynamics of bovine spleen galectin-I binding to disaccharides: correlation with structure and its effect on oligomerization at the denaturation temperature*. Biochemistry, 1998. **37**(17): p. 5867-77.
43. Bruylants, G., J. Wouters, and C. Michaux, *Differential scanning calorimetry in life science: thermodynamics, stability, molecular recognition and application in drug design*. Curr Med Chem, 2005. **12**(17): p. 2011-20.
44. Brandts, J.F. and L.N. Lin, *Study of strong to ultratight protein interactions using differential scanning calorimetry*. Biochemistry, 1990. **29**(29): p. 6927-40.
45. Weber, P.C. and F.R. Salemme, *Applications of calorimetric methods to drug discovery and the study of protein interactions*. Curr Opin Struct Biol, 2003. **13**(1): p. 115-21.
46. Lakowicz, J.R., *Principles of Fluorescence Spectroscopy*, Second edition, Kluwer Academic/Plenum Publishers, New York, 1999.
47. Ramprakash, J., et al., *Comparison of the chemical and thermal denaturation of proteins by a two-state transition model*. Anal Biochem, 2008. **374**(1): p. 221-30.
48. Eftink, M.R., *Fluorescence methods for studying equilibrium macromolecule-ligand interactions*. Methods Enzymol, 1997. **278**: p. 221-57.
49. Lumry, R and S. Rajender, "Enthalpy-entropy compensation phenomena in water solutions of proteins and small molecules: a ubiquitous property of water." Biopolymers, 1970. **9**: p. 1125-1227.
50. Chang, C.E. and M.K. Gilson, *Free energy, entropy, and induced fit in host-guest recognition: calculations with the second-generation mining minima algorithm*. J Am Chem Soc, 2004. **126**(40): p. 13156-64.

51. Chen, W., C.E. Chang, and M.K. Gilson, *Calculation of cyclodextrin binding affinities: energy, entropy, and implications for drug design*. Biophys J, 2004. **87**(5): p. 3035-49.
52. Sturtevant, J.M., *Heat capacity and entropy changes in processes involving proteins*. Proc Natl Acad Sci U S A, 1977. **74**(6): p. 2236-40.
53. Tanhuanpaa, K. and P. Somerharju, *gamma-cyclodextrins greatly enhance translocation of hydrophobic fluorescent phospholipids from vesicles to cells in culture. Importance of molecular hydrophobicity in phospholipid trafficking studies*. J Biol Chem, 1999. **274**(50): p. 35359-66.
54. Desai, A., et al., *Lysozyme refolding with cyclodextrins: structure-activity relationship*. Biochimie, 2006. **88**(10): p. 1435-45.
55. Bar, J., et al., *Denaturation of phosphofructokinase-1 from Saccharomyces cerevisiae by guanidinium chloride and reconstitution of the unfolded subunits to their catalytically active form*. Biochemistry, 2000. **39**(23): p. 6960-8.
56. Jessel, N., et al., *Multiple and time-scheduled in situ DNA delivery mediated by beta-cyclodextrin embedded in a polyelectrolyte multilayer*. Proc Natl Acad Sci U S A, 2006. **103**(23): p. 8618-21.
57. Malpezzi, L., et al., *Crystal architecture and conformational properties of the inclusion complex, neohesperidin dihydrochalcone-cyclomaltoheptaose (β -cyclodextrin), by X-ray diffraction*. Carbohydrate Research, 2004. **339**: p. 2117-2125.
58. Chervenak, M.C. and E.J. Toone, "A direct measure of the contribution of solvent reorganization to the enthalpy of ligand binding." J Am Chem Soc, 1994. **116**: p. 10533-39.
59. Available from : <www.asiinstr.com/technical/Dielectric%20Constants.htm>.
60. Rekharsky, M.V. and Y. Inoue, *Complexation Thermodynamics of Cyclodextrins*. Chem Rev, 1998. **98**(5): p. 1875-1918.

61. Rekharsky, M.V. and Y. Inoue, in: H. Dodziuk (Ed.), *Cyclodextrins and Their Complexes*, Wiley-VCH Verlag GmbH & Co. KGaA, Weinheim, Germany, 2006, pp. 215-222.
62. Warren, G.L., C.W. Andrews, A. Capelli, B. Clarke, J. LaLonde, M.H. Lambert, M. Lidvall, N. Nevins, S.F. Semus, S. Senger, G. Tedesco, I.D. Wall, J.M. Woolven, C.E. Peishoff, M.S. Head, "*A critical assessment of docking programs and scoring functions.*" *J Med Chem*, 2005. **48**: p. 50362-83.
63. M. Vikmon, in: *International Symposium on Cyclodextrins*, vol. 7, 1981, pp. 69-74.
64. Myszka, D.G., et al., *The ABRF-MIRG'02 study: assembly state, thermodynamic, and kinetic analysis of an enzyme/inhibitor interaction.* *J Biomol Tech*, 2003. **14**(4): p. 247-69.
65. Goyenechea, N., et al., *Inclusion complexes of nabumetone with beta-cyclodextrins: thermodynamics and molecular modelling studies. Influence of sodium perchlorate.* *Luminescence*, 2001. **16**(2): p. 117-27.
66. Goldbaum, F.A., et al., *The effect of water activity on the association constant and the enthalpy of reaction between lysozyme and the specific antibodies D1.3 and D44.1.* *J Mol Recognit*, 1996. **9**(1): p. 6-12.
67. Ladbury, J.E., *Just add water! The effect of water on the specificity of protein-ligand binding sites and its potential application to drug design.* *Chem Biol*, 1996. **3**(12): p. 973-80.
68. Ashwell, J.D., *The many paths to p38 mitogen-activated protein kinase activation in the immune system.* *Nat Rev Immunol*, 2006. **6**(7): p. 532-40.
69. Cuenda, A. and S. Rousseau, *p38 MAP-kinases pathway regulation, function and role in human diseases.* *Biochim Biophys Acta*, 2007. **1773**(8): p. 1358-75.
70. Luis, F., E. Perdiguero, A.R. Nebreda, P. Munoz-Canoves, *Regulation of skeletal muscle gene expression by p38 MAP kinases.* *Trends Cell Biol*, 2006. **16**: p. 36-44.

71. Park, J.M., et al., *Macrophage apoptosis by anthrax lethal factor through p38 MAP kinase inhibition*. Science, 2002. **297**(5589): p. 2048-51.
72. Hsu, L.C., et al., *The protein kinase PKR is required for macrophage apoptosis after activation of Toll-like receptor 4*. Nature, 2004. **428**(6980): p. 341-5.
73. Freshney, N.W., et al., *Interleukin-1 activates a novel protein kinase cascade that results in the phosphorylation of Hsp27*. Cell, 1994. **78**(6): p. 1039-49.
74. Han, J., et al., *A MAP kinase targeted by endotoxin and hyperosmolarity in mammalian cells*. Science, 1994. **265**(5173): p. 808-11.
75. Lee, J.C., et al., *A protein kinase involved in the regulation of inflammatory cytokine biosynthesis*. Nature, 1994. **372**(6508): p. 739-46.
76. Natarajan, S.R., J.B. Doherty, *P38 MAP kinase inhibitors: evolution of imidazole-based and pyrido-pyrimidin-2-one lead classes*. Curr. Top. Med. Chem., 2005. **5**: p. 987-1003.
77. Diller, D.J., T.H. Lin, A. Metzger, *The discovery of novel chemotypes of p38 kinase inhibitors*. Curr. Top. Med. Chem., 2005. **5**: p. 953-965.
78. Young, P.R., et al., *Pyridinyl imidazole inhibitors of p38 mitogen-activated protein kinase bind in the ATP site*. J Biol Chem, 1997. **272**(18): p. 12116-21.
79. Wang, Z., et al., *Structural basis of inhibitor selectivity in MAP kinases*. Structure, 1998. **6**(9): p. 1117-28.
80. Wilson, K.P., et al., *Crystal structure of p38 mitogen-activated protein kinase*. J Biol Chem, 1996. **271**(44): p. 27696-700.
81. Cuenda, A., et al., *SB 203580 is a specific inhibitor of a MAP kinase homologue which is stimulated by cellular stresses and interleukin-1*. FEBS Lett, 1995. **364**(2): p. 229-33.

82. de Laszlo, S.E., et al., *Pyrroles and other heterocycles as inhibitors of p38 kinase*. Bioorg Med Chem Lett, 1998. **8**(19): p. 2689-94.
83. Kumar, S., et al., *Novel homologues of CSBP/p38 MAP kinase: activation, substrate specificity and sensitivity to inhibition by pyridinyl imidazoles*. Biochem Biophys Res Commun, 1997. **235**(3): p. 533-8.
84. Lee, J.C., et al., *p38 mitogen-activated protein kinase inhibitors--mechanisms and therapeutic potentials*. Pharmacol Ther, 1999. **82**(2-3): p. 389-97.
85. Dodeller, F. and H. Schulze-Koops, *The p38 mitogen-activated protein kinase signaling cascade in CD4 T cells*. Arthritis Res Ther, 2006. **8**(2): p. 205.
86. Kaminska, B., *MAPK signalling pathways as molecular targets for anti-inflammatory therapy--from molecular mechanisms to therapeutic benefits*. Biochim Biophys Acta, 2005. **1754**(1-2): p. 253-62.
87. Jiang, Y., et al., *Characterization of the structure and function of a new mitogen-activated protein kinase (p38beta)*. J Biol Chem, 1996. **271**(30): p. 17920-6.
88. Bellon, S., et al., *The structure of phosphorylated p38gamma is monomeric and reveals a conserved activation-loop conformation*. Structure, 1999. **7**(9): p. 1057-65.
89. Gallagher, T.F., et al., *Regulation of stress-induced cytokine production by pyridinylimidazoles; inhibition of CSBP kinase*. Bioorg Med Chem, 1997. **5**(1): p. 49-64.
90. Fitzgerald, C.E., et al., *Structural basis for p38alpha MAP kinase quinazolinone and pyridol-pyrimidine inhibitor specificity*. Nat Struct Biol, 2003. **10**(9): p. 764-9.
91. Wang, Z., et al., *The structure of mitogen-activated protein kinase p38 at 2.1-A resolution*. Proc Natl Acad Sci U S A, 1997. **94**(6): p. 2327-32.
92. Tong, L., et al., *A highly specific inhibitor of human p38 MAP kinase binds in the ATP pocket*. Nat Struct Biol, 1997. **4**(4): p. 311-6.

93. Kroe, R.R., et al., *Thermal denaturation: a method to rank slow binding, high-affinity P38alpha MAP kinase inhibitors*. J Med Chem, 2003. **46**(22): p. 4669-75.
94. Davidson, W., et al., *Discovery and characterization of a substrate selective p38alpha inhibitor*. Biochemistry, 2004. **43**(37): p. 11658-71.
95. Available from: <<http://moult.umbi.umd.edu/human2004/geneMAPK14.html>>.
96. Patel, S.B., et al., *Lattice stabilization and enhanced diffraction in human p38 alpha crystals by protein engineering*. Biochim Biophys Acta, 2004. **1696**(1): p. 67-73.
97. Sigurskjold, B.W., *Exact analysis of competition ligand binding by displacement isothermal titration calorimetry*. Anal Biochem, 2000. **277**(2): p. 260-6.
98. Buurma, N.J. and I. Haq, *Advances in the analysis of isothermal titration calorimetry data for ligand-DNA interactions*. Methods, 2007. **42**(2): p. 162-72.
99. Kirchhoff, W.H., Exam: A Two-State Thermodynamic Analysis Program. NIST Tech. Note 1401, US Government Printing Office, Washington, DC, 1993.
100. Schwarz, F.P., *Interaction of cytidine 3'-monophosphate and uridine 3'-monophosphate with ribonuclease a at the denaturation temperature*. Biochemistry, 1988. **27**(22): p. 8429-36.
101. Bzowska, A., E. Kulikowska, and D. Shugar, *Purine nucleoside phosphorylases: properties, functions, and clinical aspects*. Pharmacol Ther, 2000. **88**(3): p. 349-425.
102. Knapp, M., et al., *Targeting cancer: the challenges and successes of structure-based drug design against the human purinome*. Curr Top Med Chem, 2006. **6**(11): p. 1129-59.
103. Pugmire, M.J. and S.E. Ealick, *Structural analyses reveal two distinct families of nucleoside phosphorylases*. Biochem J, 2002. **361**(Pt 1): p. 1-25.

104. Zhang, Y., et al., *PNP anticancer gene therapy*. Curr Top Med Chem, 2005. **5**(13): p. 1259-74.
105. de Azevedo, W.F., Jr., et al., *Crystal structure of human purine nucleoside phosphorylase at 2.3 Å resolution*. Biochem Biophys Res Commun, 2003. **308**(3): p. 545-52.
106. Ealick, S.E., et al., *Three-dimensional structure of human erythrocytic purine nucleoside phosphorylase at 3.2 Å resolution*. J Biol Chem, 1990. **265**(3): p. 1812-20.
107. Ropp, P.A. and T.W. Traut, *Purine nucleoside phosphorylase. Allosteric regulation of a dissociating enzyme*. J Biol Chem, 1991. **266**(12): p. 7682-7.
108. dos Santos, D.M., et al., *Crystal structure of human purine nucleoside phosphorylase complexed with acyclovir*. Biochem Biophys Res Commun, 2003. **308**(3): p. 553-9.
109. de Azevedo, W.F., Jr., et al., *Crystal structure of human PNP complexed with guanine*. Biochem Biophys Res Commun, 2003. **312**(3): p. 767-72.
110. Ghanem, M., et al., *Tryptophan-free human PNP reveals catalytic site interactions*. Biochemistry, 2008. **47**(10): p. 3202-15.
111. Porter, D.J., *Purine nucleoside phosphorylase. Kinetic mechanism of the enzyme from calf spleen*. J Biol Chem, 1992. **267**(11): p. 7342-51.
112. Tuttle, J.V. and T.A. Krenitsky, *Effects of acyclovir and its metabolites on purine nucleoside phosphorylase*. J Biol Chem, 1984. **259**(7): p. 4065-9.
113. Stoeckler, J.D., et al., *Purine nucleoside phosphorylase from human erythrocytes*. Methods Enzymol, 1978. **51**: p. 530-8.
114. Stein, J.M., et al., *Inhibition of human purine nucleoside phosphorylase by acyclic nucleosides and nucleotides*. Biochem Pharmacol, 1987. **36**(8): p. 1237-44.

115. Kelley, J.L., Linn, J.A., McLean, E.W., and Tuttle, J.V., 9-[(Phosphonoalkyl)benzyl]guanines. *Multisubstrate Analogue Inhibitors of Human Erythrocyte Purine Nucleoside Phosphorylase*. J. Med. Chem., 1993, 36, 3455-3463.
116. Bzowska, A., et al., *Crystal structure of calf spleen purine nucleoside phosphorylase with two full trimers in the asymmetric unit: important implications for the mechanism of catalysis*. J Mol Biol, 2004. **342**(3): p. 1015-32.
117. Stoeckler, J.D., et al., *Purine nucleoside phosphorylase from human erythrocytes: physicochemical properties of the crystalline enzyme*. Biochemistry, 1978. **17**(2): p. 278-83.
118. Todd, M.J. and J. Gomez, *Enzyme kinetics determined using calorimetry: a general assay for enzyme activity?* Anal Biochem, 2001. **296**(2): p. 179-87.
119. ITC Data Analysis in Origin, Tutorial Guide, Version 7.0, Ultrasensitive Calorimetry for the Life Sciences, MicroCal, 2004.
120. Wyatt, P.J., *Light scattering and the absolute characterization of macromolecules*. Analytical Chimica Acta, 1993. **272**: p. 1-40.
121. Bzowska, A., *Calf spleen purine nucleoside phosphorylase: complex kinetic mechanism, hydrolysis of 7-methylguanosine, and oligomeric state in solution*. Biochim Biophys Acta, 2002. **1596**(2): p. 293-317.
122. Kulikowska, E., et al., *Properties of two unusual, and fluorescent, substrates of purine-nucleoside phosphorylase: 7-methylguanosine and 7-methylinosine*. Biochim Biophys Acta, 1986. **874**(3): p. 355-63.
123. Bzowska, A., et al., *Purine nucleoside phosphorylase: inhibition by purine N(7)- and N(9)-acyclonucleosides; and substrate properties of 7-beta-D-ribofuranosylguanine and 7-beta-D-ribofuranosylhypoxanthine*. Biochem Pharmacol, 1994. **48**(5): p. 937-47.

124. Ealick, S.E., et al., *Application of crystallographic and modeling methods in the design of purine nucleoside phosphorylase inhibitors*. Proc Natl Acad Sci U S A, 1991. **88**(24): p. 11540-4.
125. Edgcomb, S.P., B.M. Baker, and K.P. Murphy, *The energetics of phosphate binding to a protein complex*. Protein Sci, 2000. **9**(5): p. 927-33.
126. Chandler, D., *Interfaces and the driving force of hydrophobic assembly*. Nature, 2005. **437**(7059): p. 640-7.
127. Atkins, P., *The Elements of Physical Chemistry with Applications in Biology*, Third edition, W.H. Freeman and Company, New York, 2000.
128. van Holde, K.E., W.C. Johnson, and P.S. Ho, *Principles of Physical Biochemistry*, Prentice Hall, New Jersey, 1998.
129. Kelley, S.M. and N.C. Price, *The use of circular dichroism in the investigation of protein structure and function*. Current Protein and Peptide Science, 2000. **1**: p. 349-84.
130. Amersham Biosciences, *Gel filtration. Principles and Methods*, Handbook from Amersham Biosciences AB, 2002.
131. Wen, J., T. Arakawa, and J.S. Philo, *Size-exclusion chromatography with on-line light-scattering, absorbance, and refractive index detectors for studying proteins and their interactions*. Anal Biochem, 1996. **240**(2): p. 155-66.
132. Foltá-Stogniew, E. and K.R. Williams, *Determination of molecular masses of proteins in solution: implementation of an HPLC size exclusion chromatography and laser light scattering service in a core laboratory*. J. Biomolecular Techniques, 1999. **10**(2): p. 51-63.
133. Schellman, J.A., *Macromolecular binding*. Biopolymers, 1975. **14**: p. 999-1018.